Variational Techniques for Strongly Correlated Open Quantum Systems

Von der Fakultät für Mathematik und Physik
der Gottfried Wilhelm Leibniz Universität Hannover
zur Erlangung des akademischen Grades

Doktor der Naturwissenschaften
Dr. rer. nat.

genehmigte Dissertation von

M.Sc. Seyedjavad Kazemi

2021

Referent	:	Priv.-Doz. Dr. Hendrik Weimer
Korreferenten	:	Prof. Dr. Luis Santos
	:	Asst. Prof. Mohammad Maghrebi
Tag der Promotion	:	30.09.2021

Abstract

Quantum systems are subject to dissipation as perfect isolation from the surrounding environment is impractical. Though this might wash out the intriguing quantum features that are absent in classical systems, proper engineering of dissipation, by contrast, opens up the possibility to not only prepare resilient quantum states but also attain dynamical properties unreachable in closed systems. The former provides a robust source for universal quantum computation and the latter transcends the conventional equilibrium physics bringing on genuinely new many-body phenomena.

This work utilizes novel variational techniques to explore many-body effects in strongly correlated and/or interacting open quantum systems. After introducing these techniques in Part I, innovative solutions to several challenging problems in the context of non-equilibrium steady states are presented in Part II. In this part, we first address the issue of having genuine bistability in the steady state of open quantum systems. To this end, we develop a powerful framework to analyze stability in the long-time limit of a generic dissipative process with or without the detailed balance condition. The study of Toom's majority voting model in the presence of quantum fluctuations paves the way for engineering bistability using chiral jump operators. In a second step, we extend our variational method to approach otherwise intractable problems in the context of strongly interacting dissipative spin systems. Our method enables the estimation of steady-state properties across phase transitions. We exemplify this by simulating long-range interacting Rydberg gases undergoing different kinds of dissipation.

In Part III, we turn our attention to dynamical properties of open quantum systems. We mainly focus on the classification of dynamical behaviors in quantum systems building upon the notion of elementary cellular automata (ECA). A master equation embedding of ECA dynamical rule 110 being capable of universal computation reveals the existence of a phase transition between chaotic and unpredictable behavior. We then complement the dynamical system with a second process in such a way that unpredictability coexists with quantum entanglement even in the long time limit. Finally, we demonstrate an efficient realization of many-body interactions required for such systems relying on a variational quantum simulation scheme that employs available qubit technologies.

Keywords

— Open Quantum Many-Body Systems

— Variational Principles for Steady States

— Dissipative Phase Transitions

— Correlated Jump Operators

— Toom's Majority Voting Model

— Genuine Bistability

— Mesoscopic Langevin Equation

— Driven-Dissipative Rydberg Gases

— Unpredictable Dynamical Systems

— Probabilistic Cellular Automata

— Variational Quantum Simulation

In memory of my nephew and his passionate curiosity,
MoR Kazemi

Contents

I Introduction 1

1 Preliminary remarks 3
- 1.1 Motivation 3
- 1.2 Overview of the dissertation 4

2 Theory of open quantum systems 7
- 2.1 Density operator formalism 7
  - 2.1.1 Effective spin-1/2 description 8
  - 2.1.2 Composite quantum systems 9
- 2.2 Quantum operation 11
  - 2.2.1 Operator-sum representation 12
  - 2.2.2 Quantum Markovianity 13
- 2.3 Phase transitions and criticality 15
  - 2.3.1 Classical phase transition 16
  - 2.3.2 Quantum phase transition 19

3 Variational simulation of open quantum systems 21
- 3.1 Classical simulation methods 21
- 3.2 Variational principle 26
  - 3.2.1 Gutzwiller theory for open systems 27
  - 3.2.2 Beyond Gutzwiller treatment 31
- 3.3 Quantum simulation 33
  - 3.3.1 Dissipative variational quantum simulation 34
  - 3.3.2 Quantum simulation platforms 38

II Collective Effects in Steady States 45

4 Bistability in steady states 47

4.1 Introduction . . . 47
4.2 Thermally-activated nucleation processes . . . 48
4.2.1 Arrhenius law for open systems . . . 49
4.2.2 Application: Dissipative Ising model . . . 51
4.3 Non-equilibrium kinetics of nucleation . . . 54
4.3.1 Toom's majority voting model . . . 54
4.3.2 Mesoscopic Langevin formalism . . . 55

5 Stationary long-range correlation 63
5.1 Strong Rydberg-Rydberg interaction . . . 63
5.1.1 Van der Waals interaction . . . 64
5.1.2 Rydberg blockade effect . . . 65
5.2 Driven-Dissipative Rydberg gases . . . 66
5.3 Implementation of the variational technique . . . 68
5.3.1 Variational correlation functions . . . 69
5.3.2 Minimization constraints . . . 71
5.4 Liquid-gas phase transition . . . 72
5.4.1 Coherent drive vs decay . . . 73
5.4.2 Coherent drive vs dephasing . . . 77

III Dissipation-Assisted Unpredictable Dynamics 79

6 Dissipative cellular automata 81
6.1 Elementary cellular automata . . . 82
6.1.1 ECA classification . . . 82
6.1.2 Complexity classes and unpredictability . . . 85
6.2 Embedding of elementary cellular automata . . . 87
6.3 Cycle time phase transition . . . 90
6.3.1 Purely classical dynamics . . . 90
6.3.2 Competition with entanglement . . . 92

7 Quantum simulation of complex models 97
7.1 Dissipative quantum state preparation . . . 97
7.1.1 Rokhsar-Kivelson state . . . 98
7.1.2 Trapped-ion co-processor . . . 100
7.2 Quantum simulation of unpredictable evolution . . . 102
7.2.1 Circuit architecture . . . 102
7.2.2 Rydberg-atom co-processor . . . 104

IV Conclusion 109

8 Summary and outlook 111
8.1 Summary 111
8.2 Outlook 112

V Appendices 115

A Microscopic derivation of Lindblad equation 117
A.1 Born-Markov approximation 117
A.2 Secular approximation 118

B Characterization of Toom-like bistability 121
B.1 Ginzburg-Landau variational functional 121
B.2 Domain-wall kinetics in Toom's model 122

C Correlated jump operators in Rydberg atoms 125
C.1 Adiabatic elimination 125
C.2 Tailoring correlated jump operators 125

D Frozen Rydberg gases and the Ising model 129
D.1 Rydberg vs. Ising Hamiltonian 129
D.2 Numerical simulation 132

Acknowledgements 156

Part I

Introduction

In the modern world view, dissipation has taken over one of the functions formerly performed by God: It makes matter transcend the clod-like nature it would manifest at equilibrium, and behave instead in dramatic and unforeseen ways, molding itself, for example, into thunderstorms, people, and umbrellas.

— Charles Henry Bennett

Chapter 1

Preliminary remarks

1.1 Motivation

What do we gain from studying open quantum systems? First of all, open systems are fundamentally different from the closed systems as their dynamical properties go beyond the conventional condensed equilibrium matter leading to genuinely new many-body phenomena. This essentially comes from the fact that in open systems conservation of energy and the microscopically detailed balance can be broken and hence a thermal statistical description is ruled out. There are in fact several ways to originate *non-equilibrium behavior* in open systems such as strong coupling to non-thermal bath, or different thermal bath. However, the most well-established way relies on the notion of *driven-dissipative many-body systems* in which quantum particles are weakly coupled to an environment and the system is driven out of thermal equilibrium by external fields.

Moreover, these systems provide a novel approach in quantum state preparation which is highly required in different branches of quantum science including quantum information and computation [1], quantum simulation [2], and quantum metrology [3, 4]. The so-called *dissipation-assisted quantum-state engineering* is based on the idea of tailoring specific dissipation channels and coherent interactions such that the steady state of the corresponding dynamics becomes the desired quantum state [5, 6, 7, 8]. Importantly, dissipative state preparation is experimentally easier and more robust compared to ground-state preparation in closed systems [9].

Spin-1/2 models are one of the most important classes of quantum many-body systems due to their correspondence with qubits in the context of quantum computation and quantum information. Also from the experimental point of view, recent advancements in implementing ultracold atoms have attracted more attention to the spin-1/2 models as they can be effectively described by two-level systems in certain regimes. Particularly, laser-driven ultracold atoms in the presence of controlled dissipation is an implementation of the aforementioned driven-dissipative systems which open up the possibility to explore far-from-equilibrium phenomena. However, there are numerous open questions in this field which makes it necessary to undertake novel theoretical studies alongside experimental observations.

1.2 Overview of the dissertation

In this thesis, we will explore different collective behavior of driven-dissipative spin-1/2 models by developing classical and quantum variational methods. In **Part I**, we cover the basic concepts and required tools to study the aforementioned models. **Chapter 2** overviews the theory of open quantum systems especially in the Markovian regime and variational techniques for analysis of these systems are presented in **Chapter 3**.

Having introduced the variational approach for open systems, in **Part II** we study two different aspects of steady states. First, in **Chapter 4** we investigate bistability in steady states using the notion of nucleation process in the presence of thermal and non-thermal fluctuations. To this end, we establish a Gutzwiller approach employing the variational principle for open systems. Using this approach in combination with a theory of metastability, we show that predicted hysteresis behavior in conventional dissipative systems only appears in the vicinity of phase transitions. Importantly, we demonstrate a genuine bistability building upon a quantum variant of a majority-voter model known as Toom's model for which we present a variational Langevin formalism.

As another aspect, we develop our variational method to compute long-range correlations in the steady of strongly interacting dissipative spin models. In Chapter 5, we present the variational results for the non-equilibrium steady state of dissipative Rydberg gases with strong long-range interactions, an intriguing model whose numerical simulation is very challenging. Specifically, we find a dissipative variant of the Rydberg blockade in the pair correlation function, a particular regime in which any simultaneously bipartite excitation within a so-called blockaded radius is inhibited. In addition, we investigate the interplay between coherent driving and dissipation. This setting gives us the chance of detecting a first-order quantum phase transition in a two-dimensional setup with the density of Rydberg excitation as the order parameter.

In **Part III**, we focus on the dynamical properties of open quantum systems, especially searching for unpredictable behavior in contrast to chaotic behavior being statistically predictable in a coarse-grained level. In **Chapter 6**, we propose a master-equation embedding of an unpredictable class of elementary cellular automata (ECA) which are conjectured to be Turing complete and capable of universal computation. The embedding makes it possible to demonstrate a phase transition between chaotic and unpredictable dynamical behavior. Moreover, we explore the interplay between quantum entanglement and unpredictability by adding a set of quantum operators that drive the system to highly-entangled states. Strikingly, we show that by tailoring proper many-body interactions, entanglement can get along with unpredictability. **Chapter 7** of this thesis proposes a hardware-efficient experimental realization of the required interactions. The realization relies on an open system version of a variational quantum estimation algorithm.

Finally, **Part III** sums up the content of this thesis by summarizing the results and outlining possible directions for future research in **Chapter 8**.

Chapter 2

Theory of open quantum systems

2.1 Density operator formalism

The non-commutative algebra of observables in quantum mechanics boils down to an operational definition of quantum states living in the Hilbert space (an abstract complex vector space with an inner product). Basically, a general quantum state, the complete state-of-knowledge about a quantum system, can be represented by a non-negative operator which serves as a probability density over all possible states. The so-called *density operator* (or *density matrix*) represents both classical uncertainty of a quantum system (which typically originates from errors of state preparation) and quantum uncertainty which is an inherent feature of quantum systems.

A spectral representation of a density operator in terms of projection operators, an outer product of a vector $|\psi\rangle$ and its dual vector $|\psi\rangle^\dagger = \langle\psi|$, is given by

$$\rho = \sum_i p_i |\psi_i\rangle\langle\psi_i|, \tag{2.1}$$

which shows a statistical ensemble over possible quantum states $|\psi_i\rangle$ weighted by probabilities p_i adding up to one, $\sum_i p_i = 1$. In other words, the mean value of any *observable* O (a Hermition operator $O^\dagger = O$) in a physical system (for instance the polarization of a light beam) is given by a probabilistic average of measuring O in quantum states $|\psi_o\rangle$ (polarization states in this example),

$$\langle O\rangle = \sum_o p_o \langle\psi_o|O|\psi_o\rangle = \mathrm{Tr}\{O\rho\}. \tag{2.2}$$

The so-called *expectation value* $\langle O\rangle$ is the statistical information of observable O that the theory of quantum mechanics ultimately describes. Crucially, it can only predict probabilistic outcomes of *statistical experiments* where the probabilities come from an average over repeated individual measurements. Therefore, a density operator encapsulates measurement information of a statistical ensemble, not an individual system.

It is now straightforward to extract the general properties of the density operator from Eq. (2.1), namely

- Hermiticity: $\rho^\dagger = \rho$;
- Positivity: $\langle\psi|\rho|\psi\rangle \geq 0$ for any $|\psi\rangle$;
- Unit trace: $\mathrm{Tr}\{\rho\} = 1$.

The *purity* of a density operator is also out of importance. If the spectral decomposition Eq. (2.1) has only one non-zero probability, $\rho = |\psi\rangle\langle\psi|$, the state is called *pure* and otherwise *mixed*. From a different point of view, a pure state is the extremum of a convex set of all states, i.e. it cannot be written as a convex combination of other states, $\lambda\rho_1 + (1-\lambda)\rho_2$ where $\lambda \in (0,1)$. Therefore, an immediate measure for purity is represented by $\mathrm{Tr}\{\rho^2\}$ which is upper-bounded by 1 for ρ being pure and lower-bounded by $1/d$ for the *maximally mixed state* $\rho = \mathrm{I}/d$, where I is a d-dimensional identity matrix.

Generally, the diagonal elements of a density matrix are called *populations* as they represent the probabilities of a system being measured in the given basis and the off-diagonal elements encode *coherences* which determine the quantumness of the underlying state. That is why a maximally mixed state is solely a classical or incoherent mixture of all possible states.

2.1.1 Effective spin-1/2 description

The simplest form of a density operator corresponds to a two-level quantum system or a *qubit* that can be represented in terms of Pauli matrices plus the identity matrix,

$$\rho_0 = \frac{1}{2}\Big(I + \sum_{i\in\{x,y,z\}} \alpha_i\sigma_i\Big) = \frac{1}{2}\begin{pmatrix} 1+\alpha_z & \alpha_x - i\alpha_y \\ \alpha_x + i\alpha_y & 1-\alpha_z \end{pmatrix}, \tag{2.3}$$

where

$$\mathrm{I} = \begin{pmatrix} 1 & 0 \\ 0 & 1 \end{pmatrix}, \quad \sigma_x = \begin{pmatrix} 0 & 1 \\ 1 & 0 \end{pmatrix}, \quad \sigma_y = \begin{pmatrix} 0 & -i \\ i & 0 \end{pmatrix}, \quad \sigma_z = \begin{pmatrix} 1 & 0 \\ 0 & -1 \end{pmatrix}.$$

Since Pauli matrices are Hermitian and trace-less, the conditions of Hermiticity and unit trace are already satisfied. However, for the positivity condition, we need to add an additional constraint on Eq. (2.3), that is $\alpha_x^2 + \alpha_y^2 + \alpha_z^2 \leq 1$. In the following chapters, we will employ this constraint for variational estimation of density matrices. In fact, from the numerical point of view, it is enough to ensure that the least eigenenergy of a given density matrix is positive.

A geometrical representation of Eq. (2.3) on the well-known *Bloch sphere* demonstrates how a classical bit differs from a qubit. To be specific, the latter can additionally include *superposed states*, i.e. all the non-polar points on the surface of the Bloch sphere. It is evident that all the unital vectors pointing on the surface, i.e. $\alpha_x^2 + \alpha_y^2 + \alpha_z^2 = 1$, represent pure states while the non-unital vectors inside the sphere show all possible mixed states for a qubit.

Qubits can be used to model different physical systems with two distinct states. For example,

- A Spin-1/2 particle like an electron: $|0\rangle = |\text{spin down}\rangle$ and $|1\rangle = |\text{spin up}\rangle$;
- A two-level atom like an effective Rydberg atom: $|0\rangle = |\text{ground state}\rangle$ and $|1\rangle = |\text{Rydberg state}\rangle$;
- A cellular automaton: $|0\rangle = |\text{dead cell}\rangle$ and $|1\rangle = |\text{live cell}\rangle$;
- Polarization of a photon: $|0\rangle = |\text{horizontal polarization}\rangle$ and $|1\rangle = |\text{vertical polarization}\rangle$;

Also, for general d-dimensional systems, *qudits*, the Bloch sphere parametrization can be still applicable using the notion of generalized Pauli matrices, e.g. Gell-Mann matrices for 3-level systems or *qutrits* [10, 11].

2.1.2 Composite quantum systems

So far, we have only looked at the quantum states of individual quantum systems. However, more intriguing properties of quantum states come into the picture when we deal with composite systems. A density operator describing a composition of individual systems is then defined on the tensor product of the individual Hilbert spaces. Now, a bipartite state ρ_{AB} defined on the total Hilbert space $\mathcal{H}_A \otimes \mathcal{H}_B$ is *separable* (or *classically correlated*) if it can be written as

$$\rho_{AB} = \sum_i \lambda_i \rho_A^{(i)} \otimes \rho_B^{(i)},$$

with positive λ_i as well as $\rho_A^{(i)}$ and $\rho_B^{(i)}$ being defined on $\mathcal{H}_A$ and $\mathcal{H}_B$, respectively. Otherwise, ρ_{AB} is called *entangled* [12].

To understand the concept of quantum entanglement, let us first define the notion of *partial trace*. The mathematical recipe to discard some part of a composite system and obtain a description of the remaining subsystem, say ρ_A, is provided by the partial trace. The so-called *reduced state* ρ_A is determined by tracing the total density matrix only with respect to the discarded Hilbert space,

$$\rho_A = \mathrm{Tr}_B\{\rho_{AB}\} = \sum_b (\mathrm{I}_A \otimes \langle\psi_b|)\rho_{AB}(\mathrm{I}_A \otimes |\psi_b\rangle),$$

where the set of $\{|\psi_b\rangle\}$ forms a basis on $\mathcal{H}_B$ and is I_A the identity operator in $\mathcal{H}_A$. An important implication for bipartite systems is that if the composite state is pure and the reduced density matrix on either system is maximally mixed, the total state is a *maximally entangled state*, e.g. $\rho_{AB} = (|00\rangle\langle 00| + |11\rangle\langle 11|)/2$. In other words, the mixedness of a reduced density matrix indicates the existence of entanglement in the original pure state. This feature is useful to measure entanglement in pure bipartite state in terms of the *von Neumann entropy* of the reduced density matrix on either subsystem,

$$S_A = -\mathrm{Tr}\{\rho_A \ln \rho_A\}. \tag{2.4}$$

The so-called *entanglement entropy* of a $2k$-qubit system is then bounded as $S_A \in [0, k\ln 2]$ with A containing half of the total qubits.

However, the bipartite entanglement obviously cannot describe all kinds of entanglement which might appear in many-body quantum systems. To give some examples, here are the most well-known pure states that are highly entangled and yet non-biseprable,

$$\begin{aligned}|\mathrm{GHZ}\rangle &= \frac{|00...0\rangle + |11...1\rangle}{\sqrt{2}},\\ |\mathrm{W}\rangle &= \frac{|100...0\rangle + |010...0\rangle + ... + |000...1\rangle}{\sqrt{N}}.\end{aligned}$$

The above states are defined for a general system with N qubits. In general, to compute multipartite entanglement in a generic mixed state, one can use the so-called *quantum negativity*[13] being defined as

$$\mathcal{N}(\rho) = \frac{\|\rho^{\mathrm{T}_A}\|_1 - 1}{2}, \tag{2.5}$$

where ρ^{T_A} is a partial transpose with respect to the subsystem A and $\|O\|_1 = \mathrm{Tr}\sqrt{O^\dagger O}$ is the *trace norm* which is the sum of the absolute values of the eigenvalues. The negativity is equivalent to the absolute sum of the negative eigenvalues of ρ^{T_A} which is based on the fact that the partial transpose of a separable state has no negative eigenvalue.

In general, deciding whether a quantum state is separable has been shown to be NP-hard [14]. A more useful definition for the correlation's content of density matrices is such that if a state can be written as

$$\rho_p = \prod_{i=1}^{N} \rho_i = \rho_1 \otimes \rho_2 \otimes \ldots \otimes \rho_n, \tag{2.6}$$

then the state is a *product state* and otherwise it's classically or/and quantum correlated. Accordingly, a generic correlated density matrix describing N particles can be expanded in terms of single-particle density matrices ρ_i and correlation matrices $C_{ij\ldots}$, that is

$$\begin{aligned} \rho_c = \rho_p + & \sum_{ij} \mathcal{R} C_{ij} + \sum_{ij \neq kl} \mathcal{R} C_{ij} C_{kl} + \ldots \\ & + \sum_{ijk} \mathcal{R} C_{ijk} + \sum_{ijk \neq lmn} \mathcal{R} C_{ijk} C_{lmn} + \ldots \\ & + \sum_{ijkl} \mathcal{R} C_{ijkl} + \ldots, \\ & + \ldots \end{aligned} \tag{2.7}$$

where $\mathcal{R}$ converts every I_i into the single-particle density matrices ρ_i, i.e. $\mathcal{R}\mathrm{I} = \prod_{i=1} \rho_i$. In the rest of this thesis, we will widely use the above expansion to describe many-body systems.

2.2 Quantum operation

Operators as matrix-like objects act on vector-like states to produce new states. When it comes to pure states of quantum systems, unitary operators, i.e. $UU^\dagger = U^\dagger U = \mathrm{I}$, are relevant as they preserve the total probabilities of the state which are acted upon. According to the famous Schrödinger equation, unitaries describe the time translations of closed quantum systems being completely isolated from the surrounding environment. Since the time translation is unitary, there exists a Hermition operator, known as the Hamiltonian operator $H^\dagger = H$, which represents the total energy of the system. Therefore, the time evolution of a closed system is expressed as

$$i\hbar \frac{d}{dt} |\psi(t)\rangle = H |\psi(t)\rangle \to |\psi(t)\rangle = e^{-iH(t-t_0)/\hbar} |\psi(t_0)\rangle, \tag{2.8}$$

where $U = e^{-iH(t-t_0)/\hbar}$ represents a unitary *time-evolution operator* or a *propagator* with H acting as a time-translation generator. Basically, U can be thought of as a complex rotation matrix that can diagonalize the associated Hermitian operator. Here, the time-transnational symmetry of the dynamics is a consequence of the energy conservation of the generator which is encoded into the Hamiltonian. From now on, for the sake of simplicity, we set $\hbar = 1$.

2.2.1 Operator-sum representation

A transformation of a density matrix, in turn, can be represented by a *superoperator* or a *quantum operation* as an operator-to-operator map, i.e.

$$\rho_f = \mathcal{E}(\rho_i).$$

General evolution of a quantum system from an initial state ρ_i to a final state ρ_f imposes certain features to the quantum operation $\mathcal{E}$. First of all, this map must be linear (since quantum mechanics is a linear theory), trace-preserving and positive, i.e. generates only positive states. Moreover, since a generic quantum state might be a sub-state of a larger system, the map of the latter must be also positive. This asserts more restrictions on the map of the state of interest as the partial trace of the larger map, that is known as being *completely positive*. It turns out that a valid quantum operation for an N-dimensional system is completely positive if and only if it can be formulated as follows

$$\mathcal{E}(\rho) = \sum_n K_n \rho K_n^\dagger, \tag{2.9}$$

where $\sum_n K_n^\dagger K_n = \mathrm{I}$. The so-called *operator-sum representation* includes (maximally) N^2 operators K_n which are referred to as *Kraus operators* [15].

From a more intuitive perspective, the non-unitary evolution of a quantum systems can be obtained from a unitary evolution of a larger system. In other words, our system of interest S is coupled to another (larger) system E over which we might have no control, resembling an open system interacting with the surrounding environment. Following the definition of the Schrödinger equation for a closed system, one can reach the equation of motion for the density matrix of an open system, or the *von Neumann equation*, that is given by

$$\frac{d}{dt}\rho_{\mathrm{SE}}(t) = -i[H_{\mathrm{SE}}, \rho_{\mathrm{SE}}(t)], \tag{2.10}$$

where $H_{\mathrm{SE}} = H_{\mathrm{S}} + H_{\mathrm{E}} + H_{\mathrm{int}}$ denotes the total Hamiltonian of the open system and its environment including an interaction term H_{int}. Therefore, given the total initial state $\rho_{\mathrm{SE}}(t_0)$, the state of the system S at an arbitrary time t

can be obtained as

$$\rho_{\mathrm{S}}(t) = \mathrm{Tr}_{\mathrm{E}}\{U(t,t_0)\rho_{\mathrm{SE}}(t_0)U^{\dagger}(t,t_0)\}, \tag{2.11}$$

where $U(t,t_0) = e^{-iH_{\mathrm{SE}}(t-t_0)}$. Now, considering an uncorrelated initial state $\rho_{\mathrm{SE}}(t_0) = \rho_{\mathrm{S}}(t_0) \otimes \rho_{\mathrm{E}}(t_0)$, we can retrieve the explicit form of Kraus operators using a spectral decomposition of $\rho_{\mathrm{E}}(t_0) = \sum_i \lambda_i |\psi_{\mathrm{E}}\rangle\langle\psi_{\mathrm{E}}|$,

$$\begin{aligned}\rho_S(t) =& \mathrm{Tr}_{\mathrm{E}}\{U(t,t_0)\rho_{\mathrm{S}}(t_0) \otimes \sum_i \lambda_i |\psi_{\mathrm{E}}\rangle\langle\psi_{\mathrm{E}}| U^{\dagger}(t,t_0)\}\\ =& \sum_{ij} \sqrt{\lambda_i}\langle\psi_j|U(t,t_0)|\psi_i\rangle\rho_{\mathrm{S}}(t_0)\sqrt{\lambda_i}\langle\psi_i|U^{\dagger}(t,t_0)|\psi_j\rangle\\ =& \sum_{ij} K_{ij}(t,t_0)\rho_{\mathrm{S}}(t_0)K_{ij}^{\dagger}(t,t_0).\end{aligned}$$

A more general derivation including initial correlation can be found in Ref. [16]. Importantly, any kind of time evolution in quantum systems can be expressed by the Kraus decomposition. In the next section, we will specifically focus on an important set of quantum operations that describe continuous time evolution with the following condition,

$$\mathcal{E}(t_2,t_0) = \mathcal{E}(t_2,t_1)\mathcal{E}(t_1,t_0), \tag{2.12}$$

known as *divisibility condition.* This condition enforces a time-local evolution of a quantum state with a short memory on its history, paving the way for defining a quantum analog of classical Markovian processes.

2.2.2 Quantum Markovianity

In order to gain more insight about the notion of Markovian processes in quantum systems, let's first look at a real implementation of the same. In quantum optics, an open quantum system refers to a quantum system that is coupled to a large environment, resembling the canonical ensemble in statistical mechanics where a mechanical system is coupled to a heat bath. In this setup, the system of interest is often a group of qubits that on its own undergoes a coherent evolution with a frequency scale of ω_S, and a typical quantum-optical environment is represented by a bath of harmonic oscillators hence a set of bosonic modes.

A microscopic description of a general open quantum-optical system in most cases can be determined by making two approximations (for a detailed derivation see Appendix A). First of all, the well-known *rotating wave approximation* is considered to neglect the fast-oscillating terms in the Hamiltonian of interaction between the system and environment. The approximation takes place in an interaction picture of the model considering a rotation with the system to simplify time dependency of the evolution [17]. Secondly, it is usual to assume a weak system-environment coupling and a fast relaxation rate of the environment compared with the typical time associated with the dynamics of the system. This leads to the *Born-Markov approximation* in perturbation treatment of the dynamics. In other words, we can describe the time evolution of the system by a *Markovian process* of Eq. (2.12), as the memory length of the environment is assumed to be relatively short. A more general description of open quantum systems beyond the Markovian regime is discussed in Refs. [16, 18, 19].

Derivation of the Markovian master equation, a linear differential equation describing the time evolution of an open quantum system, requires computing the time derivative of $\rho(t)$. Making use of the operator-sum representation in Eq. (2.9) for an infinitesimal time interval dt we have,

$$\begin{aligned}\frac{d}{dt}\rho(t) &= \lim_{dt\to 0}\frac{\rho(t+dt)-\rho(t)}{dt}\\ &= \lim_{dt\to 0}\frac{\mathcal{E}(t+dt,0)-\mathcal{E}(t,0)}{dt}\rho(0)\\ &= \lim_{dt\to 0}\frac{\mathcal{E}(t+dt,t)-\mathrm{I}}{dt}\rho(t),\end{aligned}$$

where in the last line we utilized the Markov approximation by considering a divisible generator $\mathcal{E}(t+dt,0)=\mathcal{E}(t+dt,t)\mathcal{E}(t,0)$. The resultant differential equation can be further simplified using the rotating wave approximation leading to the famous *Lindblad master equation* [20, 16]. The Markovian evolution of a generic quantum state ρ can then be represented by the *Liouvillian superoperator* which is given by $\partial_t\rho = \mathcal{L}(\rho)$,

$$\mathcal{L}(\rho) = -i[H,\rho] + \sum_j \left(c_j\rho c_j^\dagger - \frac{1}{2}\{c_j^\dagger c_j,\rho\}\right), \tag{2.13}$$

where H is the Hamiltonian of the system and the set of c_js denotes the *jump operators* or *collapse operators* originated from environment couplings. The first term in the Lindblad master equation is exactly equivalent to the von Neumann equation describing the coherent part of the evolution whereas the second term expresses the dissipative part.

Table 2.1 summarizes various types of dissipative processes that can occur in two-level systems. The corresponding jump operators are usually classified in terms of their locality, ranging from a single-body operator to a fully collective operator. In this range, any intermediate multi-body jump operator

	decay	pumping	dephasing
local	$\sigma_-^{(i)}$	$\sigma_+^{(i)}$	$\sigma_z^{(i)}$
correlated*	$P_1^{(i-1)}\sigma_-^{(i)}P_1^{(i+1)}$	$P_0^{(i-1)}\sigma_+^{(i)}P_0^{(i+1)}$	$P_0^{(i-1)}\sigma_z^{(i)}$
collective	$\sum_i \sigma_-^{(i)}$	$\sum_i \sigma_+^{(i)}$	$\sum_i \sigma_z^{(i)}$

Table 2.1: Dissipative processes in open quantum systems and the jump operators generating them in the case of two-level systems. Here $\sigma_- = \sigma_+^\dagger = |1\rangle\langle 0|$ denotes a depopulation of the excited state and $P_\alpha = |\alpha\rangle\langle\alpha|$ is a projection onto $|\alpha\rangle$ (*the correlated jump operators are only given as examples).

is called *correlated*, as a jump on a given site becomes conditional upon quantum operations on some other sites. In the rest of this thesis, we will employ local and correlated jump operators for state preparation.

The Markovian evolution typically features stationary behaviour in the long-time limit of the underlying system. In this limit, it is often the case that a unique *steady state* emerges irrespective of the initial configuration. The steady state,

$$\rho_{\mathrm{ss}} = \arg \lim_{t\to\infty} \mathcal{L}(\rho_t),$$

corresponds to the null space of the associated Liouvillian, i.e. $\hat{\mathcal{L}}(\rho_s) = 0$. However, in rare cases, dependency on the initial configurations may result in multiple steady states. We will elaborate on such cases in Chapter 4.

2.3 Phase transitions and criticality

So far, we have talked about the behavior of quantum systems on a microscopic scale where we have access to the inter- and intra-particle interactions. Although the microscopic description of interacting particles provides insightful information about the underlying system, it doesn't directly justify the appearance of macroscopic phases of matter, i.e. the collective behavior of many-body systems in the *thermodynamic limit*, $N \to \infty$. Moreover, classification of the so-called *thermodynamic phases* and non-trivial transitions between them requires a systematic treatment that goes beyond the microscopic description. In the following, we first describe the fundamental physics behind *phase transitions* in classical systems, i.e. matter in the presence of thermal fluctuations, based on the theory of classical thermodynamics. Next, we introduce the notion of phase transition in quantum systems in the limit of absolute zero temperature.

2.3.1 Classical phase transition

A many-body system undergoes a phase transition by varying an external *control parameter* such as temperature or magnetic fields. In other words, within a phase, the underlying system evolves smoothly in terms of its macroscopic properties. However, crossing a critical value of the control parameter, a dramatic change in the system properties can occur which results in a qualitatively different phase. The resultant phase transitions are often characterized by ordering and symmetries. For example, disordered liquids (often) freeze into crystalline solids upon lowering temperature like in the water-ice transition. Although the liquid phase exhibits translational symmetry, the solid phase is no longer translational invariant due to the crystalline structure. As another example, magnetic materials like iron exhibit a phase transition from a magnetically ordered phase, i.e. ferromagnetic with a parallel orientation of the spins, at low temperature to a disordered phase with rotational symmetry, i.e. paramagnetic with random orientations, above a critical temperature called Curie temperature.

The underlying *symmetry-breaking* phenomenon in the aforementioned examples is an indication of a wide variety of phase transitions involving crystallization, magnetism, superconductivity, etc. To quantify a phase transition, the notion of *order parameter* has been introduced as a thermodynamic variable that is zero on the symmetric phase and nonzero on the symmetry-broken phase. For example in the case of the ferromagnet-paramagnet transition, the magnetization is the order parameter that is vanishing (finite) in the paramagnetic (ferromagnetic) phase.

According to classical thermodynamics, the order parameter and in general all the *macroscopic quantities*, all measurable quantities of a system in the thermodynamic limit, can be deduced from the *Helmholtz free energy* F and the *partition function* Z,

$$F = -k_B T \log Z \qquad \text{with} \quad Z = \sum_i e^{-\frac{E_i}{k_B T}},$$

where T is the temperature of the system with energy levels E_i. In fact, the order parameter can be obtained as some derivative of F. On the other hand, since the order parameter is zero for a finite range of the control parameter and non-zero for the other side of a transition, it can not be an analytic function. This implies that F becomes also non-analytic when it comes to a phase transition. However, we have to mention that the transition-induced non-analyticity in F and Z can only appear in the thermodynamic limit where the number of energy levels goes to infinity. In a more physical sense, a phase transition arises from a competition between the entropic part and the energetic part of the free energy. According to classical thermodynamics, the contributions of these two parts in the free energy is given by

$$F = U - TS,$$

with U as the internal energy of a system U and S as the entropy. This relation demonstrates how temperature can control a system's behavior as it changes the entropic contribution of F. In other words, the system would exhibit an ordered phase provided that the *thermal fluctuations* are low. The order can be then broken in the presence of large enough fluctuations. The resulting *thermal phase transition* (TPT) is mainly the mechanism behind the phase transition at finite temperatures.

Phase transitions are often classified according to the nature of the broken analyticity (the lowest derivative of the free energy with respect to some thermodynamic variable). A transition is referred to as a *first-order phase transition* provided that a first derivative of the free energy is discontinuous at the transition, like solid/liquid/gas transitions. However, if the first derivative of the free energy is continuous and higher derivatives exhibit discontinuity, the corresponding transition is called a *continuous phase transition*. The ferromagnet-paramagnet transition is a well-known example of a second-order phase transition as the second derivative of the free energy with respect to the magnetic field, i.e. magnetic susceptibility, shows a sudden change at the transition.

Ginzburg-Landau theory

In general, we do not know the explicit mathematical form of the free energy as it is a complicated function of the order parameter. As a solution to this issue, Landau's remarkable proposal was to expand F in a power series of the order parameter in proximity to the critical point. This expansion is based on the assumption that the order parameter is uniform and small close to the critical point. In the Landau theory, the expansion is restricted to the terms which don't violate the symmetry of the system and the highest order term must be chosen such that it has an even exponent and a positive coefficient to guarantee a stable state [21]. However, a drawback of this theory is that the order parameter is free of any temporal and spatial fluctuation that is required for an accurate description of a thermodynamic phase. This is why the *Landau-Ginzburg theory* is developed by adding fluctuation into the free energy in the form of some gradients, leading to the so-called *Ginzburg-Landau functional*

$$F = \int d\mathbf{r} f[\Phi(\mathbf{r})] + \int d\mathbf{r} g[\nabla\Phi(\mathbf{r})], \tag{2.14}$$

where f and g represent power series of the order parameter in the form of a spatial field $\Phi(\mathbf{r})$, and the gradient terms respectively. Using the Ginzburg-Landau functional, one can obtain a differential equation for the order parameter relying on the extremum principle, $\delta F = 0$, similar to the Lagrange equations in classical mechanics. Moreover, The Ginzburg-Landau equation can be extended to describe the time evolution of a system in terms of a time-dependent field. In Chapter 4 we will investigate the time-dependent theory in more detail.

Universality

Now, let us to look at a specific example of the Ginzburg-Landau functional that can describe the second-order ferromagnet-paramagnet transition. The functional is given by

$$F = \int d\mathbf{r} \Big[u_2 \Phi^2(\mathbf{r}) + u_4 \Phi^4(\mathbf{r}) + v_2 [\nabla\Phi(\mathbf{r})]^2 \Big], \tag{2.15}$$

that in which the odd terms disappear due to the assumption of having the reflection symmetry $\phi \to -\phi$. The critical point is then determined when the quadratic term changes sign, i.e. $u_2 = 0$. Significantly, a wide variety of phase transitions can be characterized using the so-called *ϕ^4-theory* only based on the symmetry and dimensionality. This brings us to the notion of *universality* in the sense that the critical behavior of a continuous phase transition makes the underlying system insensitive to the microscopic details. In a mathematical point of view, all the observables become *scale invariant.* This implies that the dependency of observables on the system's scale can be described by power laws. To clarify further, when a system approaches a critical point, spatial and temporal fluctuations of the order parameter exhibit long-range correlations. In other words, the fluctuations take place in all scales as the correlation length ξ and correlation time τ_c diverge in the following form

$$\begin{aligned} \xi &\propto |t|^{-\nu}, \\ \tau_c &\propto \xi^z \propto |t|^{-\nu z}, \end{aligned}$$

where ν (z) denotes the correlation length (dynamical) critical exponent with t representing a dimensionless distance from the critical point. The divergence in correlation lengths ξ and τ_c is the mechanism behind the surprising phenomenon of universality. In fact, one can completely determine different *universality classes* based on the values of the *critical exponents.* Therefore, a large number of distinct physical systems can be labeled by the same universality class with certain critical exponents.

2.3.2 Quantum phase transition

A *quantum phase transition* (QPT), or phase transition at absolute zero temperature, i.e. $T = 0$, is rather driven by *quantum fluctuations* due to energy fluctuations arising from the uncertainty principle. Typically, QPT is discussed in terms of the ground states of closed systems. The *Ground-state phase transition* (GSPT) is associated with a non-analyticity in the ground-state energy induced by a small change in the coupling constants of the Hamiltonian. The *Steady-state phase transition* (SSPT) also happens in a similar fashion that its comparison with GSPT and TPT is presented in

	TPT	GSPT	SSPT
system operator	Hamiltonian $H^\dagger = H$	Hamiltonian $H^\dagger = H$	Liouvillian $\mathcal{L}$-Lindblad
relevant quantity	free energy $F(\rho) = \langle H \rangle_\rho - T\langle S \rangle_\rho$	energy eigenvalues $E_\psi : H\lvert\psi\rangle = E_\psi\lvert\psi\rangle$	Lindblad eigenvalues $\lambda_\rho : \mathcal{L}\rho = \lambda_\rho \rho$
state	Gibbs state $\rho_T = \underset{\rho\geq 0, \mathrm{Tr}(\rho)=1}{\arg\min} [F(\rho)]$ $\rho_T \propto \exp[-H/k_B T]$	ground state $\lvert\psi_0\rangle = \underset{\lVert\psi\rVert=1}{\arg\min}[\langle\psi\rvert H\lvert\psi\rangle]$ $[H - E_{\psi_0}]\lvert\psi_0\rangle = 0$	steady state $\rho_{\mathrm{ss}} = \underset{\lVert\rho\rVert_1=1}{\arg\min}[\lVert\mathcal{L}\rho\rVert_1]$ $\mathcal{L}\rho_{\mathrm{ss}} = 0$
phase transition	non-analyticity in $F(\rho_T)$	gap closing $E_{\psi_1} - E_{\psi_0} \to 0$	gap closing $\max[\mathrm{Re}(\lambda_\rho)] \to 0$

Table 2.2: Comparison of different types of phase transitions, namely the thermal phase transition, the ground-state phase transition, and the steady-state phase transition [22].

Table 2.2. There are of course other types of QPT such as dynamical and excited-state phase transitions which won't be covered in this thesis.

To gain a better understanding of QPT, it is instructive to look further into the notion of GSPT. Suppose the total Hamiltonian H of our quantum system is parameterized as $H = \lambda H_0 + (1 - \lambda) H_1$ with H_0 and H_1 being non-commuting Hamiltonians with distinct ground states, i.e. $[H_0, H_1] \neq 0$. Let's assume that the unitary operator U is a symmetry of H, i.e. $U^\dagger H U = H$. Now, by varying $0 \leq \lambda \leq 1$, the Landau's symmetry-breaking phase transition occurs if U leaves the ground state of H_0 but not H_1 invariant, i.e. $U|\Psi_0\rangle = |\Psi_0\rangle$ and $U|\Psi_1\rangle \neq |\Psi_1\rangle$. Symmetries in open systems can be similarly defined in terms of the Lindbladian. In this context, U is a symmetry if it commutes with the Hamiltonian and all the collapse operators, i.e. $[H, U] = [c_i, U] = 0$ for all i [23].

Chapter 3

Variational simulation of open quantum systems

3.1 Classical simulation methods

The description of (non-integrable) driven-dissipative many-body systems is one of the most challenging problems in condensed-matter physics in terms of theoretical and numerical approaches. The first issue with these systems comes from their dissipative nature. Crucially, the computational complexity of a full density matrix of an open many-body system scales as $\mathcal{O}(d^{2N})$ with N being the number of d-level particles. The factor 2 in the exponent comes from the matrix description of mixed states in contrast to the vector form of the pure states. Moreover, the non-equilibrium nature of these systems emerging from the interplay between dissipation and coherent dynamics is also intractable as the vast toolbox of equilibrium physics is not applicable anymore. There are several analytical and numerical approaches to circumvent these challenges that in the following we will address the most successful ones in the context of spin models, summarized in Table 3.1.

Mean-field treatment

Among the theoretical approaches in describing non-equilibrium many-body systems, the *mean-field method* is widely used as it is easy to implement. The main ingredient in the mean-field method is a derivation of an effective local Liouvillian by decoupling a system of interest from the rest [24, 25, 26]. This is possible by taking a partial trace of the Lindblad master equation resulting in the following single-body equations

$$\dot{\rho}_i = \mathrm{Tr}_{\not{i}}\{-i[H,\rho] + \mathcal{D}(\rho)\} = -i[\tilde{H}_i, \rho_i] + \tilde{\mathcal{D}}_i(\rho_i),$$

where $\tilde{H}_i$ and $\mathcal{D}_i$ represent the effective mean-field terms. This set of equations can be then solved for both the dynamics and the steady state. While the mean-field treatment of closed systems is exact in the limit of infinite dimensions, it is not always the case for dissipative systems [27]. Also, the mean-field solutions for open systems sometimes exhibit non-physical bistability in the steady state, known as *steady-state bistability*. This artifact comes from the non-linearity of the mean-field equations of motion that is at odds with more sophisticated methods [28].

Keldysh non-equilibrium field theory

A more systematic approach originates from a field-theoretical method known as *Keldysh non-equilibrium field theory* [29]. The basic idea behind the Keldysh formalism is to map the master equation, formulated in terms of second-quantized operators (using bosonic creation-annihilation representation of spin operators), into a Feynman path integral formulation (based on a backward-forward Trotterization of the time propagator). The resulting *Keldysh action* in the basis of coherent states is then treated by the powerful field-theoretical machinery giving access to a macroscopic description of the system. In particular, regarding the non-equilibrium steady states, extraction of a classical Langevin equation for the corresponding field fluctuations makes it possible to calculate the stationary properties [30].

Keldysh formalism demonstrates a successful application of the field theory to driven-dissipative systems leading to an analytical macro-description of the non-equilibrium problem in terms of symmetries and dimensionality. Also, it gives access to critical exponents and the determination of the universality class of the underlying critical behavior. However, this method is restricted to long-wavelength fluctuations in the vicinity of phase transitions where a mapping from the model of interest to a continuum-field theory is applicable.

Monte-Carlo wave-function method

As discussed earlier, a mixed state in the form of a density matrix is essentially a statistical ensemble of pure states. This allows breaking the quadratic complexity of a density matrix by decomposing it into (several) wave functions as their complexity is linear in terms of the Hilbert space dimension. Therefore, instead of evolving the whole density matrix through time, one can evolve individual pure states $|\psi_i\rangle$ to a desired time and then compute the expectation values of the observables according to $\langle O\rangle = \sum p_i \langle\psi_i|O|\psi_i\rangle$ where p_i's are obtained by standard *Monte-Carlo sampling.*

The main challenge in the *Monte-Carlo wave-function* (MCWF) method is the way that the individual trajectories should be evolved [17]. To this aim, we rewrite the Lindblad master equation in the following form,

$$\mathcal{L}(\rho) = -i\big(H_{\text{eff}}\rho - \rho H_{\text{eff}}^{\dagger}\big) + \sum_j c_j \rho c_j^{\dagger}, \tag{3.1}$$

where $H_{\text{eff}} = H - \frac{i}{2}\sum_j c_j^{\dagger} c_j$ represents an effective non-Hermition Hamiltonian describing the dissipative dynamics of the open system. Now, to implement the trajectory propagation using the effective Hamiltonian, one can follow the steps below:

1. Pick an initial pure state $|\psi(t_0)\rangle$;
2. Choose a random number $r \in [0,1]$, standing for the occurrence probability of a quantum jump;
3. Evolve the state using the effective Hamiltonian, $|\psi(t)\rangle = e^{-iH_{\text{eff}}t}|\psi(t_0)\rangle$, up to a time t_j where $\langle\psi(t_j)|\psi(t_j)\rangle = r$. Here, t_j denotes the time that a specific jump occurs, say c_n;
4. In order to determine c_n, calculate the probability $P_n = \delta p_n / p$ with n being the smallest value satisfying $P_n \geq r$, $\delta p_n = \sum_{k=1}^{n} \langle\psi(t_j)|c_k^{\dagger} c_k|\psi(t_j)\rangle$, and $p = \sum_{k=1} \langle\psi(t_j)|c_k^{\dagger} c_k|\psi(t_j)\rangle$;
5. Calculate the after-jump state, $|\psi(t_j{+}\delta t)\rangle = c_n|\psi(t_j)\rangle / \langle\psi(t_j)|c_n^{\dagger} c_n|\psi(t_j)\rangle$ with $\delta t \to 0$;
6. Replace $|\psi(t_0)\rangle$ with the new state $|\psi(t_j + \delta t)\rangle$ and repeat the steps.

In other words, in each iteration of the above algorithm (also known as *quantum jump formalism*), we first evolve an initial state using the effective Hamiltonian until a certain time when the norm of the evolved state becomes equal to a chosen random number. Exactly at this specific time, the state undergoes a quantum jump which abruptly changes the evolved state. Averaging over a large number of trajectories is then equivalent to the master equation.

Regarding the statistical errors arising from Monte-Carlo sampling, since the random numbers used in the algorithm are statistically uncorrelated and hence the independency of the trajectories, the error in the expectation value of an observable O scales as $\mathcal{O}(1/\sqrt{N_{\text{traj}}})$ with N_{traj} being the number of trajectories $N_{\text{traj}} \gg N$. For local observables in open systems, setting $N_{\text{traj}} = 500$ is enough to have a good statistical convergence. In particular, the largest system which has been studied so far, using highly parallel implementation of MCWF method, consists of 20 spin-1/2 sites with two-body interaction [31]. In Chapter 6, using the same technique we will present MCWF calculations for 22 spins in a purely dissipative setup ($H = 0$) with 3- and 6-local jump operators capable of generating long-range entanglement. In this thesis, for the numerical implementation of the MCWF method, we have used the open-source quantum toolbox in Python (QuTiP) [32].

Tensor network methods

Tensor network methods are one of the most powerful and versatile numerical methods for both closed and open quantum many-body systems. Within the tensor network family, *matrix product state* (MPS) demonstrates a highly accurate description of one-dimensional closed systems due to its connection with the notion of the *density matrix renormalization group* (DMRG) [33]. MPS is given by

$$|\Psi\rangle = \sum_{s_1,\dots,s_N=1}^{D} \mathrm{Tr}\{\prod_{i=1}^{N} A_i^{s_i}\}|s_1, s_2, \dots, s_N\rangle, \tag{3.2}$$

where $A_i^{s_i}$ represent matrices with dimension D, known as *bond dimension*, corresponding to the site i and the associated basis $|s_i\rangle$.

It is instructive to look at the entanglement entropy of MPS, as it provides a measure of the simulation efficiency of a quantum state on a classical computer. The entanglement entropy of a subsystem ρ_A in terms of the bond dimension reads as $S(\rho_A) \leq 2\log D$ which is totally independent of the system size. On the other hand, it has been shown that the typical ground states in one-dimensional systems (where the Hamiltonian is gapped and local) satisfy a constant entanglement entropy. This is in harmony with the MPS which enforces an upper bound on the amount of entanglement entropy. Generalization of MPS to mixed states is also possible by enlarging the Hilbert space using well-known techniques such as *vectorization* or *purification* [28].

Having said that, implementation of tensor network method for higher dimensions is challenging. This can be also understood by entanglement analysis. In general, the entanglement entropy satisfies the following *area law*,

$$S(\rho_A) \leq \mathcal{A}(\rho_A),$$

where $\mathcal{A}(\rho_A)$ represents the surface area of the subsystem. Consequently, extended versions of MPS to higher dimensions are faced with intrinsic restrictions [34, 35, 36]. Particularly, this is more pronounced in the case of open systems in the presence of weak dissipation [37].

Variational methods

Variational simulation is a versatile tool widely used to describe complex systems using an approximated but tractable parameterization of the states. In the context of open quantum systems, this refers to a parameterized density matrix in terms of a set of variational parameters, known as *variational ansatz*, which is chosen from the most relevant subset of the exponentially large Hilbert space. The variational parameters are then tuned in order to minimize a suitable *variational functional* resulting in an approximated description of the system. This formalism is justified according to the notion of *variational principle* which we will further discuss in the next section. Although the variational treatment is restricted to the structure of the given ansatz, it can provide a non-trivial estimation of both dynamical and static properties of open systems. Also, in spite of the conceptually simple structure of the variational methods, it sometimes outperforms very sophisticated methods.

There are several implementations of the variational treatment for open systems such as variational tensor network methods, variational quantum Monte-Carlo methods (reviewed in Ref. [28]) and even variational methods

	Advantages	Disadvantages
Mean-Field	computational simplicity	wrong prediction of bistability, wrong critical exponents
Keldysh	access to critical exponents	restricted to critical regions, challenging for spin systems
Monte-Carlo	exact for large number of trajectories	limited to small system sizes
Tensor Network	works well for inhomogeneous systems	issues with dimensionality, fails for weak dissipation
Variational	access to thermodynamic limit	ansatz dependent

Table 3.1: Comparison of classical simulation methods for driven-dissipative systems.

using artificial neural networks [38]. In the rest of this chapter, we will only focus on a specific version of the variational methods proposed in 2015 [39]. Developing this variational method will enable us to study different complex dissipative spin models with short- and long-range interactions.

3.2 Variational principle

Physics owes a lot to the extremum principles in nature. Initiated from Fermat's principle of least time in optics,

$$T = \int_{r_i}^{r_f} \frac{1}{v} dr \to \text{stationary},$$

where a light ray travels with the speed v a path from r_i to r_f in the shortest time. In a precise mathematical sense, the functional of time between two spacial points associated with the light path becomes stationary, or variations in the time functional vanishes $\delta T = 0$. Similarly, the motion of a physical system between two temporal points manifests itself in Hamilton's principle of stationary action in classical mechanics, i.e.

$$S = \int_{t_i}^{t_f} L\Big[x(t), \frac{dx(t)}{dt}, t\Big] dt \to \text{stationary},$$

where L is the corresponding Lagrangian of the system. Here, the action integral becomes stationary, i.e. $\delta S = 0$. This has preceded a significant breakthrough in the twentieth century leading to the famous Schrodinger equation in quantum mechanics inspired by de Broglie's wave-particle duality, and keeping up with the Feynman's path integral formulation inspired by Dirac's idea of infinite quantum trajectories.

Extremum principles have opened up the possibility of variational formulation of complex problems in different branches of physics. Particularly in quantum mechanics, several variational principles have been developed to tackle computationally hard problems of describing exponentially large quantum states using approximated solutions. In the context of closed many-body systems, there are two different classes of variational principles associated with the static problem of finding a ground state and simulation of the real-time coherent dynamics. The former is addressed by *Rayleigh-Ritz* method as a minimization of the following energy functional

$$\langle \psi_v | H | \psi_v \rangle \to \min .$$

The ground state is then chosen such that it minimizes this functional. Indeed, due to the exponential growth of Hilbert space, ψ_v is designed as a subset of the whole Hilbert space. For the simulation of the time evolution, one can employ the *time-dependent variational principle*, extracted using an application of the Euler-Lagrange equation over the following Lagrangian,

$$L = \langle\psi_v|(\frac{d}{dt} + iH)|\psi_v\rangle,$$

that essentially minimizes a norm defined over the Schrödinger equation [40]. The rest of this chapter is dedicated to the notion of the variational principle for open quantum many-body systems.

3.2.1 Gutzwiller theory for open systems

The basic idea for establishing a variational principle for open quantum systems is to take a variational trial state and compute the approximated dynamics it will generate by computing its time derivative $\dot{\rho} = \mathcal{L}\rho$ according to the underlying quantum master equation [39]. In analogy to closed systems where the ground states are out of interest, steady-state properties of open systems are often prior to the dynamical properties. To this aim, a variational functional is needed to be minimized for steady states $\rho_{\text{ss}} \equiv \lim_{t\to\infty} \rho(t)$. This functional arises from a variational principle for the steady states [39] equipped with a suitable norm of the corresponding Liouvillian, i.e.

$$\rho_{\text{ss}} = \arg\min_{\rho} \|\mathcal{L}\rho\| \,. \tag{3.3}$$

To approximate ρ_{ss}, we consider a *Gutzwiller variational ansatz* for a N-body system given by

$$\rho_{\text{var}} = \prod_{i=1}^{N} \rho_i, \tag{3.4}$$

in which all the correlations are neglected to decrease the complexity of the underlying many-body problem. Any local density matrix in this ansatz, i.e. ρ_i, is then decomposed in terms of suitable orthogonal matrices. This enables a systematic variational treatment of the ansatz by treating the coefficients of these matrices as a set of variational parameters. In the case of spin-1/2 systems, ρ_i is expanded in terms of Pauli matrices σ_μ as in Eq. (2.3). Now the state of each spin-1/2 particle ρ_i, can be determined by three independent variables,

$$\boldsymbol{\alpha}_i = \Big\{\langle\sigma_x^{(i)}\rangle, \langle\sigma_y^{(i)}\rangle, \langle\sigma_z^{(i)}\rangle\Big\} = \Big\{\alpha_x^{(i)}, \alpha_y^{(i)}, \alpha_z^{(i)}\Big\}. \tag{3.5}$$

These parameters can be obtained by minimizing a suitable variational norm $\|\mathcal{L}\rho\|$. Particularly, we will focus on two popular matrix norms namely 1-norm or *trace norm*,

$$\|A\|_1 = \mathrm{Tr}\Big[\sqrt{A^\dagger A}\Big],$$

and 2-norm or *Hilbert-Schmidt (HS) norm*,

$$\|A\|_2 = \sqrt{\mathrm{Tr}\big[A^\dagger A\big]}.$$

The trace norm is equivalent to the sum over eigenvalues of $\sqrt{A^\dagger A}$ whereas the HS norm is simply the square root of the trace of $A^\dagger A$. The former is computationally unfavorable due to the cost of matrix diagonalization, and the latter is biased toward maximally mixed state [39]. However, the bias of the HS norm can be cured using normalization by the purity similar to the approach introduced in Ref. [41]. In this thesis, we mostly use the HS norm as its advantage compared to the trace norm is threefold; (i) The HS norm is easier to compute since no diagonalization is needed, (ii) It's possible to obtain it analytically due to its definition, (iii) and most importantly it can capture continuous phase transitions while the trace norm is favoring first-order transitions. In the following, we will first estimate the variational cost function for homogeneous systems and then we will derive an upper bound of the function for a general Inhomogeneous system.

Homogeneous systems

Here, we consider a cost function being derived from the inner product $\langle\!\langle \mathcal{L}^\dagger(\rho) | \mathcal{L}(\rho) \rangle\!\rangle$ where $|A\rangle\!\rangle$ denotes a $mn \times 1$ vector contained by flattening a $m \times n$ matrix A. The inner product of vectorized operators is compatible with the HS norm according to the following relation

$$\mathrm{Tr}\{A^\dagger B\} = \langle\!\langle A^\dagger | B \rangle\!\rangle, \tag{3.6}$$

which means $\|\mathcal{L}(\rho)\|_2^2 = \langle\!\langle \mathcal{L}^\dagger(\rho) | \mathcal{L}(\rho) \rangle\!\rangle$. Crucially, to circumvent the bias of the HS norm, we normalize the inner product by the total purity $\mathrm{Tr}\big[\rho^2\big] = \langle\!\langle \rho | \rho \rangle\!\rangle$, i.e.

$$F_v = \frac{\langle\!\langle \mathcal{L}^\dagger(\rho) | \mathcal{L}(\rho) \rangle\!\rangle}{\langle\!\langle \rho | \rho \rangle\!\rangle}. \tag{3.7}$$

For a given (uniform) Liouvillian we can express the numerator as an expansion of its individual terms. These terms comprise the geometrical different configurations as it is shown in Fig. 3.1, that in turn can be factorized by some N- and N^2-dependent coefficients. The N-dependent configurations correspond to the overlapping terms in $\langle\!\langle \mathcal{L}^\dagger(\rho)|\mathcal{L}(\rho)\rangle\!\rangle$, and the N^2-dependent configurations represent non-overlapping terms. In addition, these coefficients also encode the lattice dimensionality via their dependency on the coordination number z. As a further step to have a scale-independent variational norm, we treat these coefficients on the same footing, rescaling the N-dependent terms to N^2 and then normalize the whole function by N^2.

As a result, the variational norm can be cast into the form

$$f_v = \sum_{ij} \frac{\langle\!\langle \tilde{\mathcal{L}}_i^\dagger(\rho)|\tilde{\mathcal{L}}_j(\rho)\rangle\!\rangle}{\langle\!\langle \rho_0|\rho_0\rangle\!\rangle^{n_{ij}}}, \tag{3.8}$$

where a uniform solution $\prod \rho_0$ is assigned to the many-body state assuming translational invariance in the underlying system ($\rho_i = \rho_j$ for all i and j). Also, $\tilde{\mathcal{L}}_i$'s denote the individual terms in the Liouvillian, similar to what is depicted in Fig. 3.1, and the denominator represents the local purity $\langle\!\langle \rho_0|\rho_0\rangle\!\rangle$ to the power of n_{ij} being the total dimension of the terms in the numerator.

Notably, in the case of having uniform couplings in the Lindblad master equation, analytical evaluation of the variational norm f_v is possible even in the thermodynamic limit. This resembles a similar treatment in the context of closed quantum systems where the ground-state energies can be estimated by Gutzwiller energies [42]. It is worth mentioning that following the same procedure using the more natural trace norm imposes additional approximations which we will discuss shortly.

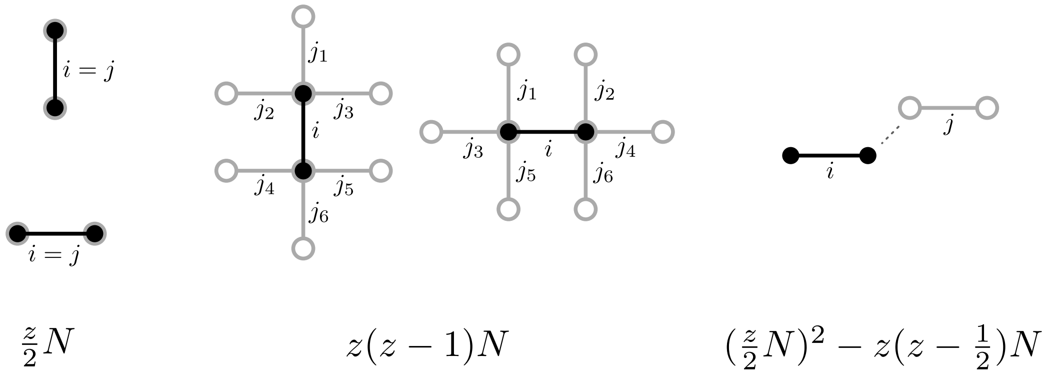

Figure 3.1: Spatial configurations corresponding to a 2-local Liouvillian appearing on a 2D lattice with the coordination number $z = 4$. The black 2-dot lines labelled with i represent $\langle\!\langle \tilde{\mathcal{L}}_i^\dagger(\rho)|$ and the gray lines labelled with j represent $|\tilde{\mathcal{L}}_j(\rho)\rangle\!\rangle$ in the HS norm.

In Chapter 4, we will show how this conceptually simple approach enables us to resolve the controversial issue of steady-state bistability in open quantum systems.

Inhomogeneous systems

As shown in the previous section, the variational function for short-range interacting open quantum systems is predominately determined by the semi-local configurations, depicted in Fig. 3.1. Intuitively, this allows finding an upper bound of the variational function by recasting the many-body system in terms of local batches of the whole system. This idea has been proposed in Ref. [39] for the steady state of dissipative systems which outperforms the mean-field-like methods in detecting steady-state phase transitions. In the following, we will briefly review this treatment.

Starting from the variational principle in Eq. (3.3), we want to approximate the true steady state using a variational ansatz by minimizing the following cost function

$$\|\mathcal{L}\rho\| = \|-i[H,\rho] + \mathcal{D}(\rho)\| \to \min,$$

which indeed vanishes in the case of having an exact ansatz including all the possible correlations. however, we again employ the Gutzwiller ansatz described in Eq. (2.3) to approximate the exact state. Now, substituting Gutzwiller ansatz on the right-hand side of the equation yields

$$\|\mathcal{L}\rho\| = \left\| \sum_i \mathcal{R}\dot{\rho}_i + \sum_{\langle ij\rangle} \mathcal{R}\dot{C}_{ij} \right\|, \tag{3.9}$$

where $\dot{\rho}_i \equiv \mathrm{Tr}_{\not{i}}\{\mathcal{L}\rho\}$ defines the time derivative of a single-site density matrix and $\dot{C}_{ij}$ denotes the time derivative of the nearest-neighbour two-body correlations. Here, the underlying assumption is that the Liouvillian is at most 2-local, although generalization to more than 2-local cases is straightforward. Also, we have to mention that the appearance of $\dot{C}_{ij}$ is only because of the master equation, despite the lack of any correlation in the ansatz. Evaluation of the full norm in Eq. (3.9) is still an exponentially hard problem. In order to circumvent this issue, the norm can be upper bounded by a computable function in the following form

$$\|\mathcal{L}\rho\| \leq \sum_{\langle ij\rangle} \left\|\mathcal{R}\left(\dot{\rho}_i \otimes \rho_j + \rho_i \otimes \dot{\rho}_j + \dot{C}_{ij}\right)\right\| = \sum_{\langle ij\rangle} \|\mathcal{R}\dot{\rho_{ij}}\|.$$

After considering the unbiased trace norm and two-time application of the triangle inequality (fully discussed in Ref. [43]), one can obtain the variational norm as follows

$$f_v = \sum_{\langle ij \rangle} \|\dot{\rho}_{ij}\|_1 \,. \tag{3.10}$$

The operators on the right-hand side of this inequality act on exponentially small subspaces of the full Hilbert space which is why it can be efficiently minimized using standard numerical techniques.

Regarding the variational ansatz, one can also add short-range correlations into it leading to tighter upper bounds using a similar derivation. However, while including correlation for short-range interacting systems might change the position of phase transitions, it usually does not alter the qualitative behavior of them [39]. Therefore, the usage of the Gutzwiller ansatz is justified as it can describe phase transition up to quantitative uncertainties.

The upper-bound treatment makes it possible to also look at the dynamics of open systems. Similar to closed systems, numerical integration of the master equation gives rise to an operational definition of the time-dependent variational principle for open systems [44] that in the case of implicit midpoint integration has the following form

$$\left\| \rho(t+\tau) - \rho(t) - \frac{\tau}{2}\mathcal{L}[\rho(t+\tau) + \rho(t)] \right\| \to \min \,.$$

The error generated from the time-step integration scales as $\mathcal{O}(\tau^3)$, that can be improved using higher-order methods such as Runge-Kutta. This method has been used for the investigation of both short- and long-range interacting open systems which are covered in Refs. [43, 45].

3.2.2 Beyond Gutzwiller treatment

Here, we extend the variational principle for dissipative many-body systems to the regime of long-range interactions and correlations. Regarding the variational ansatz, we only include two-body long-range correlations and ignore higher-order correlations. This is justified according to the *BBGKY hierarchy* (Bogoliubov-Born-Green-Kirkwood-Yvon hierarchy) for correlation operators [25] asserting that in dissipative dynamics higher-order correlations decay faster than two-body terms. The variational ansatz is given by

$$\rho_{\text{var}} = \prod_{i=1}^{N} \rho_i + \sum_{i<j} \mathcal{R}C_{ij}, \tag{3.11}$$

where $C_{ij} = \rho_{ij} - \rho_i \otimes \rho_j$ denotes long-range correlations. We now express the generic form of ρ_i and C_{ij} in terms of variational parameters α_μ and variational ansätze $\zeta_{ij}(\mu, \nu)$ respectively

$$\rho_i = \frac{1}{2}\Big(\mathbb{1}_i + \sum_{\mu \in \{x,y,z\}} \alpha_\mu \sigma_\mu^{(i)}\Big), \tag{3.12a}$$

$$C_{ij} = \frac{1}{4} \sum_{\substack{\mu,\nu \in \\ \{x,y,z\}}} \zeta_{ij}(\mu,\nu) \sigma_\mu^{(i)} \sigma_\nu^{(j)}, \tag{3.12b}$$

where σ_μ's represent the Pauli matrices. Crucially, one has to define variational functions $\zeta_{ij}(\mu, \nu)$ such that they preserve long-range effects of correlations but with the minimum number of variational parameters in order to reduce numerical complexity of the minimization. Therefore, when it comes to long-range interacting systems our variational functions become model-dependent. An explicit form of these functions for a dissipative variant of Rydberg gases will be presented in Chapter 5. Regarding the variational norm, we again exploit the inner-product representation of the HS norm, i.e.

$$\begin{aligned} \|\dot{\rho}_{\text{var}}\|_2^2 =& \langle\langle \mathcal{L}^\dagger(\rho_{\text{var}}) | \mathcal{L}(\rho_{\text{var}}) \rangle\rangle \\ \approx& G_p(N-4) \sum_{i<j} \sum_{k<l} \langle\langle \mathcal{L}_{ij}^\dagger(\rho_{\text{var}}^{(ijkl)}) | \mathcal{L}_{kl}(\rho_{\text{var}}^{(ijkl)}) \rangle\rangle, \end{aligned} \tag{3.13}$$

where $G_p(N) = \langle\langle \rho_{\text{var}} | \rho_{\text{var}} \rangle\rangle$ is the total purity of the steady state and

$$g_p = \langle\langle \rho_0 | \rho_0 \rangle\rangle = (1 + \alpha_x^2 + \alpha_y^2 + \alpha_z^2)/2, \tag{3.14}$$

is the single-site purity. The approximation in Eq. (3.13) comes from the exclusion of the marginal correlations, i.e. we assume $\rho_{\text{var}}^{(ijklm)} = \rho_{\text{var}}^{(ijkl)} \otimes \rho_{\text{var}}^{(m)}$. Next, we define our variational cost function similar to Eq. (3.7) that reads as

$$F_v(\alpha) \equiv \frac{\|\mathcal{L}\rho\|_2}{G_p(N)}. \tag{3.15}$$

To find a computable variational norm f_v, we expand the Liouvillian in terms of local and interacting terms, i.e. $\mathcal{L}_{ij} = \sum_i \tilde{\mathcal{L}}_i + \sum_{i<j} \tilde{\mathcal{L}}_{ij}$, where in the latter for the sake of simplicity we assume binary interactions. Finally, the (squared) variational norm can be expressed as in the following form,

$$
\begin{aligned}
f_v^2 = g_p^{-2} &\sum_{1\neq j} \langle\!\langle \rho_{\text{var}}^{(1j)} | \tilde{\mathcal{L}}_1^\dagger \tilde{\mathcal{L}}_1 + \tilde{\mathcal{L}}_1^\dagger \tilde{\mathcal{L}}_j | \rho_{\text{var}}^{(1j)} \rangle\!\rangle \\
+ g_p^{-3} &\sum_{1\neq j\neq k} \langle\!\langle \rho_{\text{var}}^{(1jk)} | 2\tilde{\mathcal{L}}_1^\dagger \tilde{\mathcal{L}}_{1j} + \tilde{\mathcal{L}}_1^\dagger \tilde{\mathcal{L}}_{jk} | \rho_{\text{var}}^{(1jk)} \rangle\!\rangle \\
+ g_p^{-4} &\sum_{1\neq j\neq k\neq l} \langle\!\langle \rho_{\text{var}}^{(1jkl)} | \frac{1}{2}\tilde{\mathcal{L}}_{1j}^\dagger \tilde{\mathcal{L}}_{1j} + \frac{1}{2}\tilde{\mathcal{L}}_{1j}^\dagger \tilde{\mathcal{L}}_{jk} + \frac{1}{2}\tilde{\mathcal{L}}_{1j}^\dagger \tilde{\mathcal{L}}_{1k} + \frac{1}{4}\tilde{\mathcal{L}}_{1j}^\dagger \tilde{\mathcal{L}}_{kl} | \rho_{\text{var}}^{(1jkl)} \rangle\!\rangle,
\end{aligned}
\tag{3.16}
$$

where here we made the approximation that $G_p(N) \approx G_p(N-n) g_p^n$ which is valid for $N \gg n$. Here, n denotes the dimension of the variational states ρ_{var} appearing in the variational norm.

Evaluation of f_v in the thermodynamic limit is still not feasible. However, one can instead perform finite-size scaling as it is consistent with the fact that long-range interactions typically decay by a power-law form. Importantly, As we will show in Chapter 5, the non-analyticity of the variational norm at the phase transition appears even for finite sizes. This is because the system size in this context is, in fact, corresponding to the size of an infinitely repeated array of a finite batch or cluster of sites. In this sense, the variational method can be thought of as a cluster-based approach, see e.g. [46]. From a geometrical point of view, we try to minimize the estimation error in the bulk of the clusters while neglecting the error arising on the surfaces. The latter is justified in the limit of a large cluster size. Therefore, our variational method in combination with a proper finite-size analysis can be utilized to approximate the non-equilibrium steady states of long-range interacting quantum systems, especially to detect phase transitions.

3.3 Quantum simulation

Until now, we have only talked about numerical simulation methods using a classical computer. However, the ultimate goal in the field of quantum simulation is to take advantage of controllable quantum simulators to emulate another quantum system. There are essentially two different approaches that are widely used in this regard. *Analogue quantum simulation* is the first approach where a quantum simulator should be specifically engineered such that it can imitate the physical behavior of the model of interest. This of course requires a direct realization of the model's Liouvillian given the available quantum resources. Clearly, this approach cannot be used for a general simulation due to the typically restricted quantum resources.

The second approach which does not suffer from this issue is the so-called *digital quantum simulation.* Here, the corresponding time propagator of the desired model is broken down into a long sequence of gate operations. This process is usually called *Trotterization* due to the Suzuki-Trotter approximation of a global evolution operator $H = A + B$, i.e.

$$e^{-iH\tau} = e^{-iA\tau/2}e^{-iB\tau}e^{-iA\tau/2} + \mathcal{O}(\tau^3), \tag{3.17}$$

where here the individual terms of the H do not commute, $[A, B] \neq 0$. Trotterization is shown to be efficient to simulate local quantum systems providing small (digital) time steps τ [47]. The advantage of this approach is that in principle all the resulting digitized propagators can be recast into a set of semi-local universal gates, leading to universal quantum simulation. In addition, error correction schemes can also be applied in each time step for fault-tolerant computations. The main challenge for digital simulation is the implementation of high-fidelity universal gates since many repetitions of the gates are required.

In general, the analog/digital simulation of complex quantum systems might be challenging via the available quantum resources also known as *noisy intermediate-scale quantum* (NISQ) devices comprise 50-100 noisy qubits [48]. Considering the current situation in terms of quantum computational devices, neither Liouvillian engineering for analog simulation is generally possible, nor arbitrarily long sequences of digital logic gates with high fidelity are within reach. However, recently developed techniques for the variational preparation of quantum states [49, 50, 51], also known as *variational quantum simulation* (VQS), opens up the possibility of overcoming this challenge.

Within the VQS scheme, a hybrid classical-quantum machine is employed to approximately reproduce variant quantum states without explicit realization of the corresponding unitaries. In other words, VQS is a combined analogue-digital quantum simulation in which a shallow parameterized quantum circuit generates some trial states by minimizing a corresponding cost function of some measurement outputs on a classical computer. Basically, a classical processor performs the minimization procedure in the variational simulation while the trial variational states are generated by accessible quantum hardware (also known as *quantum co-processor*) in the form of a circuit ansatz.

3.3.1 Dissipative variational quantum simulation

Here, we present an adapted VQS scheme to be able to realize Markovian evolution of arbitrary large open quantum many-body systems. To this end, we employ the Lindblad quantum master equation in the Heisenberg picture, i.e.

$$\frac{dO}{dt} \equiv \mathcal{L}_H O = i\big\langle [H,O] \big\rangle + \sum_i^N \Big\langle L_i{}^\dagger O L_i - \frac{1}{2}\big\{L_i^\dagger L_i, O\big\}\Big\rangle, \tag{3.18}$$

which describes the time evolution of an observable O caused by a Hamiltonian H and a set of jump operators $\{L_i\}$ modeling the target open system. The strategy behind our dissipative variant of VQS is to prepare the state $\rho(t+\tau)$ at time $t+\tau$ using a parameterized circuit ansatz, given the state $\rho(t)$ evolving according to the Lindblad master equation. The circuit ansatz generates different trial states that among them the desired state is determined by minimizing a proper cost function. This is similar to the procedure introduced in Section 3.2.1 and other relevant studies both in the Schrödinger picture [44] and in the Heisenberg picture [52]. Similarly, we introduce a variational cost functional F_H based on the implicit midpoint integration of Eq. (3.18), given by

$$F_H \equiv \sum_i \Big| \big\langle O_i(t+\tau) \big\rangle - \big\langle O_i(t) \big\rangle - \frac{\tau}{2} \mathcal{L}_H [O_i(t) + O_i(t+\tau)] \Big|, \tag{3.19}$$

where the sum runs over all orthogonal observables including non-local operators. However, we use a truncation scheme by ignoring the terms for high-order observables. Achieving accurate results using a subset of observables has been numerically verified [52].

Within a classical variational treatment, we need a trial (mixed) state to compute the expectation values of the observables that appear in the cost function. Crucially, due to the exponential growth of Liouvillian space by increasing the system size, classical simulation of the corresponding quantum state is not generally possible when it comes to large system sizes. Here, VQS comes into the picture as a quantum co-processor capable of generating trial states given a set of variational parameters which is calculated on a classical computer by minimizing the relevant cost function. During this feedback loop, if the convergence conditions are satisfied, then the last trial state is the solution.

The quantum co-processor is basically a variational quantum circuit composed of multiple layers of unitary and non-unitary propagators with temporal phases treated as variational parameters. A parameterized layer n out of d layers, known as *circuit depth*, with a vector $\boldsymbol{\theta}_n$ evolves an input state according to $\rho_n = \mathcal{G}_{\boldsymbol{\theta}_n}(\rho_{n-1})$ where $\mathcal{G}$ denotes a quantum operation given by

$$\mathcal{G} = \prod_{k=1}^{N} \big[\mathcal{D}_k^a \mathcal{R}_k^{x,y,z}\big] \mathcal{U}_g. \tag{3.20}$$

As it is shown in Fig. 3.2, the quantum circuit consists of global propagators

$$\mathcal{U}_g(\rho) = e^{-iH_0\theta}\rho e^{+iH_0\theta}, \tag{3.21}$$

which can generate entanglement depending on the quantum resource Hamiltonian H_0. Additionally, the variational state can undergo general local rotations (for example by controllable focused laser beams in trapped ions) denoted by

$$\mathcal{R}_k^\alpha(\rho) = e^{-i\sigma_\alpha^{(k)}\theta}\rho e^{+i\sigma_\alpha^{(k)}\theta}, \tag{3.22}$$

with $\alpha \in \{x, y, z\}$, or

$$R_x(\theta) = e^{-i\sigma_x\theta} = \begin{pmatrix} \cos\theta & -i\sin\theta \\ -i\sin\theta & \cos\theta \end{pmatrix}, \tag{3.23a}$$

$$R_y(\theta) = e^{-i\sigma_y\theta} = \begin{pmatrix} \cos\theta & -\sin\theta \\ \sin\theta & \cos\theta \end{pmatrix}, \tag{3.23b}$$

$$R_z(\theta) = e^{-i\sigma_z\theta} = \begin{pmatrix} e^{-i\theta} & 0 \\ 0 & e^{-i\theta} \end{pmatrix}. \tag{3.23c}$$

In fact, just having only two of the three Pauli rotations is sufficient to cover the whole surface of the Bloch sphere. Even in particular cases, one Pauli rotation suffices as in the experiment reported in Ref. [51]. Typically, the local rotations are chosen in such a way to preserve the symmetries of the target model. So far, the variational circuit is only capable of producing pure states. Here, we extend the scope of the variational elements by incorporating non-unitary operations so that even mixed states become accessible. In particular, we take into account the conventional local dissipative channels which are mostly realizable even with the available quantum resources. Similar to the case of unitary rotations, the type of the channels will be determined according to the target problem. Here, as an example, we equip the circuit with the ordinary amplitude damping channel D_d. The corresponding operator-sum representation is given by

$$\mathcal{D}_d(\rho) = \frac{1}{N}\sum_{j=1}^{N}\Big[D_1^{(j)}\rho D_1^{(j)\dagger} + D_2^{(j)}\rho D_2^{(j)\dagger}\Big], \tag{3.24}$$

with

$$D_1 = \begin{pmatrix} 1 & 0 \\ 0 & \sqrt{e^{-\gamma\tau}} \end{pmatrix}, \tag{3.25a}$$

$$D_2 = \begin{pmatrix} 0 & \sqrt{1 - e^{-\gamma\tau}} \\ 0 & 0 \end{pmatrix}, \tag{3.25b}$$

where $D_2^{(j)}$ describes an increase in the ground state of a resource qubit j via a decay process $\sigma_- = |0\rangle\langle 1|$ with a rate γ whereas $D_1^{(j)}$ leaves the ground state invariant while de-populating the excited state. The factor $1/N$ appears due to the completeness relation of Kraus operators so that the channel becomes trace-preserving. As mentioned before, the temporal phases τ appearing in all the circuit operations are treated as (different) variational parameters. In Chapter 7, we will explicitly determine the circuit architecture for particular models.

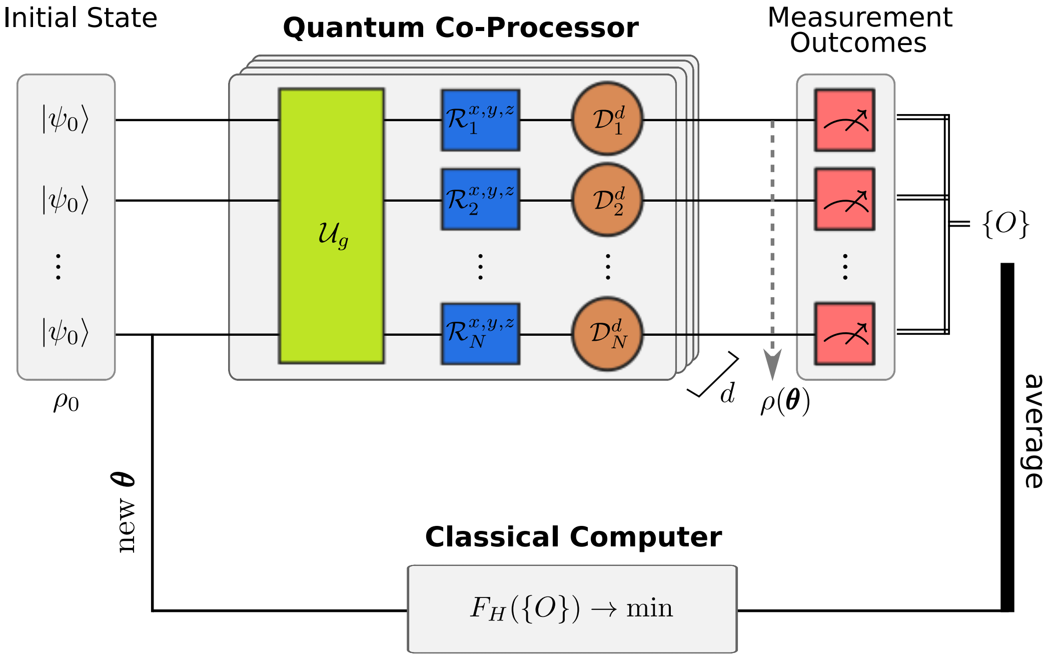
Initial State
Quantum Co-Processor
Measurement Outcomes
$|\psi_0\rangle$
$|\psi_0\rangle$
$|\psi_0\rangle$
ρ_0
$\mathcal{U}_g$
$\mathcal{R}_1^{x,y,z}$
$\mathcal{R}_2^{x,y,z}$
$\mathcal{R}_N^{x,y,z}$
$\mathcal{D}_1^d$
$\mathcal{D}_2^d$
$\mathcal{D}_N^d$
d
$\rho(\boldsymbol{\theta})$
$\{O\}$
average
new $\boldsymbol{\theta}$
Classical Computer
$F_H(\{O\}) \to \min$

Figure 3.2: A diagram of the variational quantum simulation scheme. The quantum co-processor generates a trial quantum state for N qubits given a product initialized state $\rho_{\text{in}} = \prod_{i=1}^{N} |\psi_0\rangle\langle\psi_0|$ and a set of variational parameters $\boldsymbol{\theta}$ encoded into the temporal phases of the variational circuit's ingredients, i.e., global resource unitary, $\mathcal{U}_g(\boldsymbol{\theta})$, local Pauli rotations $\mathcal{R}(\boldsymbol{\theta})$, and local dissipation channels $\mathcal{D}_d(\boldsymbol{\theta})$.

3.3.2 Quantum simulation platforms

We now briefly review the relevant properties of the most promising quantum platforms for variational quantum simulation. Here, we only address those simulators capable of individual controllability, tunable coupling and high-fidelity read-out which are necessary for variational treatment. In particular, we focus on only three distinctive platforms namely *superconducting circuits* (SC), *trapped ions*, and *Rydberg atoms*, see the Table 3.2. Crucially, in all the following quantum platforms, long-range Ising-type interactions can be engineered to be used as the global entangling propagator in VQS. Indeed there are also other types of simulators with promising advances such as photonic-based platforms [49, 53] that are still under development.

Superconducting circuits

Superconducting circuits being coupled by *electrical resonators* are basically the electric-circuit analog of cavity quantum electrodynamics where the interaction between matter and quantized electromagnetic fields is studied using natural atoms and optical cavities. Although there are several implementations of SC qubits, the main ingredient in all of them is a connection of superconducting islands via the so-called *Josephson junction* where a thin insulating film is sandwiched between two superconducting electrodes. This allows a quantum tunneling of the so-called *Cooper pairs* of electrons, formed in superconducting electrodes, through the insulating barrier. As a result, SC (as a macroscopic object) show discrete energy levels which are used to

	Rydberg atoms	Trapped ions	Superconducting circuits
Qubit	highly excited states of alkali atoms	electronic energy levels of ions	charge states in superconducting islands
Coupling	dipole-dipole	Coulomb-coupled motion	electrical resonance
Readout	optical pumping	optical pumping	electrical resonator
Advantages	programmable geometries, scalability	long coherence time, tunable interactions	fast gate operation, on-chip fabrication
Challenges	short coherence time, lifetime barrier	restricted to 1D, intrinsic scalability issues	limited connectivity, requires extremely low temperature

Table 3.2: Comparison of available experimental platforms for variational quantum simulation.

encode quantum information. The manipulation of circuits is then possible by applying voltages (typically in micro-volts) and currents.

The typical resource Hamiltonian for charged qubits in SC engineered for spin models [54] reads

$$H_{\mathrm{SC}} = -\sum_i \Delta_i \sigma_i^z - \sum_{i<j} J_{ij} \sigma_i^x \sigma_j^x, \tag{3.26}$$

where Δ_i is the qubit splitting and J_{ij} is the interaction strength between qubits i and j. This resource Hamiltonian has been recently employed on a 12-qubit superconducting quantum processor for variational quantum preparation of many-body eigenstates [55]. Also, a first-time variational realization of a non-Abelian gauge theory has been conducted using IBM superconducting quantum computer [56]. Other variants of the Hamiltonian have been also used to estimate ground state properties of simple molecules using 6 qubits [57, 58].

The advantage of SC qubits is that they can be fabricated on a large scale on electronic chips adopted from well-developed techniques and tools in micro-electronics. The first experimental realizations of quantum supremacy have been conducted using the SC platform [59, 60]. However, one of the main challenges of this platform is the requirement of extremely low temperature that is necessary to maintain superconducting features. In addition, since controlling and coupling SC qubits usually need dense current-carrying wiring, connectivity of qubits in superconducting chips at large scales is an intrinsic issue.

Trapped ions

Trapped ions are one of the most controllable and coherent quantum simulation platforms. This platform is originally proposed in a seminal work in 1995 as a realistic physical implementation of a quantum computer [61]. The first experimental realization of this proposal has been accomplished in 2003 to implement a CNOT gate [62]. This is still a highly active field of research in quantum simulation that at the moment 50-qubit trapped ion platforms with high-fidelity operations are constructed [63, 51]

Cold trapped ions (such as Al^+, Ca^+, Mg^+) are basically laser-driven ions being stored in electromagnetic traps. Experimentally, first, hot vaporized atoms are guided into a vacuum chamber and get ionized by electron bombardment. The resulting atomic ions are then confined using electromagnetic fields generated by a set of nearby electrodes. Next, laser cooling of the ions takes place to suppress thermal fluctuations. This results in a localized crystalline structure where the repulsive Coulomb forces cancel out the external trapping forces.

Specific degrees of freedom of trapped ions can be manipulated using external interventions. Particularly, driving the ions into different internal electronic states is possible by appropriate laser irradiation. Typically, these electronic states are chosen to be either hyperfine levels corresponding to atomic s-orbital states or optical levels corresponding to s- and d-orbital levels. Both *hyperfine qubits* and *optical qubits* are scalable as long as there are no inhomogeneities in terms of electromagnetic fields which might modify the energy levels. In addition to the internal states, the ions have external degrees of freedom which correspond to their motions inside the trap. This is due to the momentum transfer as a result of photon absorption of the ions. Elimination of the collective vibrational modes (phonons) with high energies clears the way to have an effective spin-1/2 description of the ions.

Now, to perform a simulation, the qubits should be first initialized, then interact, and finally be measured. For both initialization and read-out, *optical pumping* is employed. Here, a qubit state (say $|1\rangle$) is resonantly driven to some short-lived excited p-states. Exploiting additional laser drive, these states spontaneously decay to some ground states except $|0\rangle$ due to specific spin selection rules. Ultimately, the qubit will be initialized into $|0\rangle$ and the emitted photons can be detected by CCD cameras as a read-out process. Regarding the interaction of the qubits, the Coulomb interaction between ions couple the qubit states to the phonons which makes it possible to manipulate the coupling through laser driving of individual ions. Manipulation of individual ions (by optical addressing techniques) is also doable thanks to the micrometer distances between ions in a typical ion trap.

The effective spin model arises from this setup is described by an approximated XX Hamiltonian with long-range interaction in the following form

$$H_{\text{ion}} = \frac{B(t)}{2}\sum_i \sigma_z^{(i)} + J_0 \sum_{i<j} \frac{\sigma_x^{(i)}\sigma_x^{(j)}}{r_{ij}^{\alpha}}, \tag{3.27}$$

where B indicates an effective magnetic field, J_0 denotes the strength of long-range interactions with a tunable power-law exponent, i.e. $0 \leq \alpha \leq 3$, and r_{ij} is the spatial distance between the qubits i and j. In the regime of $B \gg J_0$, the Hamiltonian can be approximately converted into an XY Hamiltonian using perturbation theory, which has been used as the resource Hamiltonian in a variational quantum simulation of a one-dimensional lattice gauge theory [51]. In general, different variety of interacting spin models have been implemented using trapped ions like the Heisenberg model

$$H_{\text{Heis}} = \sum_{i<j} \sum_{\mu \in \{x,y,z\}} J_{ij}^{\mu} \sigma_{\mu}^{(i)} \sigma_{\mu}^{(j)},$$

from which different sub-classes like XXZ ($J_{ij}^{x} = J_{ij}^{y}$) and XY ($J_{ij}^{z} = 0$) can be extracted, reviewed comprehensively in Ref. [64].

Although trapped ion simulators demonstrate long coherence time and high-fidelity in initialization, localization, and measurement of qubits, they suffer from several limitations. Firstly, they are mostly restricted to one-dimensional lattices due to the specific shape of the Paul traps. Extension to higher dimensions is very challenging as the ions can sit out of the radio frequency null of the traps giving rise to less technical controllability. But, efforts in utilizing other possible trapping technologies are in progress [65, 66]. Secondly, the current trapped-ion simulators have intrinsic scalability issues arising from the fact that the qubit-phonon coupling degrades by increasing the number of ions which in turn slows down two-qubit operations. However, several solutions have been proposed to overcome these challenges, described in more detail in Ref. [67].

Rydberg atoms

Rydberg atoms are neutral (usually alkali) atoms in which one electron is excited close to the *ionization threshold* where principal quantum number n is very high ($n > 20$). This is associated with a huge expansion of the size of Rydberg atoms (relative to ground-state ones) which results in several exaggerated features. The main features consist of a long radiative lifetime of Rydberg states scaling as n^3, high sensitivity to electrical fields due to strong polarisability scales as n^7 and giant van der Waals interaction which its rate scales as n^{11}. The scaling laws in Rydberg atoms are summarized in Table 3.3 (more details in this regard can be found in Ref. [68]).

Although the study of Rydberg atoms dates back to the early days of atomic physics at the 1890s, harnessing their properties took several decades when the advanced techniques of laser tuning were established in the 1970s. Building upon the advancement in laser technology, gigantic (ultracold) Rydberg atoms can be loaded into *optical lattices* (periodic optical potential generated by interfering laser beams) with a lattice spacing of a few micrometers where optical addressing is possible [2]. Another popular platform instead of the optical lattices is the arrays of *optical tweezers* which are basically tightly-focused dipole traps and are more flexible at large scales [70]. The ultracold Rydberg atoms in lattices or the so-called *frozen Rydberg gases* (first realization dates back to the end of twentieth century [71, 72]) feature ex-

Property	Scaling
Level spacing	$\tilde{n}^{-3}$
Energy levels	$\tilde{n}^{-2}$
Orbital radius	$\tilde{n}^{+2}$
Radiative lifetime	$\tilde{n}^{+3}$
C_3 coefficient	$\tilde{n}^{+4}$
Polarizability	$\tilde{n}^{+7}$
C_6 coefficient	$\tilde{n}^{+11}$

Table 3.3: Scaling laws in Rydberg atoms with effective principal quantum number $\tilde{n}$ [68, 69].

treme prevention of simultaneous excitation of adjacent Rydberg atoms into their Rydberg states, known as *Rydberg blockade*, due to the strong dipole-dipole interaction. This property has been massively exploited in the fields of quantum computation and quantum simulation.

Regarding the experimental preparation of Rydberg atoms, some technical aspects should be mentioned here. First of all, similar to trapped ions, a cloud of alkali atoms are guided through a vacuum chamber and then become laser-cooled and loaded into optical lattices or arrays of optical tweezers, described in more detail in [68, 73]. Now, to prepare Rydberg atoms, ground-state atoms (in s states) get excited to the ionization threshold (ns/nd) which is usually accomplished by *two-photon excitation schemes*. Single-photon excitation is more challenging due to some technical restrictions for the required high-frequency lasers and fundamental limitations corresponding to the selection rules. Instead, atoms are initially excited to an intermediate state (like $5p$) by off-resonant lasers with large detuning; Afterwards, the excitation toward the desired state takes place. Here, the large detuning ensures the effective two-level description of this three-level scheme. Rydberg atoms can be also manipulated using electric and magnetic fields installed in the vacuum chamber. Similar to the trapped ions, the read-out process is also performed by optical pumping where fluorescence imaging shows the number of emitted photons as a measure of the state population.

The conventional frozen Rydberg gas can be described by interacting spin-1/2 particles undergoing excitations from an external laser. Interestingly, the resource Hamiltonian in the rotating frame of the laser excitation resembles the conventional quantum Ising model with long-range interaction,

$$H_{\text{Ryd}} = -\frac{\Delta(t)}{2}\sum_i \sigma_z^{(i)} + \frac{\Omega(t)}{2}\sum_i \sigma_x^{(i)} + C_6 \sum_{i<j} \frac{P_r^{(i)} P_r^{(j)}}{r_{ij}^6}, \tag{3.28}$$

where in which Ω is Rabi frequency, Δ is detuning, C_6 denoted the van der Waals coefficient, and $P_r^{(i)} = (1 + \sigma_z^{(i)})/2$ is the projection onto the Rydberg state. In the Rydberg blockade regime $C_6 \gg \Omega$, Rydberg atoms are shown to be capable of simulating a large variety of many-body phenomena including topological phases, lattice gauge theories, and quantum scars [74, 75, 76]. Moreover, If the atoms in this setup are prepared in two different Rydberg states, then the resulting Hamiltonian became an XY-type with the dipole-dipole interaction, i.e. C_3/r^3 [73]. Also, engineering other types of Hamiltonian such as PXP, XXZ, etc. using Rydberg atoms has been studied both theoretically and experimentally where a good review in that regard is [77]. Other variants of variational treatments using Rydberg atoms have been also proposed as a possible direction to obtain a quantum advantage in the context of optimization problems [78].

Rydberg-atom simulators are currently of the most promising neutral-atom-based platforms which underwent fast developments in recent years. This platform is highly flexible in terms of lattice geometry and dimensionality (contrary to trapped ions) thanks to the optical tweezers. Rydberg atoms are also in a fast race of scalability compared with other platforms as recently setups with several hundreds of qubits have been implemented [79, 80]. Regarding the lifetime of the Rydberg states, the idea of *Rydberg dressing*, i.e. admixing a small fraction of the Rydberg state to the ground state, has been proposed and implemented that can lengthen the lifetime [81, 82]. More technical aspects of challenges in Rydberg atoms with possible solutions are presented in Ref. [77].

Part II

Collective Effects in Steady States

A good theoretical model of a complex system should be like a good caricature: It should emphasize those features which are most important and should downplay the inessential details.

— Michael Ellis Fisher

Chapter 4

Bistability in steady states

4.1 Introduction

Non-equilibrium physics provides many exotic phenomena beyond reach in equilibrium physics. Among them, of predominant importance is the emergence of *multistability*, where multiple phases coexist in stationary distribution, without the restricting Gibbs phase rule in equilibrium systems. However, the characterization of non-equilibrium steady states is challenging due to the absence of a notion of the partition function. The theoretical challenges get intensified in the context of quantum many-body systems due to the exponential growth of Hilbert space with system size. Consequently, many theoretical and experimental studies have been performed to overcome these issues and explore important questions especially regarding asymptotic dynamics of open quantum systems [39, 83, 84, 85, 86, 87, 88, 89]. In particular, while mean-field calculations predict steady-state bistability over an extended parameter range for many different systems [90, 91, 92, 93, 94, 95, 96, 97], more elaborate methods falsify these findings [39, 98, 84, 30, 37, 31]. The failure of the mean-field theory comes from the fact that, in contrast to equilibrium systems, mean-field solutions for open systems do not describe the physics above the upper critical dimension [30, 99]. Consequently, it is still unclear to what extent open quantum systems can exhibit bistability.

To address this question, we present a generic framework to investigate steady-state bistability based on a novel variational treatment of the Lindblad master equation. This provides a quantitative analysis of stability in the long-time limit of generic dissipative dynamics, distinguishing long-lived *metastable states* from truly steady states in the thermodynamic limit of infinite size. In this chapter, we first demonstrate how to evaluate the relaxation rate associated with the steady-state solutions obtained by minimization of a suitable variational norm. We then apply our variational formalism to a dissipative Ising model exhibiting *mean-field bistability* [90, 92]. We will show that the bistability is only observable at the vicinity of a phase transition while away from that the thermodynamically unstable solution decays rapidly.

However, the situation is fundamentally different when it comes to dissipative dynamics undergoing non-thermal fluctuations. Building upon the possibility of recasting the steady state problems in terms of effective free energy functionals [99], we will establish a variational Langevin approach to study these systems. Particularly, we investigate an intriguing probabilistic cellular automaton with a finite range of bistability in its two-dimensional parameter space. We will present a mater-equation embedding of the so-called Toom's voting model in terms of chiral jump operators. Crucially, we observe that bistability persists even in the presence of quantum fluctuation, giving rise to the first demonstration of genuine bistability in an open quantum many-body system.

4.2 Thermally-activated nucleation processes

One important byproduct of the Gutzwiller approach is that the variational function is directly connected to thermal fluctuations in the underlying open-system steady state, as it quantifies deviation of the exact steady state from the variational product ansatz [99]. This in turn comes from the fact that in driven-dissipative systems all correlations near a critical point obey the classical fluctuation-dissipation theorem at low frequencies, hence indicating a scale-independent effective temperature [30, 100]. As a result, we can employ the vast toolbox of classical statistical mechanics to investigate the stationary properties of open quantum many-body systems. Particularly, the statistical theory makes it possible to investigate the process of non-equilibrium relaxation dynamics of metastable states [101]. In this approach, we can quantify the stability of (possibly multiple) variational steady-state solutions via relaxation rate in a *thermally-activated nucleation process*.

To gain a better insight about such processes, let us first review the basic concepts in the classical nucleation theory. Nucleation is basically the mechanism behind a first-order phase transition [102]. We know that a thermodynamically *stable* phase of a physical system lives at the lowest possible point in the landscape of the free energy. However, changing a control parameter such as temperature can destabilize the system by making it stuck in a local minimum. Such a state is not totally *unstable* but rather *metastable*, since any perturbation increases the free energy. However, the system can reach a more stable state if it overcomes an energy barrier. A jump to this global minimum can be initiated by fluctuations in the system parameter, e.g. thermal fluctuations. While the fluctuations create small droplets of the more stable state, due to the *surface tension* they shortly decay in size and eventually disappear. Nevertheless, for certain value of the control parameter, these droplets reach a critical size so that their *bulk energy* overcomes the surface tension facilitating the growth of the droplets. Eventually, the system forms the new equilibrium phase through such a growth and nucleation process.

4.2.1 Arrhenius law for open systems

Thermally-activated processes can be viewed through the *Arrhenius law*,

$$I \propto \exp(-E_a/k_B T), \tag{4.1}$$

which basically gives the rate of a chemical reaction as a function of some *activation energy* E_a and absolute temperature T. The same law can explain the relaxation of metastable states in the underlying nucleation process. A standard formulation of the associated relaxation rate can be extracted from a probability equation describing the time evolution of a generic dissipative system in the presence of thermal fluctuations [101]. The steady-state solution of this equation based on a saddle-point approximation yields the following relaxation rate

$$I = |\kappa| V \left(\frac{k_B T}{2\pi |e_1|}\right)^{1/2} e^{-F_a/k_B T}, \tag{4.2}$$

where F_a denotes the excess free energy of the critical nucleus, V is the volume of the system, κ represents the growth rate of the unstable mode started from the saddle point, and e_1 is the negative eigenvalue of the Hessian matrix of F_a (with respect to the system's momenta) at the saddle point.

In the context of the steady state of an open quantum system, the variational norm f_v resembles the free energy exhibiting two energetically uneven minima, a stable state corresponding to the lower minimum and a metastable state corresponding to the higher minimum. Therefore, the nucleation process in combination with the variational norm can be employed to analyze the stability of the steady states, see Fig. 4.1. Consequently, the *relaxation rate* (per volume) of a metastable state can be assessed by the following relation

$$I = f_v^u \left(\frac{f_v^m}{2\pi\lambda}\right)^{1/2} e^{-\tilde{E}_a/f_v^m}, \tag{4.3}$$

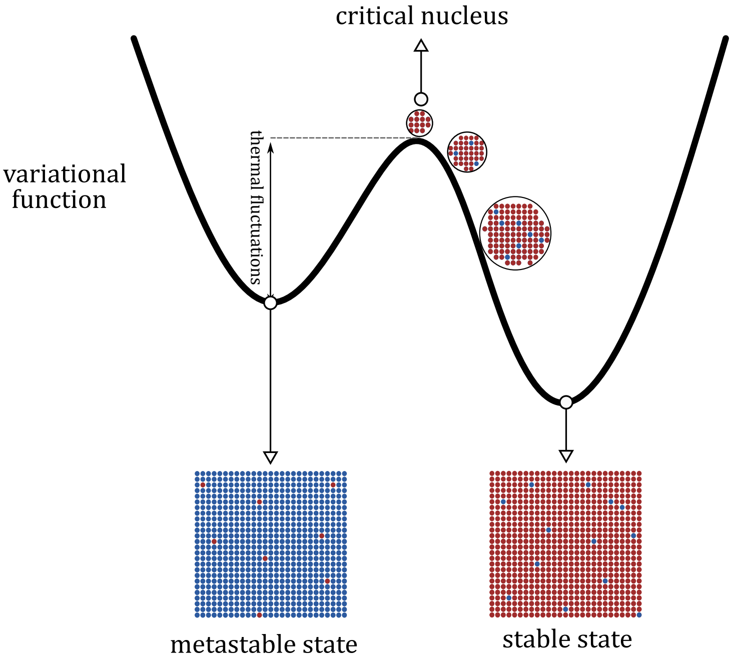

Figure 4.1: Thermally-activated nucleation process in non-equilibrium steady states described by the variational norm.

where f_v^m (f_v^u) is the value of variational norm of the metastable state (unstable state which is a saddle point separating the two minima). Correspondingly, f_v^m serves as *thermal-like fluctuations* $k_B T$ and the activation energy $\tilde{E}_a$ is interpreted here as the variational cost of a critical droplet or nucleus. By considering a square-shaped nucleus with the length ℓ,

$$E_a = -\ell^2(f_v^m - f_v^s) + 4\ell(f_v^u - f_v^m),$$

which respectively consists of *volume energy* of the nucleus and surface tension of its domain wall [21]. $\tilde{E}_a$ is then defined as the maximized activation energy with the *critical length* $\ell^* = 2(f_v^u - f_v^m)/(f_v^m - f_v^s)$. Concerning the surface tension, we consider a localized sharp kink, in the order of the lattice spacing, separating the stable nucleus from the rest. In fact, a smooth kink as in Ref. [21] using a gradient term does not result in any significant change as we have investigated it within our variational method. Finally, $\lambda = 2(f_v^m - f_v^s) > 0$ is defined as the second derivative of E_a with respect to ℓ [101].

4.2.2 Application: Dissipative Ising model

We now start investigating a concrete model using our variational formalism. The paradigmatic Ising model is obviously the first choice as it provides a minimal description of phase transition and has been extensively exploited to study various many-body phenomena. Particularly, we choose a dissipative variant of the transverse-field Ising model shows a first-order liquid-gas transition with a controversial region of bistability in its phase diagram of the non-equilibrium steady state [90, 103, 104, 92, 39, 98, 105, 87]. The coherent part of the dissipative Ising model on a two-dimensional lattice of spin-1/2 particles can be described by the following Hamiltonian

$$\mathcal{H} = \frac{g}{2}\sum_i \sigma_x^{(i)} + \frac{J}{4}\sum_{\langle ij\rangle} \sigma_z^{(i)}\sigma_z^{(j)},$$

where g (J) indicates the strength of a transverse field (inter-particle interaction). Dissipation is incorporated by adding spin flips in the form of quantum jump operators $c_i = \sqrt{\gamma}\sigma_-^{(i)}$ with the rate γ.

Within the variational approach, we can obtain approximated steady-state solution(s) by minimizing the corresponding variational norm f_v in Eq. (3.8). Close to the transition, the variational results exhibit a two-basin structure corresponding to the two possible phases in the long-time limit and the thermodynamic limit of the dissipative Ising model. One of the basins always has a lower value of the variational norm except at the phase transition. Figure 4.2 illustrates the two minima corresponding to the competing phases at the first-order phase transition where a saddle point separates them as a Landau free-energy barrier. This observation already invalidates the mean-field prediction of a finite region of bistability as the two distinct states only appear close to the phase transition.

As a more comprehensive analysis of bistability in the system, we compute the relaxation rate defined in Eq. (4.3) to have a quantitative assessment of the long-time stability of the two phases. As shown in Fig. 4.3, far from the phase transition only one of the phases is dynamically stable (as $\log(I) \to 0$). In other words, the metastable state decays in finite time $1/I$ as nucleation fluctuations can overcome the energy barrier. However, for a narrow width of g/γ, the relaxation rate of the two states radically decreases, and close to the phase transition they vanish supporting the occurrence of a first-order phase transition.

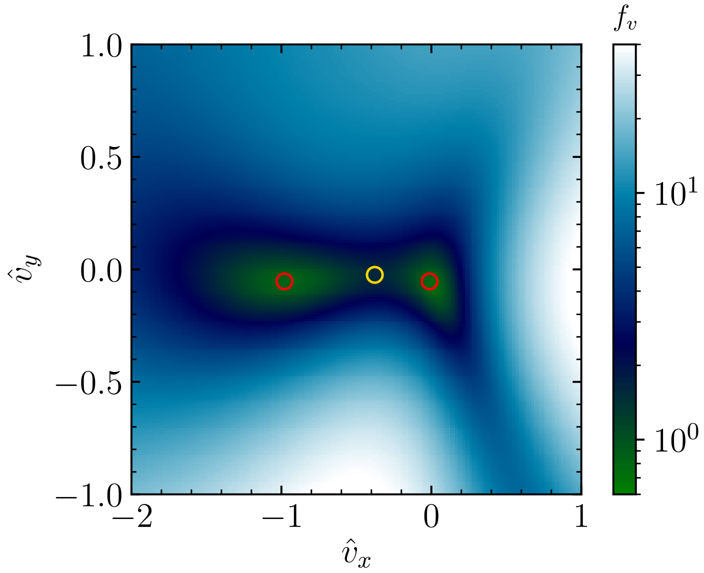

Figure 4.2: (a) Numerical results for the variational function f_v in logarithmic scale regarding the dissipative Ising model at a first-order phase transition ($J/\gamma = 5, g/\gamma \approx 5.35$) in a plane of variational parameters constructed out of two minima (red circles) and an intermediate saddle point (yellow circle). The left minimum corresponds to a gaseous phase of up spins and the right minimum denotes a liquid phase.

These results that are remarkably in good agreement with other numerical calculations [39, 98, 30, 37, 31], unravel the metastability induced by phase transition in the dissipative Ising model. To be explicit, in a real experiment, a magnetic hysteresis in the steady state is expected due to the extremely large values of the relaxation time in the vicinity of the transition. In fact, the hysteresis behaviour is already observed in relevant experiments with Rydberg gases, see e.g. [103].

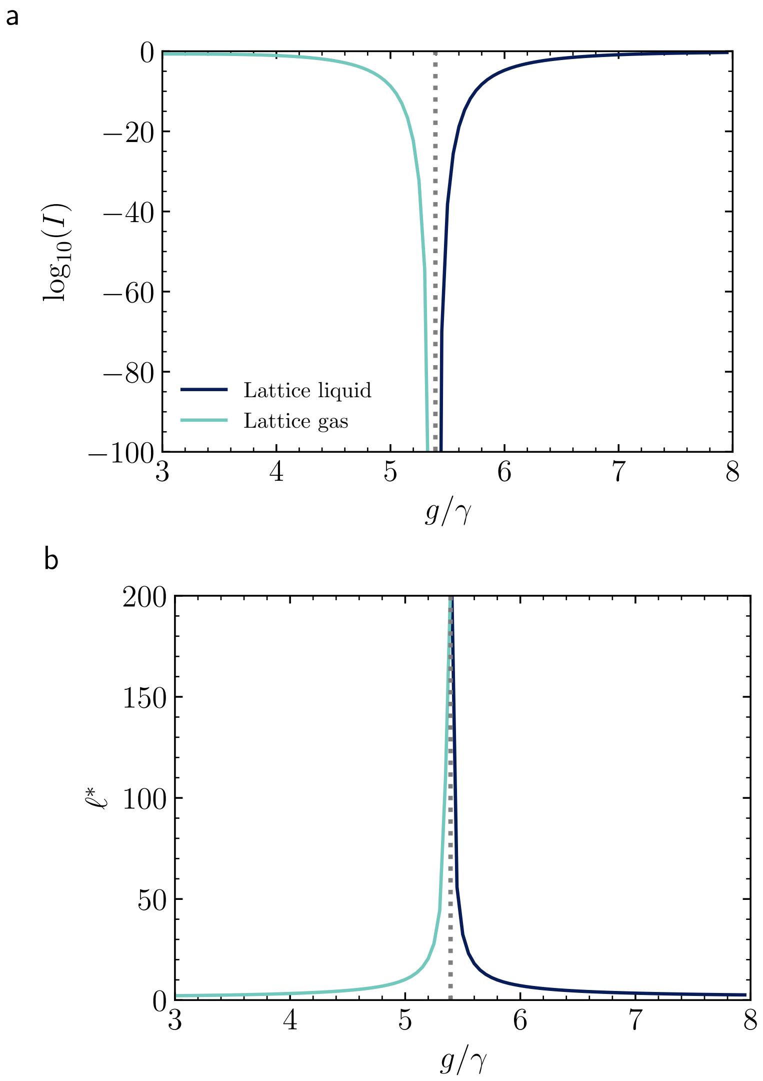

Figure 4.3: (a) The log of relaxation rates $\log_{10}(I)$ and (b) the critical length ℓ^* of the two phases as a function of g/γ demonstrates ergodicity in the steady state except for a small region around the critical point (dotted line with $J/\gamma = 5, g/\gamma \approx 5.35$).

4.3 Non-equilibrium kinetics of nucleation

So far, we have discussed transition-induced bistability in steady states arising from thermally-activated processes. However, a generic multistability requires non-thermal fluctuations to break the uniqueness of the steady state. Crucially, a basic understanding of *non-ergodic behavior* in irreversible quantum dynamics can be built upon the well-studied *probabilistic cellular automata*. Among them, *Toom's majority voting model* has received considerable interest because of its ability in solving the *majority problem*, finding the majority state of a many-body system with local interactions, by suppressing small minorities [106, 107, 108, 109]. This model exhibits an intriguing phase diagram including a finite region of bistability within its 2-dimensional parameter space.

To unfold the non-equilibrium charterer of Toom's model, we will employ the *Langevin formalism* giving access to a mesoscopic description of the dynamics using a time-dependent stochastic differential equation. As mesoscopic Langevin equations underpin the study and analysis of non-equilibrium processes, it is crucial that these equations are typically phenomenological and hard to be verified. Extracting the phenomenological parameters from the corresponding microscopic Liouvillian is generally difficult. To overcome this challenge, we convert the variational function to a Ginzburg-Landau-like functional (discussed in Ref. [99]) which its stationary solution gives rise to an effective Langevin equation.

4.3.1 Toom's majority voting model

Before discussing further, we briefly review the main features of Toom's model. The model basically consists of two-level cells located on a square lattice evolving probabilistically in a discrete time according to a three-site neighborhood majority. We can represent this model as a spin-1/2 system via conditional updates using a set of (eight) collective jump operators acting on a North-Center-East (NCE) neighborhood, i.e.

$$c_j = \left\{\sqrt{\Gamma} P_{0/1}^{(j+N)} \sigma_{-/+}^{(j)} P_{0/1}^{(j+E)}\right\}, \tag{4.4}$$

where $\sigma_-^{(j)} = |0_j\rangle\langle 1_j|$ ($\sigma_+^{(j)} = |1_j\rangle\langle 0_j|$) is the lowering (raising) operator acting on the site j on a periodic square lattice depending on the population of its northern and eastern sties, $k \in \{j+N, j+E\}$, encoded into the projection operator $P_s^{(k)} = |s_k\rangle\langle s_k|$ with $s \in \{0,1\}$. Moreover, lower indices and Γ are then chosen according to the Table 4.3.1. The transition rate $\gamma_\mu = -\ln(\mu)/t_d$

NCE state	101	111	110	011	010	100	001	000
Operation	σ_+	σ_-	σ_-	σ_-	σ_-	σ_+	σ_+	σ_+
rate	γ_ν	$\bar{\gamma}_\nu$	$\bar{\gamma}_\nu$	$\bar{\gamma}_\nu$	γ_μ	$\bar{\gamma}_\mu$	$\bar{\gamma}_\mu$	$\bar{\gamma}_\mu$

Table 4.1: Ruleset and the corresponding transition rates for Toom's model indicating how the central site is updated according to the North-Center-East state.

($\gamma_\nu = -\ln(\nu)/t_d$) denotes the rate of depopulating (populating) the central site, determined by some probability μ (ν) over a duration time t_d, if the neighborhood majority is in the $|0\rangle$ ($|1\rangle$) state. In the same way, $\bar{\gamma}_\mu = -\ln(1-\mu)/t_d$ and $\bar{\gamma}_\nu = -\ln(1-\nu)/t_d$ represent the transition rate in favor of the minority votes.

While the deterministic limit of Toom's model, i.e. $\mu = \nu = 0$ has readily the ability of elimination of minority islands, Toom has rigorously proved that this ability persists even in the presence of small values of μ or ν, which can be thought of as some noise occurring in the implementation of the updating rules [106, 110]. This makes Toom's model a fault-tolerant error correcting model for a finite range of noise. Although Toom's theorem is only relevant to the discrete-time and synchronous updates, it has been shown that the argument also holds for a generalized Markovian process [111].

The Toom's model is usually characterized in a two-parameter space of noise with amplitude $T = \mu + \nu$, analogous to temperature and with bias $H = (\nu - \mu)/(\mu + \nu)$, analogous to the symmetry-breaking magnetic field in the Ising model. In the case of an unbiased noise $H = 0$, the model behaves like the zero-field Ising model with a continuous transition at a critical temperature. However, in the presence of biased noise, the model, in contrast to the Ising model, undergoes a first-order transition between a bistable phase and a unique ergodic phase. This behavior arises from the *chirality* of the jump operators (4.4), as they don't contain the west and south sites [112, 113]. Basically, any chiral updating rule violates the *detailed balance* which is generally a sufficient condition for a dynamical system to reach a unique steady state described by the Boltzmann distribution [109].

4.3.2 Mesoscopic Langevin formalism

To analyze the non-equilibrium behavior of the Toom's model, we construct a Langevin equation based on a field-theoretical treatment of the variational norm. First, we introduce an *order parameter* $\phi = \langle\sigma_z\rangle$ in the Gutzwiller ansatz which undergoes spatial fluctuations as a *classical field*. We can then extract a Ginzburg-Landau-like functional from the homogeneous variational norm f_v in addition to an inhomogeneous term g_v which incorporates the fluctuations, i.e.

$$\mathbb{F}[\phi] = \sum_i f_v(\phi_i) + g_v(\nabla\phi_i). \tag{4.5}$$

The full description of $g_v(\nabla\phi_i)$ is discussed in Appendix B.1.

Derivation of the Langevin equation

let us first derive the time dependency of the classical field. Rewriting a generic density matrix at time t around a small perturbation of the field ϕ,

$$\rho_t = \frac{1}{2}\big[\rho(\phi_t + \epsilon) + \rho(\phi_t - \epsilon)\big]. \tag{4.6}$$

The structure of the Lindblad master equation implies that the variational norm corresponds to a decay rate of the density matrix, or $\rho_{t+\tau} = e^{\hat{\mathcal{L}}\tau}\rho_t \equiv e^{-f_v\tau}\rho_t$. Therefore,

$$\rho_{t+\tau} = \frac{e^{-f_v(\phi_t+\epsilon)\tau}\rho(\phi_t + \epsilon) + e^{-f_v(\phi_t-\epsilon)\tau}\rho(\phi_t - \epsilon)}{e^{-f_v(\phi_t+\epsilon)\tau} + e^{-f_v(\phi_t-\epsilon)\tau}}.$$

After multiplying both sides of the equation by σ_z and taking the trace one obtains

$$\phi_{t+\tau} = \frac{e^{-f_v(\phi_t+\epsilon)\tau}(\phi_t + \epsilon) + e^{-f_v(\phi_t-\epsilon)\tau}(\phi_t - \epsilon)}{e^{-f_v(\phi_t+\epsilon)\tau} + e^{-f_v(\phi_t-\epsilon)\tau}}.$$

Now performing a Taylor expansion around ϕ up to the second order yields

$$\frac{\partial}{\partial t}\phi = -\epsilon^2\frac{df_v}{d\phi}. \tag{4.7}$$

Interestingly, this equation resembles the deterministic part of the Langevin equation corresponding to the so-called relaxational model A describing the dynamics of a non-conserved field [114],

$$\frac{\partial}{\partial t}\phi_i = -\frac{d\mathbb{F}}{d\phi}|_{\phi=\phi_i} + \xi_i, \tag{4.8}$$

The stochastic part of the Langevin equation is governed by a white Gaussian noise $\langle\xi_i\rangle = 0$, whose correlation function incorporates an effective temperature, i.e. $\langle\xi_i(t)\xi_j(0)\rangle = T_{\text{eff}}\delta_{i,j}\delta(t)$. In our case, the effective temperature can be estimated by the value of the variational norm at the less-stable state (value of the higher minimum in the two-basin variational landscape),

$T_{\text{eff}} \equiv f_v^m(\phi_i)$. Finally, the Langevin equation of Toom's model takes the following form

$$\frac{\partial}{\partial t}\phi_i = -\Big[\frac{\partial f_v}{\partial \phi_i} - a - (b - b')\nabla\phi_i - 2b'\phi_i - c\nabla^2\phi_i\Big] + \xi_i, \tag{4.9}$$

where the gradient terms indicate discrete lattice differences and are defined as follows

$$\begin{aligned} \nabla\phi_i &= \phi_{i+N} + \phi_{i+E} - 2\phi_i \\ \nabla^2\phi_i &= \phi_{i+N} + \phi_{i+S} + \phi_{i+W} + \phi_{i+E} - 4\phi_i. \end{aligned} \tag{4.10}$$

The equation (4.9) differs from that of the conventional Ising model due to the appearance of a linear gradient term with coefficient $(b - b') > 0$ which captures the chirality of the jump operators. In fact, a sufficiently large $(b-b')$ ensures the shrinkage of minority islands of either state. It is also important to mention that in Eq. (4.9), we have expanded g_v up to the second-order term around $\phi = 0$ which makes the equation only valid close to criticality.

Phase diagram of Toom's model

We have estimated the phase diagram of Toom's model in $T - H$ plane by solving the Langevin equation for a 20×20 lattice and averaging over 100 samples initialized in a majority of the less-stable state (See Appendix B.2). Figure 4.4 shows a finite region of bistability which has no counterpart in the corresponding equilibrium system. It is worth mentioning that due to the *asynchronicity* of quantum jumps in contrast to Toom's original updating rules, the phase diagram quantitatively differs from that of the original model [107].

According to the numerical simulation close to criticality, two first-order lines separate the bistable region from the ergodic one ending up to an Ising-type critical point of continuous transition which takes place at $T_c = 0.777 \pm 0.001$ on the line of $H = 0$ as it is shown in the inset of Fig. 4.4. In the case of finite bias, we extrapolated the first-order lines described by a power-law equation $|H| \propto (T_c - T)^\beta$ with the exponent $\beta = 1.280 \pm 0.008$ which differs slightly from its mean-field value of $3/2$. The latter can be obtained from the uniform solution of the Langevin equation [112].

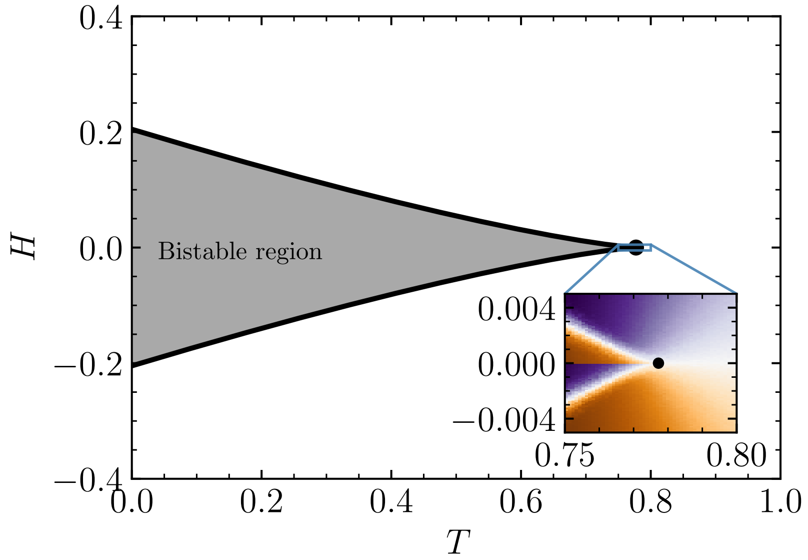

Figure 4.4: Phase diagram of Toom's model showing two first-order lines of phase transition (black lines) from a bistable (gray) region to an ergodic (white) phase meeting at a critical point $T_c = 0.777 \pm 0.001$ (black dot) where the Ising continuous transition takes place. The inset shows how the orientation of stationary magnetization (starting from a majority of the less-stable state) changes in different zones close to criticality.

We also investigate the non-ergodic behavior of the classical Toom's model in the presence of *quantum fluctuations*. To this end, we incorporate the so-called PXP Hamiltonian in the form of

$$\begin{aligned}\mathcal{H}_{\mathrm{PXP}} = \Omega \sum_{ij} \big[& P_0^{(j+N)} \sigma_x^{(j)} P_0^{(j+E)} \\ & + P_1^{(j+N)} \sigma_x^{(j)} P_1^{(j+E)} \big],\end{aligned}$$

to the original Toom's Liouvillian. The projection operators are chosen such that quantum fluctuations appear when the neighborhood's votes are identical. Thus, the Hamiltonian also acts against a local majority as a new source of noise in addition to the classical noise. Moreover, since the PXP Hamiltonian is invariant under conjugation by σ_x, it only couples $\langle \sigma_y \rangle$ and $\langle \sigma_z \rangle$ while keeping $\langle \sigma_x \rangle$ intact. This in turn allows us to generalize the definition of the classical field to z; Here, $\theta = \arctan(\alpha_y/\alpha_z)$ denotes a proper rotation around x-axis such that it converts $\rho(\alpha_y, \alpha_z)$ to a single variable density matrix $\rho(\phi)$. The orthogonal field $\phi_\perp$ is then a gapped one whose functional contains only a quadratic term excluding any criticality. This means that even in the presence of quantum fluctuations, the Langevin equation is still able to describe the model by an effective classical field.

To estimate the phase diagram we first calculate the homogeneous variational norm f_v in terms of α_y and α_z giving access to the rotational angle of the field as well as the effective temperature which is required for the white noise in the Langevin equation. Figures 4.5(a,b) respectively exhibit the variational landscape deep in the bistable phase and the ergodic phase. Having the variational field-theoretical approach tuned to study the effect of quantum fluctuations in the long-time limit of the model, we have computed the phase diagram at $T = 0.75$ (close to the critical point) as a function of Ω and H, shown in Fig. 4.6. First of all, it is noticeable that Toom's bistability persists even in the presence of quantum fluctuations. Basically, in the bistable region, Fig. 4.5(a), relatively small thermal-like noise does not destroy the Toom-like behavior leading to two thermodynamically stable solutions. However, by increasing Ω, Fig. 4.5(a), the valley in the variational landscape shallows hence facilitating nucleation of the more stable state. Furthermore, the long-time limit of bistability meets the thermodynamic limit of phase transition where the relatively strong quantum fluctuations become dominant showing a similar critical point as that of the classical case.

This procedure exemplifies the application of classical cellular automata to engineer exotic multiple steady states in the context of quantum many-body systems. In a broader picture, cellular automata can be considered as the parent models to design non-ergodic open quantum systems. For instance, while Ref. [115] asserts that $D = 2$ is the lower critical dimension for bistability in typical spin systems, intricate cellular automata such as in Ref. [116] demonstrate non-ergodicity even in one dimension which can be possibly used to devise the same feature in 1D quantum systems. Moreover, the physical realization of correlated jump operators required for the updating rules of such systems is feasible using (for example) ultracold Rydberg atoms trapped in optical lattice, see Appendix C. Particularly, a recent proposal on quantum cellular automata [117] has fully addressed this problem suggesting a scheme for designing unitary and non-unitary interactions based on multi-frequency (de-)excitation of Rydberg states.

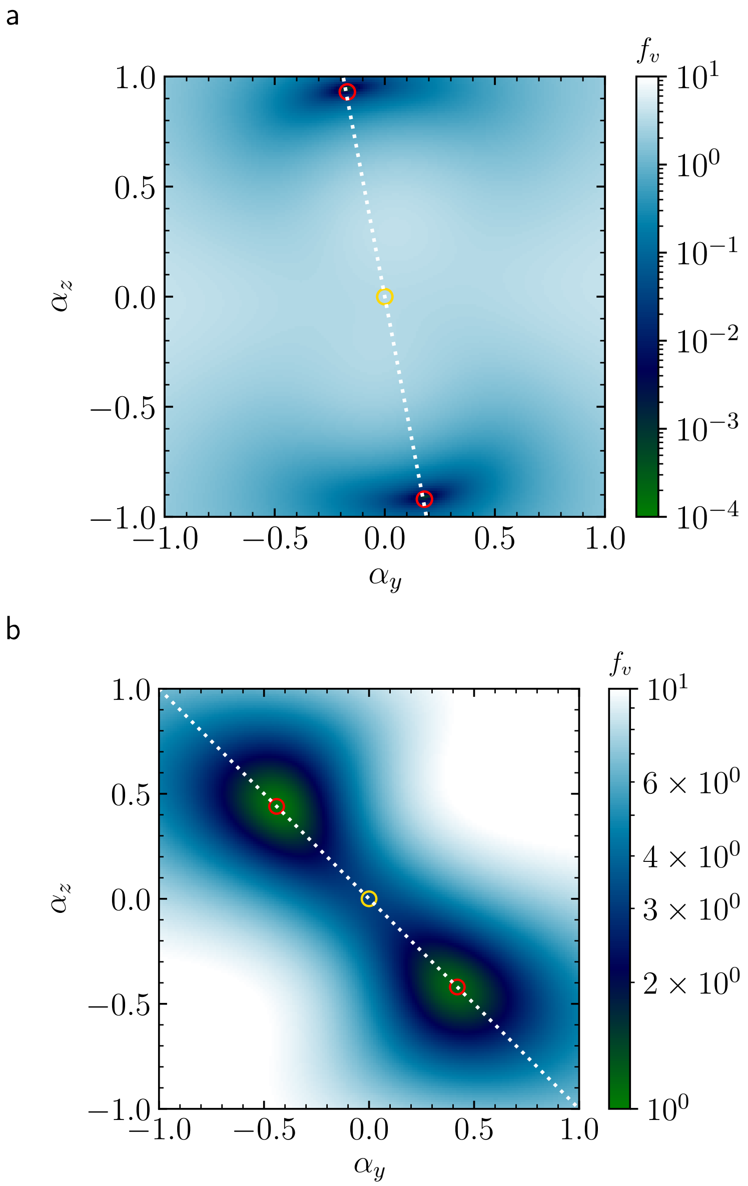

Figure 4.5: Bistability in the variational steady state of Toom's model in the presence of quantum fluctuation. Variational norm (in logarithmic scale) is depicted as a function of α_z and α_y for $H = T = 0.15$ deep in (a) the bistable phase with $\Omega t_d = 0.15$ and (b) the ergodic phase with $\Omega t_d = 2.0$. The dotted lines show the axis of the effective classical field.

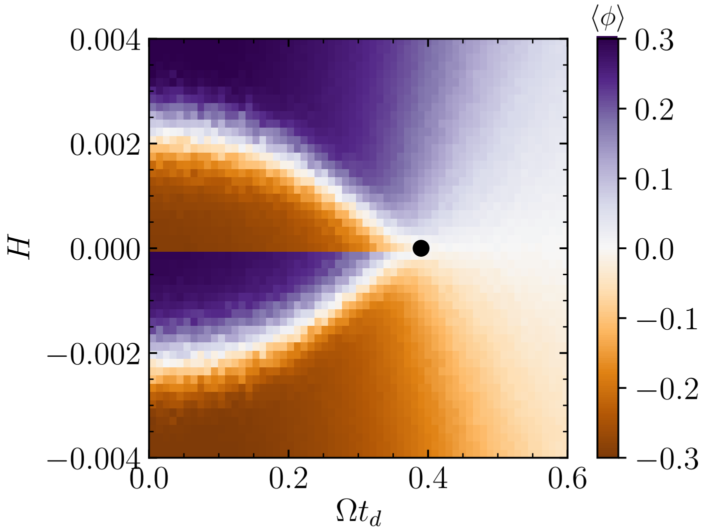

Figure 4.6: Phase diagram of Toom's model in the presence of quantum fluctuations at $T = 0.75$ showing gradual shrinkage of the bistable region by increasing Ω ending up with a critical point (black square) at $\Omega_c t_d = 0.39 \pm 0.02$ similar to the classical case.

To summarize, we have developed a method for assessing bistability in the steady state of open many-body systems with Markovian evolution. Our proposal relies on the notion of the nucleation process among multiple minima appearing in a variational subspace of the fixed states of Linbladians. We note that our method applies to a wide range of dissipative many-body systems to verify any predicted multistability. In particular, we have demonstrated how the controversial bistability in the dissipative Ising model emerges only in proximity to a phase transition refuting any genuine bistability. Moreover, we have investigated a probabilistic cellular automaton featuring genuine bistability in the presence of both classical and quantum fluctuations. Therefore, we conclude that our variational Gutzwiller theory provides a powerful framework to analyze stability in the steady state of dissipative quantum many-body systems.

Chapter 5

Stationary long-range correlation

In chapter 3, we briefly introduced the exaggerated properties of large Rydberg atoms (atoms with an outer electron promoted to states close to ionization threshold in comparison to ordinary ground-state atoms) summarized in Table 3.3. These properties scale with an *effective quantum principal number* $\tilde{n} \equiv n - \delta_l$ where δ_l denotes a modification term called *quantum defect* as a function of the angular momentum number l. This is because Rydberg atoms can be basically described as hydrogen-like atoms using quantum defect theory where the atom's core includes low-lying electrons in addition to the hydrogen nucleus.

Ultracold Rydberg atoms attributed with these properties are especially desirable for quantum simulation. In this chapter, we elaborate on the preparation of stationary long-range correlation in a dissipative variant of Rydberg atoms. We first review the collective effects of Rydberg atoms specifically in the presence of strong long-range interactions. Next, we will study the interplay between these effects and different dissipation channels. Notably, we will be able to obtain a steady-state phase diagram where the long-range correlation plays a major role.

5.1 Strong Rydberg-Rydberg interaction

Rydberg atoms are billion times larger than atoms in their electronic ground state. The excited valence electron in a Rydberg atom can travel microns away from the atomic nucleus which is typically femtometers in size. Equipped with such an extended orbital radius, a long range of nearby atoms are in access to a Rydberg atom. This leads to a powerful dipole-dipole interaction when the electron of a nearby atom is also in a Rydberg state. The so-called *Rydberg-Rydberg interaction* is orders of magnitude stronger than that between ordinary atoms. Furthermore, the Rydberg interaction potential is considerably tunable ranging from *dipole* to *van der Waals* (vdW) and attractive to repulsive. Numerical calculation of the potential is possible by efficient diagonalization of the corresponding Hamiltonian matrix for which also an open-source software is available [118].

5.1.1 Van der Waals interaction

The powerful Rydberg-Rydberg interaction is worth further investigation, specifically at its extreme where it exhibits strong vdW character. To gain more insight, we begin with two Rydberg atoms separated by the internuclear distance vector **R**. The interaction potential between these two atoms consisting of the cores labeled as A and B, and the respective Rydberg electrons numbered as 1 and 2 has the following form

$$\begin{aligned} V_{\mathrm{int}} &= \left(\frac{1}{|\mathbf{R}|} + \frac{1}{|\mathbf{r}_{12}|} - \frac{1}{|\mathbf{r}_{1B}|} - \frac{1}{|\mathbf{r}_{2A}|} \right) \\ &= \left(\frac{1}{|\mathbf{R}|} + \frac{1}{|\mathbf{R} - (\mathbf{r}_{1A} - \mathbf{r}_{2B})|} - \frac{1}{|\mathbf{R} - \mathbf{r}_{1A}|} - \frac{1}{|\mathbf{R} + \mathbf{r}_{2B}|} \right), \end{aligned} \tag{5.1}$$

where the negative (positive) terms indicate electrostatic attraction (repulsion). Now, if the electronic wavefunctions (Rydberg orbits) of the two atoms are not overlapping, i.e. $R > r_{1A} + r_{2B}$, one can perform a multidimensional Taylor expansion in R which (in leading order) yields the dipole-dipole interaction potential [119]

$$\begin{aligned} V_{\mathrm{dd}} &= \frac{\boldsymbol{\mu}_{1A} \cdot \boldsymbol{\mu}_{2B} - 3(\boldsymbol{\mu}_{1A} \cdot \mathbf{n})(\boldsymbol{\mu}_{2B} \cdot \mathbf{n})}{R^3} \\ &= \left(1 - 3\cos^2\theta\right) \frac{C_3}{R^3}, \end{aligned} \tag{5.2}$$

where $\boldsymbol{\mu}_i = -e\boldsymbol{r}_i$ denotes the dipole moment operator, $\boldsymbol{n} = \boldsymbol{R}/R$ represents the interatomic axis, and $C_3 = \mu_{1A}\mu_{2B}$ is known as *dipole-dipole interaction coefficient* which scales as $\tilde{n}^{+4}$.

Let's now suppose that the atoms are in the state $|\psi\rangle \equiv |r_1, r_2\rangle$ where r stands for the four quantum numbers. The state $|\psi\rangle$ can be then coupled to another state $|\psi'\rangle \equiv |r_1', r_2'\rangle$ via the dipole-dipole potential V_{dd} represented in the following interaction Hamiltonian (in the basis of $\{|\psi\rangle, |\psi'\rangle\}$)

$$H = \begin{pmatrix} 0 & V_{\mathrm{dd}} \\ V_{\mathrm{dd}} & \delta \end{pmatrix}, \tag{5.3}$$

where $\delta \equiv E(|\psi'\rangle) - E(|\psi\rangle)$ denotes energy difference between the two states being known as *energy defect*. The eigenenergies of the interaction Hamiltonian being

$$E(R) = \frac{\delta \pm \sqrt{\delta^2 + 4V^2(R)}}{2}, \tag{5.4}$$

discriminate two different regimes depending on the ratio of V_{dd}/δ. In the case of short distances, we have $V_{\mathrm{dd}} \gg \delta$ which results in an energy shift in the form of C_3/R^3. However, at long distances compared with the critical distance, i.e.

$$R_c \equiv \left(\frac{C_3}{\delta}\right)^{1/3}, \tag{5.5}$$

where $V_{\mathrm{dd}} \ll \delta$, the interaction turns into the vdW character C_6/R^6 with

$$C_6 \equiv \frac{C_3^2}{\delta}, \tag{5.6}$$

known as *van-der-Waals coefficient.* which can be tuned by changing δ. Considering the fact that $\delta \propto \tilde{n}^{-3}$ for neighbouring state, C_6 varies as dramatically as $\propto \tilde{n}^{11}$. That's why the vdW interaction is extremely strong reaching tens of megahertz for interatomic distances of several micrometers. Moreover, the vdW interaction can also be repulsive, since for certain combination of states δ is negative.

5.1.2 Rydberg blockade effect

The strong vdW interaction in Rydberg atoms has dramatic effects among which the suppression of simultaneous excitation of two nearby atoms to the Rydberg state has attracted specific attention. The so-called *Rydberg blockade* between two individual atoms was initially observed in 2009 ([120, 121]), and has been exploited to generate entangled states (reviewed in [73]).

Let's consider the simple case of two Rydberg atoms being shined by a resonant laser field (with a Rabi frequency Ω) so that the ground state $|g\rangle$ of each atom is coherently coupled to a Rydberg state $|r\rangle$. As a result, the corresponding Hamiltonian can be represented in the following form

$$H = \frac{\Omega}{2}\left(|r\rangle\langle g| \otimes \mathrm{I} + \mathrm{I} \otimes |r\rangle\langle g| + \mathrm{H.c.}\right) + \frac{|C_6|}{R^6}|rr\rangle\langle rr|. \tag{5.7}$$

Within the *blockade regime* where $|C_6|/R^6 \gg \Omega$, the doubly excited state $|rr\rangle$ goes out of reach as its energy shoots up by the quantity $|C_6|/R^6$ (see Fig. 5.1). In other words, starting from the doubly ground state $|gg\rangle$, the field drives

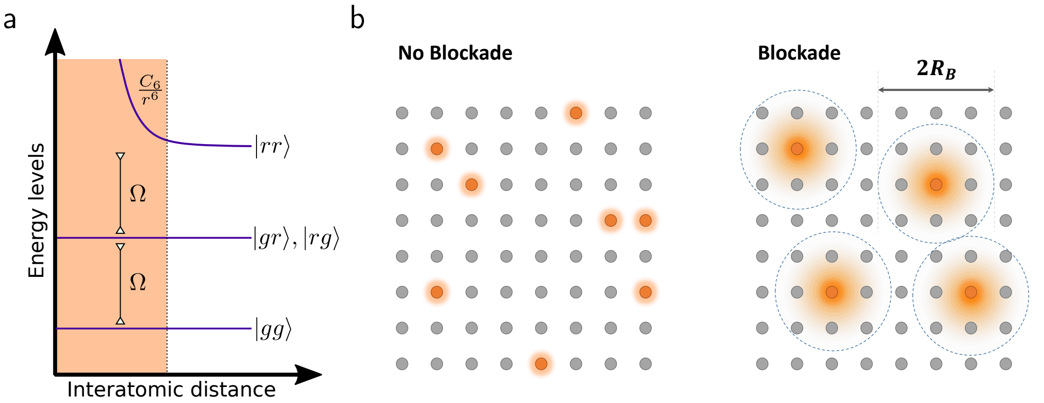

Figure 5.1: (a) Energy levels of two driven atoms with a laser coupling of Ω between an electronic ground state and a Rydberg state. The associated van der Waals interactions make double-excited state $|rr\rangle$ out of resonance. (b) Blockade effect in a 2-dimensional array of Rydberg atoms where the gray (orange) dots represent atoms in the ground (Rydberg) state. The range of the effect is quantified by the Rydberg blockade radius R_B.

the system to reach to the individually excited state $|+\rangle = (|gr\rangle + |rg\rangle)/\sqrt{2}$ with a coupling $\sqrt{2}\Omega$. The excitation requires no energetic cost in terms of the interaction term. However, this is not anymore the case for transition from $|+\rangle$ to $|rr\rangle$. Here, the interaction strongly prohibited the transition hence decoupling the doubly excited state from the dynamics.

This mechanism can be extended to an ensemble of Rydberg atoms leading to a many-body blockade effect within a volume with the *blockade radius* R_b being defined as

$$R_b = \left(\frac{|C_6|}{\Omega}\right)^{1/6}. \tag{5.8}$$

Having a system size larger than R_b gives rise to excitation of multiple Rydberg atoms resulting in a complex many-body dynamics enriched by various entanglement patterns.

5.2 Driven-Dissipative Rydberg gases

The interaction between a quantum system and its surrounding environment induces decoherence and degrades quantum correlations. As a result, the underlying dissipative system becomes effectively classical. However, an external coherent drive is a game-changer especially when it comes to weakly dissipative systems. Notably, this enables quantum correlations to survive through dissipative dynamics giving rise to stationary entangled states. Moreover, such states in contrast to their counterparts in thermal equilibrium possess non-equilibrium features putting them under the spotlight for extensive studies.

Ultracold Rydberg atoms loaded into optical lattices are an ideal platform to study strong correlations and/or interactions in the presence of controllable dissipation. To this end, the Rydberg atoms can be addressed individually and collectively using laser fields. In particular, the so-called *driven-dissipative Rydberg gases* give access to the experimental realization of open many-body systems with highly-correlated non-equilibrium steady states. The rest of this chapter is therefore dedicated to studying the stationary properties of this model using our suggested variational technique in Chapter 3.

To have a suitable microscopic description, we here employ the spin 1/2 representation. In other words, we express the effective two-level states of driven-dissipative Rydberg gases simply in terms of spin down and spin up corresponding to an electronic ground state $|\downarrow\rangle \equiv |g\rangle$, and a highly excited Rydberg state $|\uparrow\rangle \equiv |r\rangle$ respectively. In this representation, the conventional frozen Rydberg gases driven by a coherent laser with Rabi frequency Ω (via two-photon scheme) and frequency detuning Δ can be described by the following Hamiltonian (in the rotating wave approximation)

$$H_{\mathrm{Ryd}} = -\frac{\Delta}{2}\sum_i \sigma_z^{(i)} + \frac{\Omega}{2}\sum_i \sigma_x^{(i)} + C_6 \sum_{i<j} \frac{P_r^{(i)} P_r^{(j)}}{r_{ij}^6}, \tag{5.9}$$

where $P_r^{(i)} \equiv |r_i\rangle\langle r_i|$ denotes a projection of the site i onto the Rydberg state. Here, we assume that the Rydberg states are identical such that the two-body interactions become vdW repulsion. Concerning the experimental setup, we consider a square optical lattice trapping Rubidium-87 atoms with a lattice spacing of $a = 0.532\mu\mathrm{m}$ at a temperature in the order of a few microKelvin. We also consider a strong repulsive interaction by setting $|C_6| = 20\mathrm{MHz}\mu\mathrm{m}^6$ which in turn can be obtained by an appropriate choice of states like $|\downarrow\rangle = |5\mathrm{S}_{1/2}\rangle$ and $|\uparrow\rangle = |31\mathrm{P}_{3/2}\rangle$. The discussions henceforth will be concentrated on the implementation of the numerical method while a detailed description of the experimental platform can be found in Ref. [69] and references therein.

Regarding dissipation in Rydberg gases, we consider local dissipators associated with the population decay of Rydberg states and an effective single-site dephasing where the former corresponds to the amplitude damping channel and the latter correspond to the phase damping channel quantified by the dissipation rates γ_a and γ_p respectively. The dephasing we consider here effectively describes different experimental sources of noise such as atomic motions, finite laser linewidth due to spatial fluctuations of the driving field, and the decay of the intermediate state in the two-photon excitation scheme [122].

In typical experiments, the dissipation rates are relatively small compared to the frequency difference between electronic states. Consequently, the Markovian quantum master equation in the Lindblad form suits describing the time evolution of driven-dissipative Rydberg gases. In this form, the quantum jumps

$$\begin{aligned} c_a^{(i)} &\equiv \sqrt{\gamma_a}|g_i\rangle\langle r_i| = \sqrt{\gamma_a}\sigma_-^{(i)}, \\ c_p^{(i)} &\equiv \sqrt{\gamma_p}\left(|r_i\rangle\langle r_i| - |g_i\rangle\langle g_i|\right) = \sqrt{\gamma_p}\sigma_z^{(i)}, \end{aligned} \tag{5.10}$$

represent single-site decay and dephasing processes. Formulation of the Lindblad master equation vividly exhibits a competition between the driving-induced coherent dynamics and the preceding dissipative processes which possibly gives rise to steady-state phase transition [98]. Also, the master-equation description has another advantage as it gives direct access to the steady state of the dynamics, i.e. the null eigenvector of the Liouvillian. This hugely decreases the cost of numerical simulation which is especially exploited in our variational treatment.

5.3 Implementation of the variational technique

In Section 3.2.2, we introduced an operational variational principle for the steady states of strongly interacting driven-dissipative quantum systems. The resulting variational norm captures non-trivial contributions of correlation in the Lindblad master equation which goes beyond mean-field treatments (see Ref. [39]). It also outperforms the typical semi-classical methods using rate equations which have been extensively used in the context of driven-dissipative Rydberg gases [123, 87]. In the following, we will fine-tune the method for the preceding Rydberg model using a density-matrix ansatz including two-body long-range correlations.

5.3.1 Variational correlation functions

The interaction-induced blockade effect manifests itself in the two-body correlation among Rydberg states qualified by the well-known *pair correlation function* or a g_2 function which reads

$$g_2(r) = \frac{\sum_{i\neq j} g_2(i,j)\delta(r_{ij}-r)}{\sum_{i\neq j}\delta(r_{ij}-r)}, \tag{5.11}$$

with

$$g_2(i,j) = \frac{\langle P_r^{(i)}P_r^{(j)}\rangle}{\langle P_r^{(i)}\rangle\langle P_r^{(j)}\rangle}. \tag{5.12}$$

The g_2 function vanishes within the blockade volume where no simultaneous Rydberg excitation can take place, i.e. $\langle P_r^{(i)}P_r^{(j)}\rangle = 0$ if $r_{ij} < R_b$. On the other hand, for long enough distances the (Rydberg density-density) correlation vanishes, i.e. $\langle P_r^{(i)}P_r^{(j)}\rangle - \langle P_r^{(i)}\rangle\langle P_r^{(j)}\rangle = 0$, and $g_2 = 1$. Due to the strong vdW interaction, this function exhibits a sharp blockaded-uncorrelated transition which roughly resembles a step function [68]. Instead, we here suggest an analytical g_2 function where the step-like behavior is replaced by a quadratic transition. Our ansatz for the g_2 function is

$$g_2(r) \approx \frac{\tilde{r}^6}{\tilde{r}^6 + \alpha_{zz}^{(1)} + \alpha_{zz}^{(2)}\tilde{r} + \alpha_{zz}^{(3)}\tilde{r}^2}, \tag{5.13}$$

where $\tilde{r} \equiv \alpha_{zz}^{(4)} r$ in which α's are the corresponding variational parameters. This function scales as r^6 for $r \ll r_b$ and goes to 1 for $r \gg r_b$. Using this simple analytical function we can estimate the long-range correlations in driven-dissipative Rydberg gases while keeping the number of variational parameters as low as possible. In particular, tweaking the parameter $\alpha_{zz}^{(4)}$ generates different values for the blockade radius and the remaining parameters shape the transition form.

Now, one can easily express the zz correlation function, i.e. $\zeta_{ij}(z,z) \equiv \langle\sigma_z^{(i)}\sigma_z^{(j)}\rangle - \langle\sigma_z^{(i)}\rangle\langle\sigma_z^{(j)}\rangle$, by expanding the definition of $g_2(r_{ij})$ in terms of σ_z. Crucially, we exploit the translation invariance of the state as in our case $\alpha_z = \langle\sigma_z^{(i)}\rangle \simeq \langle\sigma_z^{(j)}\rangle$. As a result, our variational ansatz for zz correlation function is given by

$$\zeta_{ij}(z,z) = [g_2(r_{ij}) - 1](\alpha_z + 1)^2. \tag{5.14}$$

Using Heisenberg equations of motion (see Eq. (3.18)) we can further decrease the number of variational parameters. Especially, in the case of our

correlation function	variational parameters	variational ansatz
$\zeta_{ij}(x,x)$	$\alpha_{xx}^{(1)}, \alpha_{xx}^{(1)}$	$\alpha_{xx}^{(1)} \exp[-\alpha_{xx}^{(2)} r_{ij}]/r_{ij}^2$
$\zeta_{ij}(y,y)$	$\alpha_{yy}^{(1)}, \alpha_{yy}^{(1)}$	$\alpha_{yy}^{(1)} \exp[-\alpha_{yy}^{(2)} r_{ij}]/r_{ij}^2$
$\zeta_{ij}(z,z)$	$\alpha_z,\alpha_{zz}^{(1)}, \alpha_{zz}^{(2)}, \alpha_{zz}^{(3)}, \alpha_{zz}^{(4)}$	$[g_2(r)-1](\alpha_z+1)^2$
$\zeta_{ij}(x,y)$	$\alpha_{xy}^{(1)}, \alpha_{xy}^{(1)}$	$\alpha_{xy}^{(1)} \exp[-\alpha_{xy}^{(2)} r_{ij}]/r_{ij}^2$
$\zeta_{ij}(x,z)$	$\alpha_{xz}^{(1)}, \alpha_{xz}^{(1)}$	$\alpha_{xz}^{(1)} \exp[-\alpha_{xz}^{(2)} r_{ij}]/r_{ij}^2$
$\zeta_{ij}(y,z)$	$\alpha_z,\alpha_{zz}^{(1)}, \alpha_{zz}^{(2)}, \alpha_{zz}^{(3)}, \alpha_{zz}^{(4)}$	$(\gamma_a+\gamma_p)[g_2(r)-1](\alpha_z+1)^2/\Omega$

Table 5.1: Varitional ansätze for two-body correlation functions in two-dimensional driven-dissipative Rydberg gases.

model one can find closed relations between some variational parameters by solving the corresponding Heisenberg equations for the steady state solution,

$$\begin{aligned}
&\frac{d}{dt}\langle\sigma_z^{(i)}\rangle = 0 \to \alpha_y = \frac{\gamma_a}{\Omega}(\alpha_z+1),\\
&\frac{d}{dt}\langle\sigma_z^{(i)}\sigma_z^{(j)}\rangle = 0 \to \zeta_{ij}(y,z) = \frac{\gamma_a+\gamma_p}{\Omega}\zeta_{ij}(z,z),\\
&\frac{d}{dt}\langle\sigma_x^{(i)}\rangle = 0 \to \alpha_x = \frac{\gamma_a(\alpha_z+1)}{\Omega(\gamma_a+4\gamma_p)}\left[2\Delta - C_6(\alpha_z+1)\sum_{j\neq i}\frac{g_2(r_{ij})}{r_{ij}^6}\right],
\end{aligned} \tag{5.15}$$

Since we ultimately look for a steady state phase transition in the underlying two-dimensional lattice, we construct our ansatz in a way that the remaining two-body correlation functions resemble Ornstein-Zernike's exponential form which is used for transition points [124]. In Table 5.1 all the aforementioned ansätze are presented. Therefore, in total we have formulated the variational many-body state in terms of 13 parameters neglecting all the higher-order correlations.

It is worth mentioning that our variational ansatz is mostly expanded around the diagonal elements of the density matrix. This is because all the variational correlation functions are exponentially decaying with the distance except the zz and yz correlation functions that only contribute to diagonal and semi-diagonal elements respectively (see Table 5.1). This is consistent with the reported Monte-Carlo simulation of the model's dynamics showing that the dissipative processes destroy quantum correlation while augmenting classical correlation [122]. As a result, the long-time limit of the total density matrix is nearly diagonal.

5.3.2 Minimization constraints

Having the variational steady state configured, we have to choose a proper minimization method to be able to find the optimal solution for the associated steady state. In this specific model, since the variational landscape is not extremely nasty, we make use of a fast-converging local non-linear optimization method based on the gradient-descent scheme. In particular, we use SLSQP Optimization subroutine of SciPy library in Python [125]. The implemented SLSQP method supports constrained optimization which is necessary for the variational method as it will shortly discussed. However, for a larger number of variational parameters or in the cases where the required initial guess for the parameters is not well-estimated, one can exploit global non-linear optimization methods using open-source packages such as NLopt [126]. Since the computational time in global optimization is usually very long, combined global-local optimization schemes are highly recommended.

We also should mention that the minimization of the variational norm is constrained by two inequalities. The first inequality ensures the positivity of the quantum state. In addition, we impose a second inequality constraint that is exclusively for the Rydberg model. Explicitly, these inequalities are given by

1. Positivity of the density matrix ρ: As the variational norm consists of bipartite reduced density matrices, we only have positivity constraints on all these matrices

   $$\langle\!\langle \rho_{ij} | \Psi \rangle\!\rangle \geqslant 0 \quad \text{for any } \; |\Psi\rangle,$$

   that $\rho_{ij} = \mathrm{Tr}_{\cancel{ij}}[\rho]$. From numerical point of view, this constraint is equivalent to the positivity of the smallest eigenvalue of ρ_{ij},

   $$\mathrm{E}_1[\rho_{ij}] \geqslant 0 \quad \text{for all } \; \rho_{ij}.$$

2. Normalization condition: In equilibrium, normalization condition of the pair correlation function $g_2(\mathbf{r})$ leads to $\int d\mathbf{r}[1 - g_2(\mathbf{r})] = \langle P_r \rangle^{-1}$ [127]. In the non-equilibrium case, this equality condition turns into

the following inequality constraint

$$\sum_{i \neq j} r_{ij}[1 - g_2(\mathbf{r})] \leqslant \frac{1}{\langle P_r \rangle}.$$

5.4 Liquid-gas phase transition

Driven Rydberg gases in the absence of any dissipation are a manifestation of quantum criticality originating from a competition between the strong vdW interaction and quantum fluctuations associated with the driving field [127]. For positive values of detuning, $\Delta > 0$, the system exhibits a ground-state continuous transition from a crystalline phase of excited atoms into a paramagnetic phase corresponding to a relatively large Rabi frequency (reported in Ref. [128]).

However, in a more realistic case where the system lives in the presence of dissipation, the surrounding environment induces extra fluctuations (thermal or even non-thermal) and steers the system to a non-equilibrium steady state. The corresponding steady-state phase transition thereby might not have the same properties as that of the ground state. In our model, it turns out that a first-order phase transition takes place between a gaseous phase of low-density Rydberg excitations and a liquid-like phase with high density. Crucially, the is a result of the interplay between the coherent and the dissipative dynamics as the former enforces extensive correlation while the latter degrades it. Moreover, since the Ising-universal liquid-gas transition does not exhibit any phase transition in one dimension (having *the lower critical dimension* of one), we hereby consider a two-dimensional model.

In the following, we will proceed with the variational technique providing a detailed quantitative analysis on how local dissipative channels affect long-range order and phase transition.

5.4.1 Coherent drive vs decay

As we mentioned in Chapter 3, our variational method for long-range interacting systems is based on an infinite repetition of a fixed-size cluster of sites in the underlying lattice using periodicity in the boundary condition. A finite-size analysis is then performed to obtain the phase diagram. However, before getting to the numerical simulations, we outline the basic mechanisms which lead the system to the expected steady state. First of all, the driving field generates a coherent superposition of the ground state and the Rydberg state of each atom. Secondly, due to the large C_6 coefficient, the blockade effect is in place resulting in anti-correlation between Rydberg states. However, the strength of the blockade effect can be reduced by having positive detuning which decrease the interaction-induced energy shift of $|rr\rangle$ states. In the extreme case, a large enough detuning can fully compensate for the energy shift being known as the *facilitation or anti-blockade regime* [129, 130]. Thirdly, the local decay of Rydberg states on its own steers the system to the ground state $|ggg...g\rangle$. Finally, we have dephasing which destroys quantum coherence and guides the system to a maximally mixed state.

Initially, we investigate the interplay between the coherent driving field and the decay. To this end, we set $\gamma_a/2\pi = 1$MHz and $\gamma_p = 0$. Now, we can quantify the phase transition in terms of Ω and Δ. In fact, since the steady-state phase transition manifests itself in terms of a non-analyticity in the variational norm, we can see an abrupt change in the gradient of the variational norm (see Fig. 5.2(a)). This non-analyticity corresponds to a crossing of the values of two local minima in the variational norm. Fig. 5.2(b) shows the Rydberg density, i.e. $(\langle\sigma_z\rangle+1)/2$, displaying first-order transitions between these two solutions for different values of Δ.

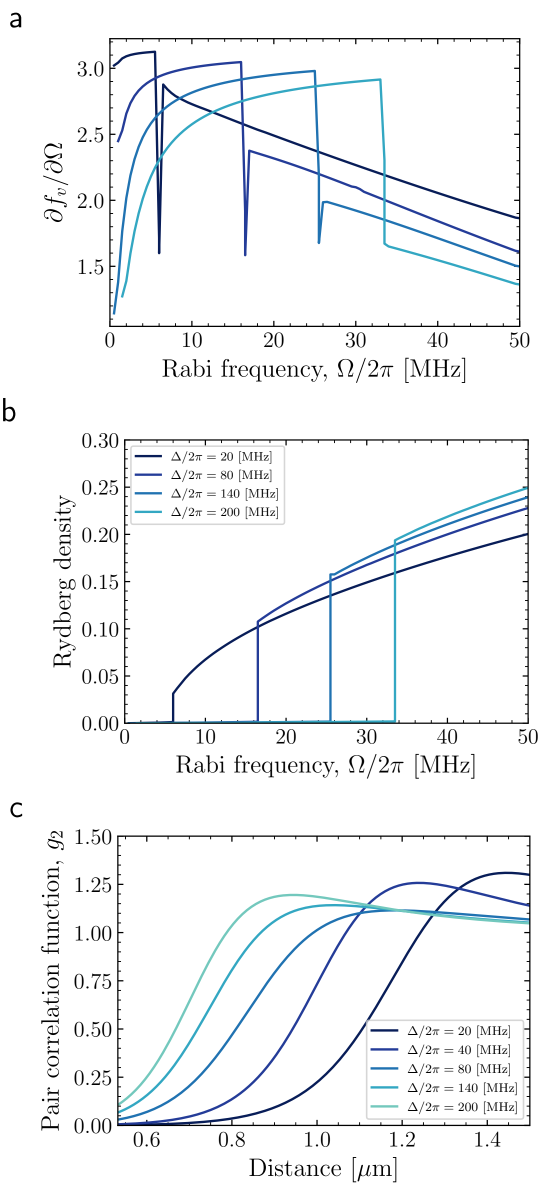

Figure 5.2: Variational results for the steady state of 2D driven-dissipative Rydberg gases with $\gamma_a/2\pi$ = 1MHz. (a). Numerical gradient of the variational norm $\partial f_v/\partial\Omega$ exhibits discontinuity for different values of detuning Δ. (b) The corresponding first-order transition is shown in terms of Rydberg density. (c) Pair correlation function g_2 demonstrates decrease in Rydberg blockade radius by increasing Δ at $\Omega/2\pi$ = 50MHz (In these calculations cluster size is 9×9).

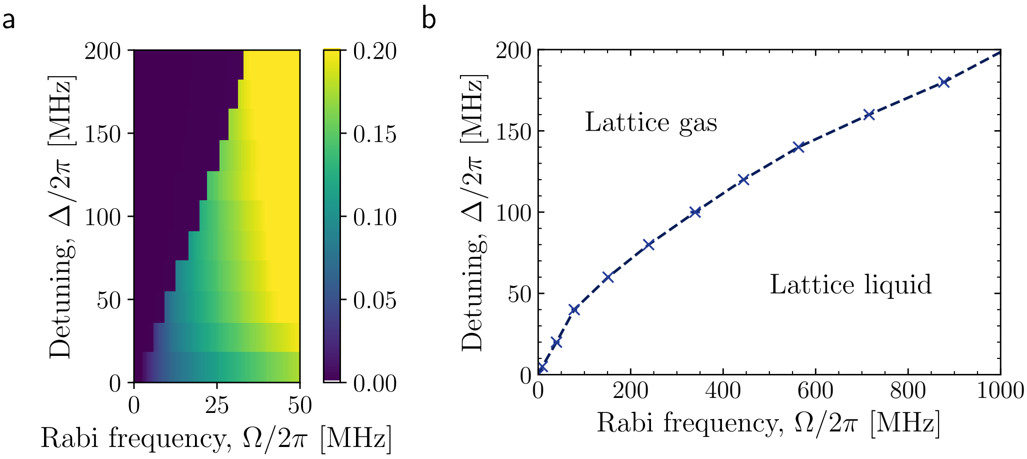

Figure 5.3: Steady-state phase diagram for driven-dissipative Rydberg gases obtained by finite-size scaling of the variational results. (a) Color-coded Rydberg density and (b) lattice liquid-gas phases in the Δ-Ω plane (the step-like discreteness in (a) is only because of the numerical resolution).

As it can be clearly seen in Fig. 5.2(b), for low Ω the Rydberg density is extremely small implying a very dilute gas of Rydberg excitations. This comes from the strong blockade effect being combined with the decay of the Rydberg excitations which makes it different from the anti-ferromagnetic phase appearing in the short-range interacting case [98]. However in the liquid phase, the Rydberg density ramps up with an asymptotic tendency to the maximally-mixed state for a very large Ω. Also, due to the facilitation mechanism arising from positive detuning, Rydberg density in the liquid phase increases by increasing Δ. This is associated with a reduction in the Rydberg blockade radius demonstrated in Fig. 5.2(c) where the pair correlation function is plotted for varying detuning and a fixed value of $\Omega/2\pi = 50$MHz.

Now, we are in the position to evaluate the phase diagram in the thermodynamic limit of the model. To this end, we perform a finite-size scaling of the variational results for three cluster sizes of 5×5, 7×7, and 9×9. The choice of odd numbers is twofold; First, this makes it easier for the numerical calculation of the variational norm as it can be constructed around a site at the center of the lattice. Second, the finite-size scaling should be performed on either even-number sizes or odd-number sizes since they have different scaling of interparticle distances.

Finally, we present the phase diagram in the Δ-Ω plane in Fig. 5.3. To get an impression of the density of each phase, a contour plot of the Rydberg density is shown in Fig. 5.3(a). One clearly observes that the liquid phase contains a wide range of Rydberg density as a function of the coherent field. Fig. 5.3(b) displays an evaluation of the phase diagram for relatively large values of Δ and Ω. As a matter of comparison, in these calculations, the nearest-neighbor interaction strength is $C_6/a^6 \approx 882\text{MHz}$.

Within our method, the minimization of the variational norm yields a global minimum indicating that the steady state is always unique. In other words, the phase diagram shows no finite region of bistability similar to the case of the dissipative Ising model studied in the previous chapter. In the same way, a narrow band of bistability is expected due to the thermal nucleation around the first-order line.

An important take-away from the phase diagram is that the phase transition of the model resembles that of the dissipative Ising model with short-range interaction as in Chapter 4 (detailed analysis can found in Ref. [39]). This indicates that the dissipative Ising model with proper values of the parameters effectively describes phase transitions in driven-dissipative Rydberg gases. In other words, following the discussion in Appendix D one can expand the interaction Hamiltonian in Eq. (5.9) in terms of σ_z. This leads to a long-range Ising-type interaction with power-law decaying and a specific value of Δ. The long-range coupling can in turn be captured by an effective short-range factor as well as a longitudinal field depending on a cutoff radius

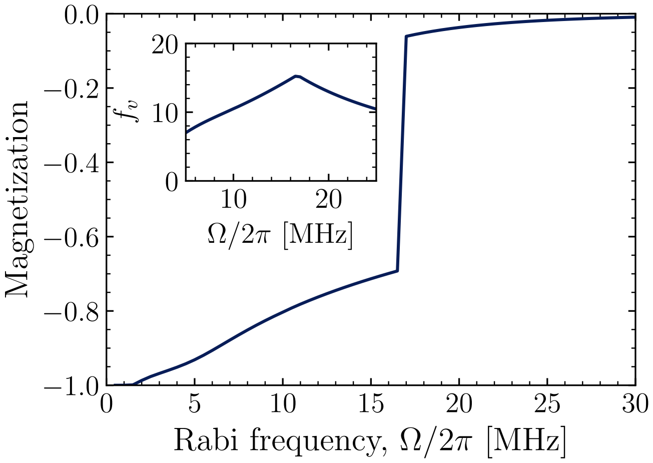

Figure 5.4: Variational results for the steady state of an effective dissipative Ising model with a cutoff radius of $r_c = \sqrt{5}$. Increasing the Rabi frequency Ω induces a sudden change in the magnetization $\sum_{i=1}^{N}\langle\sigma_z^i\rangle/N$ signaling a first-order phase transition. The inset reflects the corresponding non-analyticity in the variational norm f_v.

r_c, i.e.

$$H_{\text{eff}} = h_z(r_c) \sum_i \sigma_z^{(i)} + \frac{\Omega}{2} \sum_i \sigma_x^{(i)} + J_{\text{eff}}(r_c) \sum_{\langle ij \rangle} \sigma_z^{(i)} \sigma_z^{(j)}. \tag{5.16}$$

We can verify this correspondence by performing the numerical simulation of the effective model. As an instance, we choose a moderate value of $h_z = J_{\text{eff}}/2 \approx 14.3\gamma_a$ by setting $r_c = \sqrt{5}$. The corresponding variational results are shown in Fig. 5.4 that confirm the existence of a first-order phase transition very similar to that of the original Rydberg system. We conclude that in Rydberg gases, the long-range vdW interaction doesn't alter the nature of the underlying dissipative phase transition.

5.4.2 Coherent drive vs dephasing

Let us now turn on the phase damping channel via having a finite dephasing rate $\gamma_p > 0$ in addition to the decay process with a fixed rate of $\gamma_a/2\pi = 1$MHz. In this case, the variational norm is altered up to a contribution of dephasing in the Lindblad master equation on top of the associated modification in coefficients appearing in Heisenberg equations (5.15).

Crucially, it is well known that strong dephasing significantly increases the population of Rydberg excitation being extensively employed to create blockade-assisted artificial super atoms [131, 122]. To be more precise, dephasing degrades the symmetrically populated state of the Rydberg Hamiltonian via populating asymmetric states giving rise to an enhancement of the Rydberg density [132]. In a more experimental point of view, the broadening in linewidth of the driving field caused by technical noise gives access to more energetic states containing a higher fraction of the Rydberg state.

Fig. 5.5 demonstrates the interplay between dephasing and the driving field in terms of Rydberg density. It clearly confirms the enhancement of the Rydberg population by increasing γ_p. Notably, it reveals how rising dephasing decreases the height of the first-order jump in Rydberg density leading to a critical point beyond which any quantum phase transition is eradicated. This is in sharp contrast with the effect of an strong decay in which the phase transition disappears due to the enhancement of the ground state $|ggg...g\rangle$. Moreover, this is a way to access criticality in dissipative Rydberg gases [92].

In summary, we have analyzed the stationary properties of strongly interacting Rydberg gases using a proper many-body ansatz capturing long-range correlations. In particular, the interplay between local dissipation sources and a coherent driving field has been studied. We found that while the presence of a decay process is associated with a first-order phase transition, a

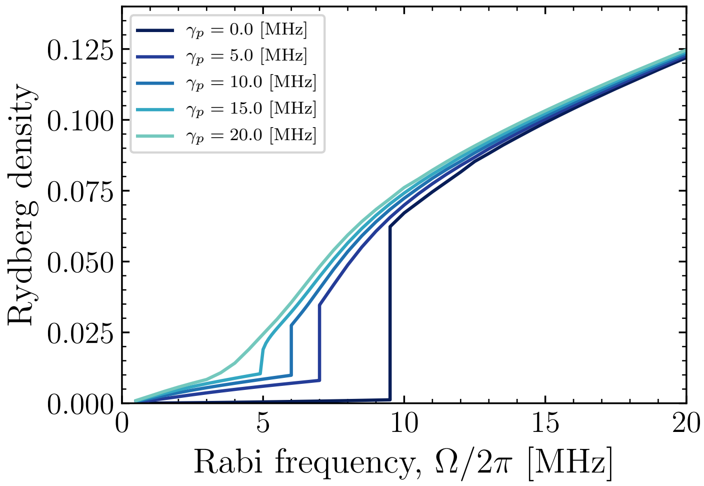

Figure 5.5: Stationary Rydberg density in the presence of weak decay $\gamma_a/2\pi =$ 1MHz and different rates of dephasing γ_p.

rather strong dephasing process can eradicate it.

Our method, in principle, can be applied to any long-range dissipative spin model provided that the required ansatz is properly constructed. Although the variational approach might not be quantitatively accurate, we re-emphasize that it makes it possible to approach those regimes which are beyond the access of more sophisticated numerical methods such as tensor network method.

Part III

Dissipation-Assisted Unpredictable Dynamics

After Turing, it seemed to me, one could assert with confidence that all our hopes, fears, sensations, and choices were just evanescent patterns in some sort of cellular automaton.

— Scott Aaronson

Chapter 6

Dissipative cellular automata

In Part II, we have mainly focused on the stationary properties of open many-body systems by introducing the notion of genuine bistability in Chapter 4 and analysing long-range correlations in Chapter 5. In this part, we turn our attention to the dynamical behavior of open many-body systems. In particular, we would like to implement different classes of dynamical behavior building upon the irreversibly in dissipative systems.

In this chapter, we specifically investigate open many-body systems with *unpredictable dynamics* in the sense that a state of such systems at an arbitrary time t is unknown unless the corresponding dynamics is fully simulated from the beginning to the time t. Our study is conducted in the framework of cellular automata, conceptually simple systems yet exhibiting different dynamical behaviors including unpredictable behavior [133, 134, 135, 136]. We first introduce a master-equation embedding of irreversible cellular automata in contrast to the commonly quantum version of cellular automata which are reversible due to their unitary dynamics [137, 138, 139, 140, 141]. While the latter requires fault-tolerant quantum computers with more than 10000 qubits which are at least a decade away to reach, the former seems to be more promising as they are intrinsically more robust against noise [142, 117]. In particular, our setting allows controlling the dynamical behavior of the underlying open system in terms of a cycle time introduced by the embedding giving rise to a phase transition between predictable and unpredictable behavior. We proceed by introducing a competing process which induces quantum fluctuations and dissipatively drives the system to highly entangled states. Interestingly, we show that under the right conditions, entanglement and unpredictability can coexist even in the long time limit.

6.1 Elementary cellular automata

The *elementary cellular automata* (ECA) are one-dimensional dynamical systems known to be the minimal model exhibiting unpredictable behavior. An elementary cellular automaton contains an array of cells with two possible values, say 0 and 1, as well as updating rules depend on the current states of each cell and its nearest neighbors. This 3-site neighborhood consists of 2^3 binary configuration which in total gives rise to $2^{2^3} = 256$ ECA with different updating rules, each of which can be indexed with a decimal number of its 8-bit binary set of rules. The discrete-time evolution of ECA is then obtained by starting with a binary array in the first row, the next generation based on the corresponding rule in the second row, and so on. For instance, rule $110_{10} = 01101110_2$ which is depicted in Fig. 6.1 demonstrates how individual sites evolve through a discrete-time based on the corresponding conditional rule. Simply, a site's state at the next time depends on the state of the 3-site neighborhood at the current time.

6.1.1 ECA classification

The discrete space-time outcomes of ECA illustrate structurally different patterns given a specific rule and an initial state. Crucially, while the initial state changes the resulting pattern, the rule itself essentially determines the intrinsic nature of the patterns. The fundamental dynamical properties of these ECA rules are accordingly categorized into four distinct classes, also known as *Wolfram's classification* [143, 144]. These classes are usually labeled in the following order,

1. Class I (uniform): Systems with fast evolution toward a homogeneous steady state.
2. Class II (periodic): Systems evolving periodically generating repeated patterns.
3. Class III (chaotic): Systems evolving in a chaotic fashion resembling random patterns.
4. Class IV (complex): Systems whose evolution encompasses non-trivial emerging structures coexisting with the patterns of the previous classes.

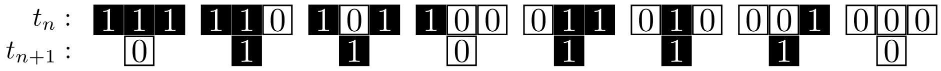

Figure 6.1: Updating ruleset of ECA rule 110 = 01101110_2.

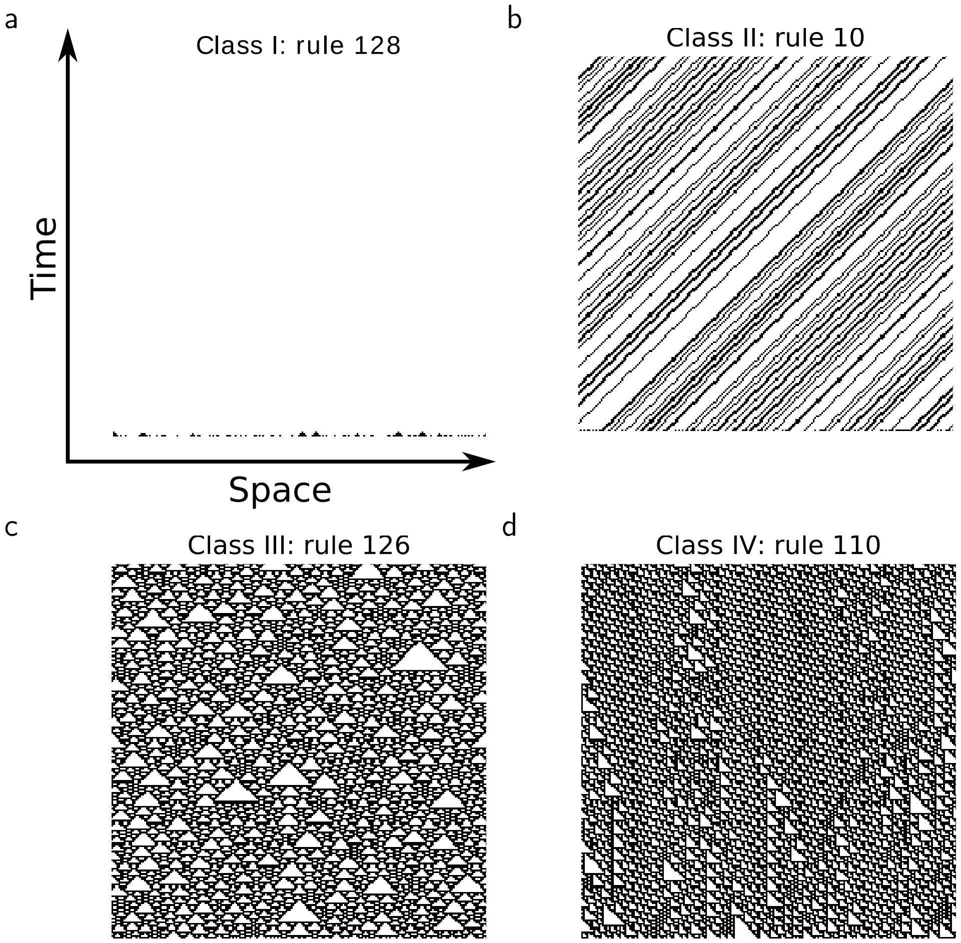

Figure 6.2: Wolfram's classification of elementary cellular automata consists of (a) class I with uniform steady states, (b) class II with periodic patterns, (c) class III with chaotic behavior, and (d) class IV with complex dynamics. In each pattern, the first bottom row corresponds to a randomly chosen initial state evolving upwards in time.

In a broader sense, this classification captures the dynamical properties of translation-invariant systems including cellular automata [145]. Figure 6.2 illustrates the four classes in terms of space-time patterns given some rules and random initial states. As seen in Fig. 6.2(a), ECA rules of Class I such as rule 128 quickly reach a homogeneous stationary state similar to the time evolution of ordinary dissipative systems. In rules of Class II like rule 10 in Fig. 6.2(b), the evolution is however periodic with limit-cycle oscillations. In Class III, systems are chaotic in a sense that the associated evolution gives rise to positive *Lyapunov exponent* [146] and large constant value of entropic measures after a relatively short time. Taking into account the difficulty of generating random numbers from a deterministic system, ECA rules belonging into Class III (as shown in Fig. 6.2(c) for rule 126) give access to (pseudo-)random binary patterns while the underlying updating rules are totally deterministic. Last but not the least, Class IV refers to dynamical systems with diverging transient times [147] and emerging non-trivial patterns in the evolution space, known as *self-organization*, signaling a complex behavior.

A specific example of Class IV is rule 110 showing *complex pattern* as it is depicted in Fig. 6.2(d). Rule 110 is the simplest cellular automaton which has been proven to be *Turing P-complete* [135, 136]. This implies that, in principle, it can simulate any Turing machine in polynomial time. The computational power of rule 110 comes from the frequent appearance of self-perpetuating localized structures in the spatio-temporal evolution. As seen in Fig. 6.3, these structures which are known as *gliders* are simply a sequence of triangular tiles whose interactions/collisions can be employed to perform computations. Noteworthy, rule 110 can be thought of as the one-

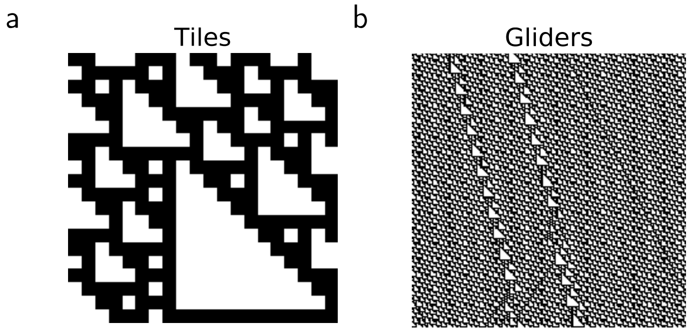

Figure 6.3: Blocks of binary cells in ECA rule 110 with emerging (a) micro triangular Tiles and (b) sequences of tiles known as Gliders.

dimensional counterpart of the well-known *Conway's game of life* which is a Turing-complete cellular automaton in 2D [148].

It is conjectured that the Class IV systems are *computationally universal* [143], being capable of doing any generic computation. This implies that it is *undecidable* to determine the behavior of such systems given an initial state unless the dynamics are simulated from the beginning to the end. The undecidability of Class IV is a corollary of the generic decision problem in computability theory, also known as *halting problem*, asserting that it is impossible to write a program that could predict whether any other program with a given input terminates or will run forever [149]. Moreover, very interesting similarities have been found between the computational power in Class IV and critical behavior in systems near phase transitions [150]. From this point of view, ECA rules under Class IV are sometimes called *edge of chaos* cellular automata since they manifest themselves as critical phases at the edge between regular periodic and chaotic behavior.

6.1.2 Complexity classes and unpredictability

The fuzzy notion of *complexity* as "the amount of information needed to describe everything interesting about the system"[151] makes it very difficult to be quantified. That is why we need to narrow down the definition to something graspable in context. In particular, Class IV behavior is said to be complex in the sense that the underlying individual binary cells interact in a way that results in an unpredictable collective behavior, also being referred to as *emergent phenomena*. The quantitative identification of such behavior is not possible using the conventional measures exploited for the other classes. For instance, while entropic measures or Lyapunov exponents can capture the randomness in the dynamics of the Class III systems, they fail to identify the emergent group dynamics in Class IV.

One possible treatment of such systems with discrete variables is to analyze the computational strings encoding the state of the system from an algorithmic information perspective. Crucially, the *algorithmic complexity* of any string of data S is defined as the length of the shortest computer program coded to output S, also known as *Kolmogorov complexity* $\mathcal{K}(S)$ [152]. While it is impossible to compute Kolmogorov complexity itself (recognized as a no-go theorem), there are however commutable upper bounds to $\mathcal{K}(S)$ providing practical application [153]. In particular, one of these bounds is given by the *compression length* $\mathcal{C}(S)$ satisfying

$$\mathcal{C}(S) = \mathcal{C}_c(S) + \mathcal{C}_0 \geq \mathcal{K}(S), \tag{6.1}$$

where here $\mathcal{C}_c(S)$ denotes the compressed length of S computed by a compression program with the length of $\mathcal{C}_0$ being identical for all strings S. Having said that, the crude application of Kolmogorov complexity (or the compression length) is not sufficient for classifying dynamical systems. Specifically, this is very challenging when it comes to Class III and Class IV systems as they both exhibit large values of $\mathcal{K}(S)$.

However, a key difference between Class III and Class IV makes it possible to differentiate them from each other. Crucially, while the chaotic Class III systems are known to be highly sensitive to small changes in the initial state irrespective of the state itself, the latter is not true in the Class IV systems [154, 144]. In other words, differential measures of Kolmogorov complexity for Class IV systems are finite, (in contrast to vanishing values for Class III), since in these systems the Kolmogorov complexity behaves differently for different initial states. This is related to the universal computing capabilities of Class IV systems as one can encode a program in terms of the initial state. While some programs may result in complicated computations showing a high Kolmogorov complexity, others can lead to relatively simple results.

This instability can be defined based on a generalization of the notion of Lyapunov exponent to algorithmic complexity so that it captures the sensitivity in compressibility of the ECA's patterns due to small changes in the initial state [154]. We refer to this as the *characteristic compression exponent* which is given by

$$\delta_n(t) = \sum_{j=1}^{n-1} \frac{\left|\mathcal{C}_c(S_j(t)) - \mathcal{C}_c(S_{j+1}(t))\right|}{n-1}, \tag{6.2}$$

where $S_j(t)$ indicates space-time outcomes of all the sites evolving from an initial state j until an arbitrary (discrete) time t; The initial state is chosen from n ordered configurations according to the Gray code enumeration scheme [155]. Using this scheme, one can order binary strings in such a way that the two successive strings differ in only one of the digits (see Fig. 6.4). This is the least possible amount of change in the initial state (Hamming distance of 1) which ensures that the variations in the compression lengths are only due to the dynamical rules, not the initial condition [154]. Regarding the compression algorithm, we use an implementation of the lossless DEFLATE algorithm [156] using `zlib.compress` function in Python 3.6.9.. It would be also very interesting to use quantum compression algorithms [157, 158, 159, 160] for Class IV systems, but we leave it as an outlook for future studies.

In Class IV systems, the characteristic exponent $\delta_n(t)$ is increasing in time in a linear form for sufficiently large n and t, sometimes referred to as the

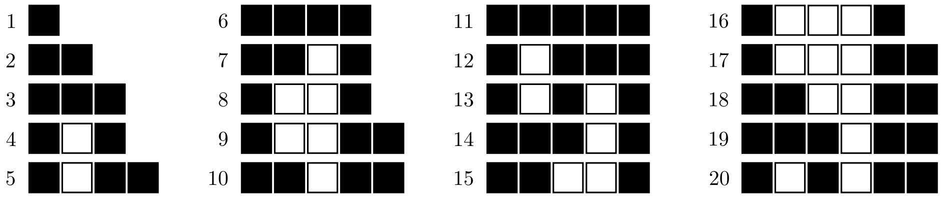

Figure 6.4: The first 20 binary configurations in the Gray code enumeration scheme. Here, the right side of each configuration consists of an arbitrarily long array of white cells.

second law of complexity [161]. Importantly, the slope of the characteristic exponent, i.e.

$$S_\delta \equiv \frac{d\delta_n(t)}{dt}, \tag{6.3}$$

vanishes for Class III systems while being positive for Class IV systems. Therefore, one can use S_δ as a computable quantity to identify Class IV behavior. We here employ the notion of *unpredictability* to describe the complex behavior in Class IV systems. By this we mean, while one can predict statistical properties of chaotic Class III systems in the long time limit at a coarse-grained level [162], Class IV is unpredictable even by granularization. Unpredictability is closely related to what is called *sophistication* in computer science which is a generalization of Kolmogorov complexity to capture “neither simple nor random” behavior estimated by compression length of coarse-grained representation of states [151].

6.2 Embedding of elementary cellular automata

ECA rules are mostly irreversible. This can be simply seen in the underlying rulesets which are defined as a map from three input bits to one output bit. Consequently, a direct implementation in a quantum system is not possible if the operations are unitary. Here, we instead need to make use of a dissipative quantum channel $\mathcal{V}_{\mathrm{ECA}}$ generating the desired state at time $t+1$ given the state at the previous time, i.e.

$$\rho(t+1) = \mathcal{V}_{\mathrm{ECA}}\rho(t). \tag{6.4}$$

The quantum channel itself requires a generator that can be expressed in terms of a purely dissipative Lindblad operator,

$$\mathcal{L}\rho \equiv \frac{d}{dt}\rho = \gamma \sum_i \left(c_i \rho c_i^\dagger - \frac{1}{2}\left\{ c_i^\dagger c_i, \rho \right\} \right), \tag{6.5}$$

with c_i being jump operators encoding the local ruleset of the ECA rule of interest and γ denoting the characteristic rate of the dynamics. Here, we can retrieve the desired channel $\mathcal{V}_{\mathrm{ECA}}$ in the infinite time limit of the dissipative dynamics leading to the state $\rho(t+1)$ in the form of a steady state.

Now, let us elaborate on the underlying open quantum system. We here propose a two-ring setting with N sites on each ring under the periodic boundary condition. We have to mention that while the periodicity is desirable for pattern formation, it is not a necessary condition as one can also consider proper fixed boundary conditions in the case of practical implementation of the setting [163, 164]. Withing the two-ring setting, each site represents a qubit with $|0\rangle$ shown as a white cell and $|1\rangle$ shown as a black cell. Consequently, the jump operators c_i^c required to implement the channel take the following form,

$$c_i^c = \sum_k o_{\bar{i},k} Q_{i,k}, \tag{6.6}$$

where $Q_{i,k} = |k\rangle\langle k|$ demonstrates a projection operator acting on the sites $i-1$, i, and $i+1$ of what we call the *input ring*, while $o_{\bar{i},k}$ is a single-site operator acting on the corresponding central site i on the *output ring*. The index k runs over all eight basis states on the 3-site neighbourhood. Table 6.1 shows the eight states k and the corresponding operation $o_{\bar{i},k}$ according to ECA rule 110. The structure of c_i^c is such that an annihilation/creation of an alive cell occurs in site i attaching to the output ring provided that the states of the corresponding site on the input ring and its neighboring sites lead to non-vanishing $\langle Q_{i,k}\rangle$, see Fig. 6.5(a). In other words, the required quantum jump operators are quasi-local, i.e. 3-site projection operator plus a single-site annihilation/creation operator, which makes them highly desirable for

State k at t	111	110	101	100	011	010	001	000
Operation o_k	σ_-	σ_+	σ_+	σ_-	σ_+	σ_+	σ_+	σ_-

Table 6.1: Jump operators for ECA rule 110 indicating how the central site on the output ring undergoes an operation o_k depending on the state k on the input ring. The ruleset for the corresponding rule 137 can be found by inverting all inputs and outputs.

practical implementation purposes.

Within this setting, we first initialized both rings with a desired Gray code configuration. We then run the dissipative dynamics by setting one of the rings as the input ring and the other as the output ring. The role of the rings is reversed after a *cycle time* t_c, see Fig. 6.5(b). Finally, the associated space-time pattern of the underlying rule can be reproduced in the limit of infinite t_c. The pattern is captured in terms of the expectation values $\langle P_i^{(1)} \rangle$ on the output ring at the end of each interval, see Fig. 6.5(b).

It is also worth looking at the case of finite cycle time t_c, which implies that the time evolution of the corresponding ECA rule becomes probabilistic hence generating computational errors. However, we expect that the Turing-complete Class IV systems can tolerate a finite amount of errors, similar to error correction codes which can clean up noisy data introduced by corrupted classical systems. This of course won't hold in the limit of $t_c \to 0$ where the noise becomes dominant. As a result, varying the cycle time t_c in the two-ring setting may simply alter the dynamical features of the underlying system. In the next section, we make us of the cycle time t_c as a control parameter to detect a phase transition between predictable and unpredictable behavior.

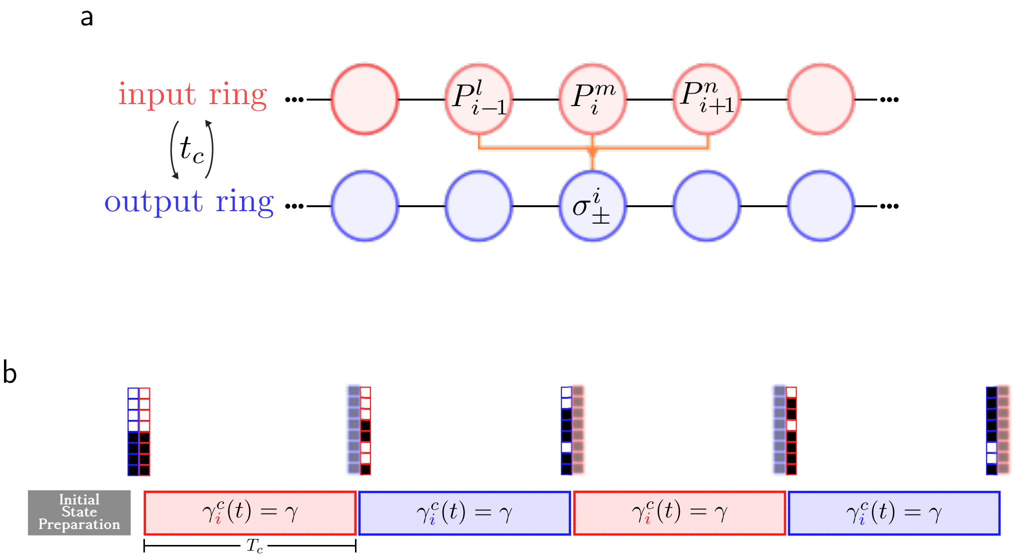

Figure 6.5: Master equation embedding of ECA rules (a) on two rings of sites (b) using a periodic application of 4-site jump operators generating the space-time pattern of the rule of interest with finite cycle time t_c.

6.3 Cycle time phase transition

In this section, we will show some numerical results obtained from Monte-Carlo simulation of the master equation embedding of rule 110 with finite t_c and also in the presence of quantum fluctuation.

6.3.1 Purely classical dynamics

Here we investigate how the duration of the cycle time t_c affects the dynamics of ECA rule 110. Note that the dynamics of the ECA rules are purely classical leading to fully diagonal density matrices. In order to simulate the master equation, we hereby make use of Monte-Carlo sampling which performs efficiently for classical dynamics. Fig. 6.6 summarises the corresponding numerical results. Notably, our tunable implementation of rule 110 shows an significant change in the slope of the characteristic compression exponent S_δ at a finite value of t_c, depicted in Fig. 6.6(a). This indicates a phase transition from a chaotic phase (Fig. 6.6(b)) with vanishing S_δ to an unpredictable phase (Fig. 6.6(c)) with finite S_δ. While it has been shown that different statistical measures of complexity can be used to detect variant phase transitions in both classical and quantum systems [165, 166, 167, 168], the observed phase transition in complexity (i.e. unpredictability) itself is novel.

Importantly, we observe that the value of S_δ grows in a non-trivial way by the system size N. This is because the emergent glider structures are much larger than the three-site unit cell of the ECA [135]. For instance, $N = 11$ is the smallest system size in which the gliders appear. Fortunately, by choosing specific system sizes we can still perform finite-size scaling of S_δ, see the inset of Fig. 6.6(a). More precisely, we only take into account those system sizes at which S_δ is at a local maximum. Similar techniques have been employed in the context of systems with strong incommensurability effects [128, 169]. According to the finite size analysis, the phase transition takes place at $t_c = 5.80 \pm 0.08$ in the thermodynamic limit. We should mention that while it has been shown that the finite-size scaling theory breaks down when it comes to the extrapolation of unpredictability in the thermodynamic limit [170], detection of a chaotic-unpredictable phase transition is feasible as the chaotic phase has the computable value of $S_\delta = 0$ in the thermodynamic limit (in contrast to the unpredictable phase which deviates from $S_\delta = 0$ by increasing the system size).

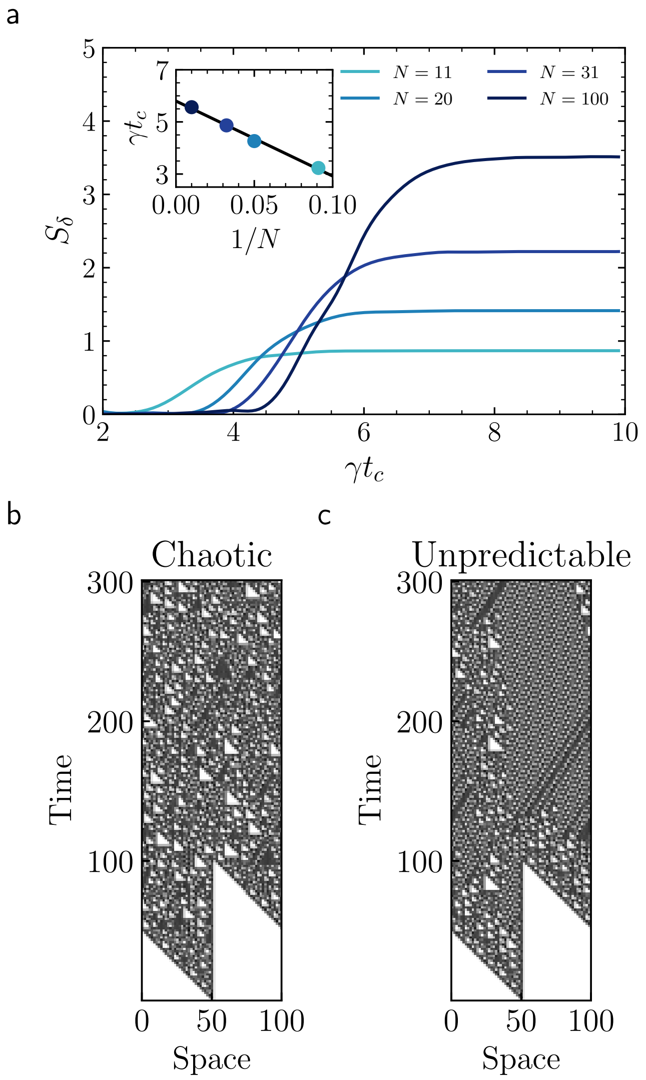

Figure 6.6: (a) Cycle time phase transition in ECA rule 110 captured by the slope of the characteristic compression exponent S_δ. Finite size scaling (inset) points to a value of $\gamma t_c = 5.80 \pm 0.08$ for the transition in the thermodynamic limit. (b) Typical trajectory of the rule 110 for a relatively short cycle time, $t_c = 4/\gamma$, evolving from a single alive (black) cell resembles a chaotic Class III behavior. (c) For larger cycle time (here $t_c = 10/\gamma$) the unpredictable phase appears with emergence of gliders in the space-time pattern. In these calculations, we set $n = 50$ and $t = 300$ to obtain convergence in S_δ. For each initial state, 100 Monte-Carlo samples were taken.

We have successfully shown that our setting has the ability to replicate the unpredictable Class IV behavior which is highly interesting due to the universal computing capabilities. Also, the chaotic phase that appears within this setting, displays rich dynamics which resembles an ongoing pattern generation with environment-assisted innovations. Interestingly, such behavior is out of relevance in studying biological mechanisms [171]. Moreover, the two-ring setting allows us to look at dynamical behaviors in the presence of quantum fluctuations. It is out of interest to study how quantum properties like quantum superpositions and entanglement co-occur with both Class III and Class IV behavior. Therefore, the rest of this chapter goes in this direction.

6.3.2 Competition with entanglement

To address the effect of quantum fluctuations on the unpredictable dynamics, we need to briefly introduce the concept of *quantum cellular automata* (QCA). QCA (in analogy to classical cellular automata) are commonly defined as an array of qudits which evolve under a unitary propagator in a discrete time (see some examples in Refs. [137, 138, 139, 140, 141] and recent reviews in Refs. [172, 173]). Unitary QCA are originally devised to model quantum computations. However, experimental realization of such systems using NISQ devices is of course challenging. Alternatively, there are different proposals to realize dissipative variants of QCA [142, 117] building upon the established theory of open quantum systems. Non-unitary QCA are specifically out of relevance here as they are intrinsically more aligned with their classical counterparts.

Here, as we wish to study the competition between quantum entanglement and unpredictability, we suggest a dissipative QCA through an interpolation of the classical ECA dynamics generated by $\mathcal{L}_c$ with a non-unitary dynamics generated by $\mathcal{L}_q$. We define $\mathcal{L}_q$ such that it also satisfies the purely dissipative Lindblad form of Eq. ((6.5)). The full Liouvillian is then given by

$$\mathcal{L} = \sin^2\left(\phi\frac{\pi}{2}\right)\mathcal{L}_c + \cos^2\left(\phi\frac{\pi}{2}\right)\mathcal{L}_q, \tag{6.7}$$

where $\phi \in [0,1]$ denotes the interpolation parameter being lower (upper) bounded in the case of fully quantum (classical) dynamics.

Regarding the quantum dynamics, we will be interested in a case that $\mathcal{L}_q$ generates highly entangled states as its fixed point. To this aim, we choose the highly entangled Rokhsar-Kivelson (RK) states also discussed in the context of lattice gauge theories, for which their dissipative preparation by correlated

State k at t	111	110	101	100	011	010	001	000
Operation O_k	μ	σ_-	μ	μ	μ	μ	μ	μ

Table 6.2: Ruleset to prepare the highly entangled Rokhsar-Kivelson state $|\psi_{\text{RK}}\rangle$. The required operator O_k is conditional to the k state on the input ring. O_k becomes either a 3-body operator $\mu_{\bar{i}} = P_{\bar{i}-1}|-\rangle\langle+|_{\bar{i}}P_{\bar{i}+1}$ acting on the three sites surrounding $\bar{i}$ on the output ring, with $|\pm\rangle = (|0\rangle \pm |1\rangle)$, or it takes the form of a single-site annihilation operator σ_- acting only on the site $\bar{i}$.

jump operators is recently proposed [174]. The RK state is basically an equal-weight superposition of all states excluding any simultaneous excitation in adjacent qubits, i.e.

$$|\text{RK}\rangle = \frac{1}{\sqrt{Z}}\prod_{k}^{N}(1 - P_{k-1}\sigma_+^k P_{k+1})|00\cdots0\rangle, \tag{6.8}$$

where $P_k = |0\rangle\langle 0|_k$ is a projection onto 0 state and Z is a normalization constant. The jump operators c_i^q required to prepare $|\text{RK}\rangle$ can be tailored in analogy with conditional updates in ECA, as follows

$$c_i^q = \sum_k O_{\bar{i},k}Q_{i,k}, \tag{6.9}$$

where $O_{\bar{i},k}$ is a 3-body operator (in contrast to the local operator in the classical case) acting on the sites $i-1$, i, and $i+1$ on the output ring. The operators inside the sum are defined such that the RK state becomes a typical dark state of the dynamics, i.e. $c_i^q|\text{RK}\rangle = 0$.

It will be helpful to align the two competing dynamics with each other, as we want to observe the interplay between unpredictability and entanglement, For this, we particularly choose ECA rule $137 = 10001001_2$ which is equivalent to Rule 110 under a $0 \rightleftharpoons 1$ transformation of the ruleset and the states. This is justified by the fact that both dynamics are biased toward the 0 state. In other words, one can simply see that while the space-time patterns in rule 110 contain more black cells (1 states), the rule 137 is reversely generating those patterns via white cells. Similarly, the RK state $|\text{RK}\rangle$ is also biased in favor of the 0 state as a result of the action of the projection operators P_k. Moreover, to have more alignment of the two competing dynamics, we divide in half the dynamics which is t_c long (see Fig. 6.7). During the first part, i.e. $t \leq t_c/2$, both the classical part $\mathcal{L}_c$ and the quantum part $\mathcal{L}_q$ are active. At the time $t_c/2$ we evaluate all necessary observables. Subsequently,

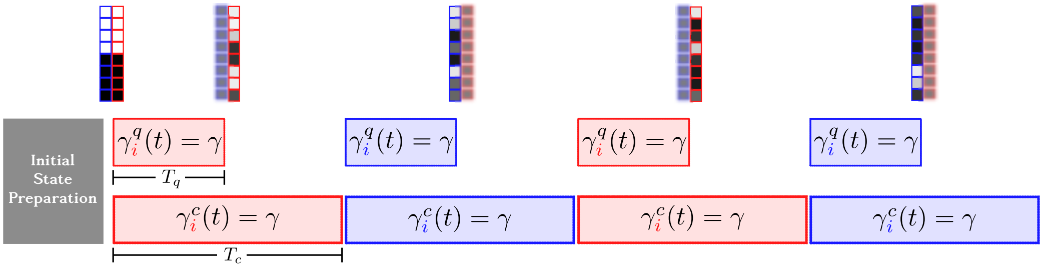

Figure 6.7: Cyclic setting in the proposed quantum cellular with cycle time being $t_c/2$ for the RK dynamics and t_c for ECA rule 137.

the second part begins where only the classical rule is acting on the system. In fact, the second part is needed to recover the unpredictable pattern which is affected by quantum fluctuations in the first part.

Now we turn to a numerical investigation of the competition between the classical rule 137 dynamics $\mathcal{L}_c$ and the quantum dynamics $\mathcal{L}_q$ preparing the RK state. To simulate the master equation in Eq. (6.5), we employ the wave-function Monte-Carlo approach [32] for 22 sites via massively parallel computations. Noteworthy, this is a slight improvement over the previously reported largest system size (up to 20 sites) for simulations retaining the full Hilbert space [31]. To compute the characteristic compression exponent δ_n, we require binary strings S_j to avoid difficulties in loss-less compression of floating-point data. Here, the Monte-Carlo sampling is especially helpful since the ith bit in the string S_j can be set as the most likely measurement result over many trajectories. In other words, we convert the expectation values to binary data such that 1 corresponds to $\langle P_i^{(1)} \rangle \geq 0.5$ and 0 otherwise.

The unpredictability of the system in terms of the slope S_δ of the characteristic compression exponent is shown in Fig. 6.8(a) as a function of the cycle time t_c and the interpolation parameter ϕ. It can be seen that in the case of the classical limit $\phi \to 1$, the expected transition to an unpredictable Class IV phase is recovered. However, in the quantum limit $\phi = 0$, while highly entangled RK states are prepared, the unpredictability is totally destroyed due to the strong quantum fluctuation. Importantly, in the intermediate region, the transition persists even away from the classical limit. Crucially, this is accompanied with entanglement as seen in Fig. 6.8(b) where negativity (see Eq. (2.5)) remains finite for sufficiently low values of ϕ. This implies that quantum entanglement and unpredictability can coexist in the system due to the proper design of the Lindblad generators. The depicted diagram in Fig. 6.8(a) is therefore an evidence that our QCA exhibits two dynamical phases with distinct degrees of unpredictability.

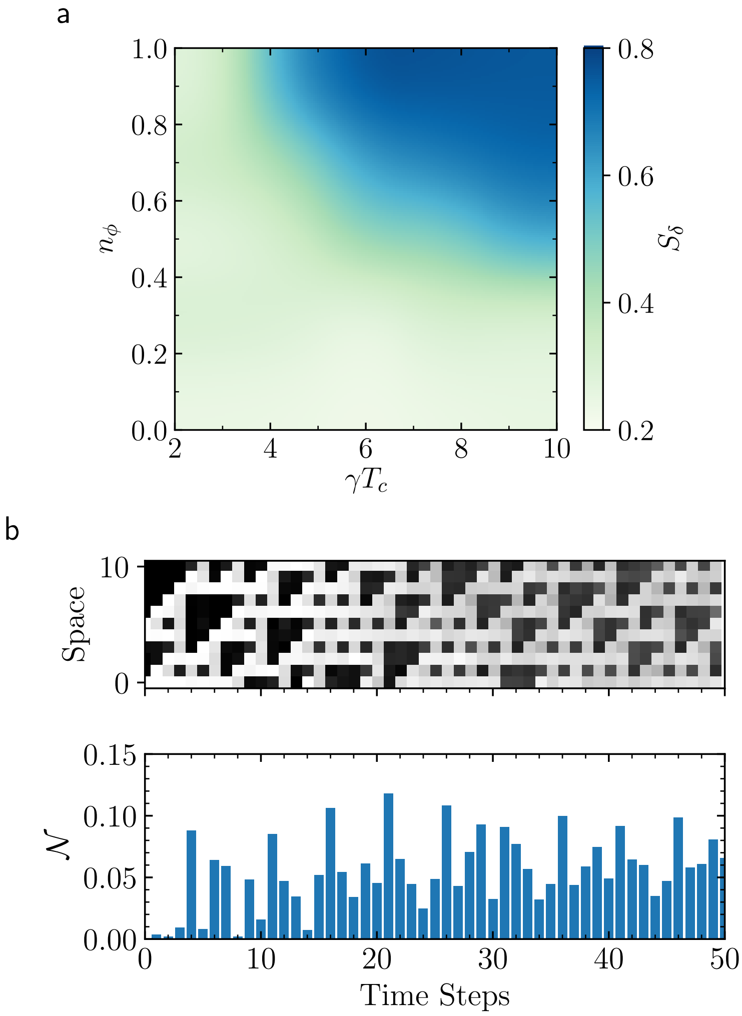

Figure 6.8: Competition between classical rule 137 and a dissipative quantum process. (a) Slope S_δ of the characteristic compression exponent as a function of the cycle time t_c and the interpolation parameter ϕ for $N = 11$ sites on each ring, showing an extended region of unpredictable Class IV behavior even in the presence of quantum fluctuations. (b) A blurry space-time pattern by averaging over 50 Monte-Carlo samples of a single initial configuration for $\gamma t_c = 10$ and $\phi = 0.6$. The corresponding states inherit multi-partite quantum entanglement calculated by quantum negativity $\mathcal{N}$ between even- and odd-numbered sites. The negativity shows a rapid increase over time and remains finite in the long time limit.

While the proposed QCA makes it possible to study novel dynamical behaviors in the context of open quantum systems, realizing such correlated jump operators is challenging in the NISQ era. We will show in the next chapter that how variational quantum simulation gives an alternative solution to this issue. Specifically, in section 7.2, we will demonstrate an efficient realization of the QCA unpredictable dynamics using a quantum co-processor based on ultracold Rydberg atoms with high fidelity.

Chapter 7

Quantum simulation of complex models

Variational quantum simulation (VQS) is an example of practical simulation using low-depth circuits with a high level of expressibility compared with synthesized digital circuits containing an extensive number of gates. These circuits are particularly of interest when it comes to the simulation of exotic and previously unexplored models with engineered multi-body interactions and correlated jump operators such as the models introduced in the previous chapters. It is worth mentioning that while it has been already studied how to engineer high-order interactions in digital quantum simulators [7, 175], VQS seems a promising approach in simulating complex quantum models using available NISQ devices without explicit realization of the corresponding interactions [49, 50, 51].

In this chapter, we especially concentrate on the variational simulation of complex open quantum systems using different quantum co-processors. We first propose a scheme for dissipative preparation of the entangled RK states using trapped-ion as the quantum co-processor similar to the experiment in Ref. [51]. Later on, we make use of a particular Rydberg-atom platform to simulate the unpredictable time evolution of the QCA introduced in the previous chapter.

7.1 Dissipative quantum state preparation

Our starting point is a variational quantum simulation of a purely dissipative time evolution ($H = 0$) which is designed to reach the RK state as the fixed point given any initial state.

7.1.1 Rokhsar-Kivelson state

As we already mentioned in Section 6.3.2, the RK state is a highly entangled state that is largely exploited in the context of lattice gauge theories and high-temperature superconductivity. The RK state is basically a ground state of a *frustration-free Hamiltonian* [176], a sum of quasilocal projection operators so that the ground state of the full Hamiltonian is equivalent to the lowest energy state of the individual terms. While it is possible to engineer such ground states in the steady state of dissipative dynamics [177], it often requires implementing correlated jump operators which might be challenging. Although there are limited protocols for realization of correlated jump operators (e.g. Appendix C), the VQS scheme makes it possible to realize any generic quantum operation. Moreover, from the perspective of quantum simulation in the NISQ era, it is highly desirable to perform useful tasks using today's qubit technologies. To this end, we propose a few-qubit simulation of dissipative dynamics toward RK state under experimental constraints over the types of measurements.

The correlated jump operators for dissipative preparation of RK states (for ≥ 3 qubits) can be represented as

$$c_i^{\mathrm{RK}} = P_{i-1}^{(0)}(|-\rangle\langle+|)_i P_{i+1}^{(0)} + \sum_{\boldsymbol{\beta}} P_{i-1}^{(\beta_1)}(|0\rangle\langle1|)_i P_{i+1}^{(\beta_2)}, \tag{7.1}$$

where $P_i^{(a)} = |a_i\rangle\langle a_i|$ is a projection operator and $\boldsymbol{\beta} \in \{(0,1),(1,0),(1,1)\}$. The resulting RK state for 3 and 4 qubits are respectively

$$\begin{aligned} |\mathrm{RK}_3\rangle &= \frac{1}{\sqrt{4}}\big(|000\rangle - |100\rangle - |010\rangle - |001\rangle\big), \\ |\mathrm{RK}_4\rangle &= \frac{1}{\sqrt{7}}\big(|0000\rangle - |1000\rangle - |0100\rangle - |0010\rangle - |0001\rangle + |1010\rangle + |0101\rangle\big), \end{aligned} \tag{7.2}$$

where no adjacent excitation is possible (see Fig. 7.1(a,b)). It is also possible to engineer the RK state, given only two controllable qubits. By modifying Eq. (7.1) into the following form

$$c_i^{\mathrm{RK}} = P_i^{(0)}(|-\rangle\langle+|)_{i+1} + P_i^{(1)}(|0\rangle\langle1|)_{i+1}, \tag{7.3}$$

one can prepare the following entangled state,

$$|\mathrm{RK}_2\rangle = \frac{1}{\sqrt{3}}\big(|00\rangle - |01\rangle - |10\rangle\big), \tag{7.4}$$

which is a subset of the many-body RK state, depicted in Fig. 7.1. In the following, we will explore the realization of Eq. (7.3) using trapped ions.

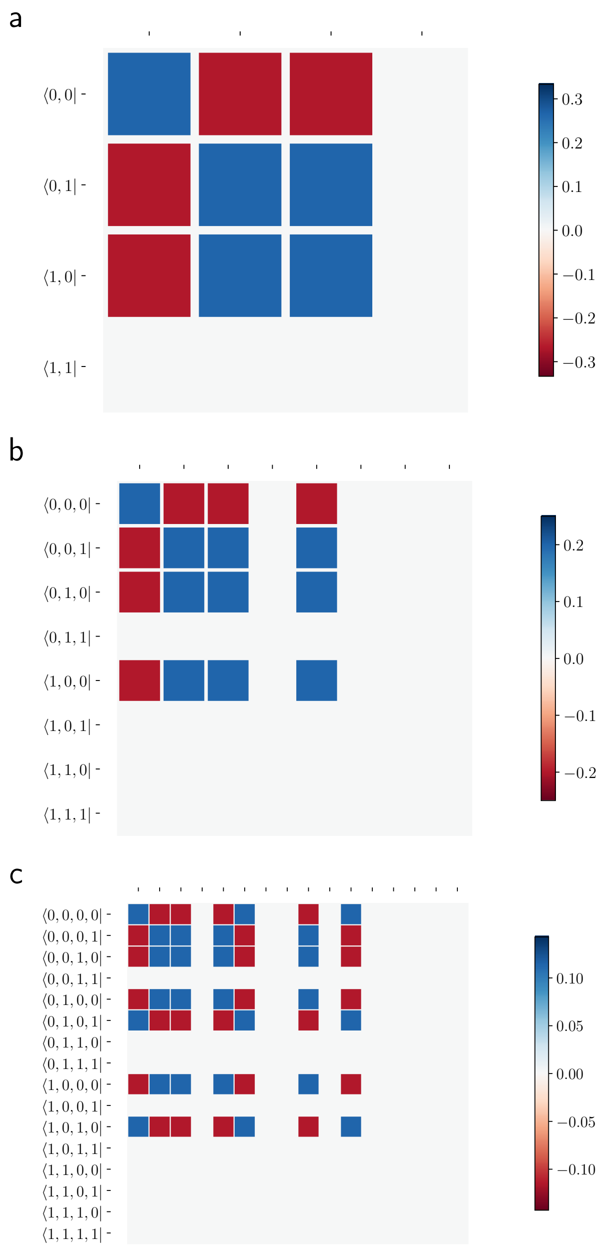

Figure 7.1: Density-matrix representation of Rokhsar-Kivelson state with (a) 2, (b) 3 and (c) 4 qubits.

7.1.2 Trapped-ion co-processor

As discussed in Section 3.3.2, trapped ions supplies a well-established quantum co-processor for variational simulation of one-dimensional systems. Here, we also envision an array of ions (such as $^{40}\mathrm{Ca}^{+}$) confined in a linear Paul trap. The valence electron of each ion is laser-driven such that it effectively represents a qubit. The native form of such a system can be described by an XX model [178] with the Hamiltonian

$$H_0 = B\sum_{i}^{N}\sigma_z^{(i)} + J_0\sum_{i\neq j}^{N}\frac{\sigma_x^{(i)}\sigma_x^{(j)}}{r_{ij}^{\alpha}}.$$

The (possible) entangled states generated by this Hamiltonian can be deformed by engineering local rotations and dissipations in VQS so that they resemble the dynamics induced by Eq. (7.3). The selected local rotations in this setting are R_x and R_y being realized by off-resonant laser beams, and the dissipator is set to be an amplitude damping channel realized by dissipative optical pumping of the qubit states (see Fig. 3.2).

Regarding the cost function Eq. (3.19), we take into account the Heisenberg equations for local Pauli matrices

$$\frac{d}{dt}\langle\sigma_x^{(i)}\rangle,\quad \frac{d}{dt}\langle\sigma_y^{(i)}\rangle,\quad \frac{d}{dt}\langle\sigma_z^{(i)}\rangle,$$

as well as the identical binary terms

$$\frac{d}{dt}\langle\sigma_x^{(i)}\sigma_x^{(j)}\rangle,\quad \frac{d}{dt}\langle\sigma_y^{(i)}\sigma_y^{(j)}\rangle,\quad \frac{d}{dt}\langle\sigma_z^{(i)}\sigma_z^{(j)}\rangle.$$

The choice of identical terms is due to fact that they are experimentally easier to be measured compared with the other binary terms.

In Fig.7.2, we provide numerical simulation results for two qubits evolving from a product initial state $\rho_0 = |{+}{+}\rangle\langle{+}{+}|$ toward the RK state. The corresponding quantum circuit is also initiated by the same state ρ_0. Moreover, we here consider identical variational parameters for the local terms (4 parameters per layer) and the circuit depth of $d = 2$. Figure 7.2(a) shows time evolution of the variational norm F_H and and the error probability ε between the exact density matrix ρ and variational state $\rho_v(\boldsymbol{\theta})$ at time t. The latter is defined in terms of the fidelity F as follows

$$\varepsilon = 1 - F = 1 - \left[\mathrm{tr}\sqrt{\sqrt{\rho_v(\boldsymbol{\theta})}\rho_e\sqrt{\rho_v(\boldsymbol{\theta})}}\right]^2. \tag{7.5}$$

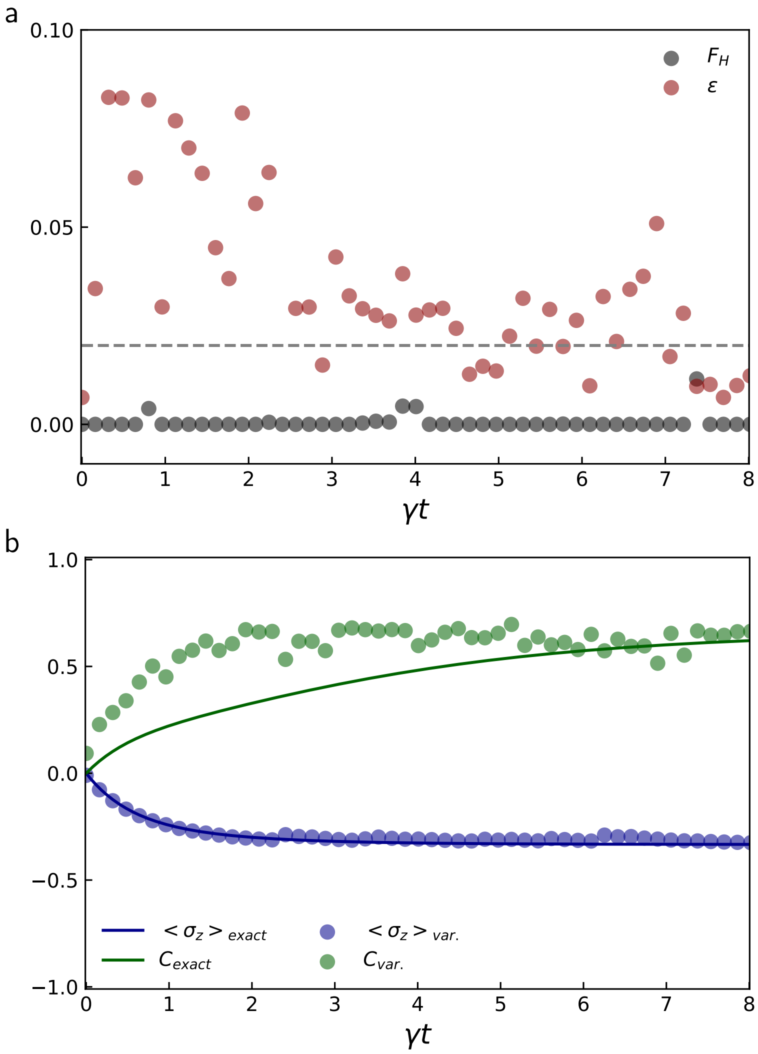

Figure 7.2: Benchmarking of the VQS approach for preparation of Rokhsar-Kivelson state for a system of two trapped ions. Variational norm F_H, error probability ε (a), expectation value of the observable σ_x and quantum concurrence C (b) as a function of time. In these calculations, the parameters are $J_0 = 100\gamma$ and $B = 10\gamma$ with γ being the dissipation rate of the corresponding jump operators.

Figure 7.2(b) exhibits the corresponding results for the time evolution of $\langle\sigma_x\rangle$ and *quantum concurrence* as a measure of two-qubit entanglement in mixed states,

$$C(\rho) = \max(0, \lambda_1 - \lambda_2 - \lambda_3 - \lambda_4), \tag{7.6}$$

where $\lambda_1 > \lambda_2 > \lambda_3 > \lambda_4$s are the ordered eigenvalues of the following Hermition matrix

$$M = \sqrt{\sqrt{\rho}\sqrt{(\sigma_y \times \sigma_y)\rho^*(\sigma_y \times \sigma_y)}\sqrt{\rho}},$$

in which the middle term denotes a spin-flip state of a complex conjugated ρ.

The benchmarking with exact numerical results in Fig. 7.2 clearly shows that the error probability ramps up immediately after the initial time reflected as a discrepancy in concurrence. This is mostly due the fact that the cost function does not include all the binary terms. However, for larger values of time, the fidelity increases ending up in the RK state with $\varepsilon < 0.02$. Therefore, these results, although preliminary, demonstrate that the available few-body qubits even with experimentally constrained measurements are useful to emulate dissipative dynamics toward entangled steady states.

7.2 Quantum simulation of unpredictable evolution

Having the VQS demonstrated quantum preparation of entangled states, we can proceed by looking at a case where the time evolution itself is unpredictable and rich in exotic entangled states. In this regard, the demonstrated QCA dynamics induced by the Lindblad generator in Eq. (6.7) is out of interest as its experimental simulation using the current experimental resources is very challenging.

7.2.1 Circuit architecture

Considering the two-ring setting of the QCA, we require some modification in the circuit introduced in Section 3.3.1. First of all, we here consider single-ring global propagators ($\mathcal{U}_g^{r_1}$ and $\mathcal{U}_g^{r_2}$), and two-ring global propagators ($\mathcal{U}_g^{r_1 2}$) as seen in Fig.7.3. We also include two separate quantum channels corresponding to a decay process ($\mathcal{D}_d$) and a dephasing process ($\mathcal{D}_p$). The operator-sum representation of the two channels are given by

$$\mathcal{D}_\mu(\rho) = \frac{1}{N}\sum_{j=1}^{N}\Big[D_{\mu_1}^{(j)}\rho D_{\mu_1}^{(j)\dagger} + D_{\mu_2}^{(j)}\rho D_{\mu_2}^{(j)\dagger}\Big], \tag{7.7}$$

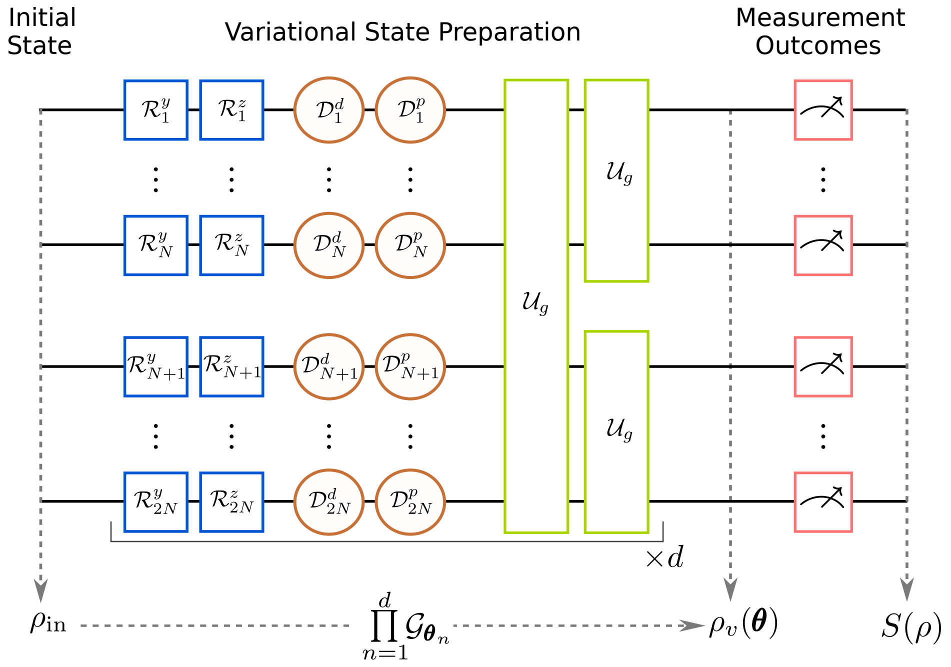
Initial State
Variational State Preparation
Measurement Outcomes
$\mathcal{R}_1^y$
$\mathcal{R}_1^z$
$\mathcal{D}_1^d$
$\mathcal{D}_1^p$
$\mathcal{R}_N^y$
$\mathcal{R}_N^z$
$\mathcal{D}_N^d$
$\mathcal{D}_N^p$
$\mathcal{R}_{N+1}^y$
$\mathcal{R}_{N+1}^z$
$\mathcal{D}_{N+1}^d$
$\mathcal{D}_{N+1}^p$
$\mathcal{R}_{2N}^y$
$\mathcal{R}_{2N}^z$
$\mathcal{D}_{2N}^d$
$\mathcal{D}_{2N}^p$
$\mathcal{U}_g$
$\mathcal{U}_g$
$\mathcal{U}_g$
$\times d$
ρ_{in}
$\prod_{n=1}^{d} \mathcal{G}_{\boldsymbol{\theta}_n}$
$\rho_v(\boldsymbol{\theta})$
$S(\rho)$

Figure 7.3: Sketch of a variational Quantum circuit for simulation of an unpredictable QCA. The circuit generates a quantum state given an initialized state ρ_{in} and a set of variational parameters $\boldsymbol{\theta} = \{\boldsymbol{\theta}_n\}_{n=1}^{d}$ for d layers encoded into the phases of the variational circuit's ingredients.

where $\mu \in \{d, p\}$ and

$$D_{d_1} = \sqrt{1 - e^{-\theta_d}} \sigma_-, \tag{7.8}$$

$$D_{d_2} = P_0 + e^{-\theta_d/2} P_1, \tag{7.9}$$

$$D_{p_1,p_2} = \sqrt{\frac{e^{-\theta_p/2}}{2}} \pm \sqrt{\frac{(1 - e^{-\theta_p})}{2}} \sigma_z, \tag{7.10}$$

The total quantum operation of each layer of the quantum circuit can then be written as

$$\mathcal{G} = \mathcal{U}_g^{r_1} \mathcal{U}_g^{r_2} \mathcal{U}_g^{r_{12}} \prod_{k=1}^{2N} \left[\mathcal{D}_k^a \mathcal{D}_k^p \mathcal{R}_k^z \mathcal{R}_k^y \right], \tag{7.11}$$

in which the local rotations include R_y and R_z. In addition, since the unpredictable QCA is a nonhomogeneous system, the phases $\boldsymbol{\theta}$ appearing in all the circuit operations are treated as independent variational parameters.

7.2.2 Rydberg-atom co-processor

Rydberg atoms trapped in arrays of optical tweezers have been demonstrated as a successful multi-dimensional platform with a high level of controllability and local addressability [179, 79, 80]. Basically, in this setup the initialized atoms (in the ground state $|g\rangle$) get illuminated with laser pulses to couple the Rydberg state with the ground state [73, 79]. The laser pulses can be tuned by time-dependent Rabi frequency $\Omega(t)$ and detuning $\Delta(t)$. This leads to the Rydberg Hamiltonian required for VQS (see Eq. (3.28)). Here, we neglect the time dependency assuming that the pulses are square-shaped.

We also need to implement independent local rotations and dissipators for the variational circuit. However, this is challenging in the Rydberg setup since local operations involving Rydberg states can activate unwanted dipolar couplings. A possible solution is to exploit *Rydberg dressing* widely used to study many-body physics [180, 181, 182, 183, 184]. This mechanism basically relies on the idea of off-resonant coupling of the ground state $|g\rangle$ with the Rydberg state $|r\rangle$ such that the resulting interaction becomes more tenable with the expense of lower interaction strength. This is allowed in the regime of large detuning, $|\Delta| \gg \Omega$, so that a perturbative treatment on the light-coupling Hamiltonian can be employed [185, 186]. A repulsive vdW interaction with red-detuned laser field gives rise to a characteristic soft-core interaction potential [181]

$$V_d(r) = \frac{V_0}{1 + (r/\xi_c)^6}, \tag{7.12}$$

where the potential height V_0 and the cut-off distance ξ_c are given by

$$\begin{aligned} V_0 &= 2\Delta\beta^4, \\ \xi_c &= \left(\frac{C_6}{2|\Delta|}\right), \end{aligned} \tag{7.13}$$

with $\beta = \Omega/2\Delta$ being called the *admixture parameter*.

In the Rydberg-dressed regime, the bare Rydberg state $|r\rangle$ is replaced by a dressed state $|d\rangle$ depending on the admixture fraction of Rydberg excitation to the ground state, i.e.

$$|d\rangle \equiv |g\rangle + \beta|r\rangle. \tag{7.14}$$

Consequently, optical control makes it possible to turn on/off the Rydberg-dressed interaction in contrast to the bare Rydberg interaction which is always present. This allows us to have local operations on the atoms by switching off the unwanted interactions.

Using a Ramsey sequence of the dressing laser and microwave pulses we end up with a slightly different resource Hamiltonian compared to the original Rydberg Hamiltonian, i.e.

$$H_0 = -\frac{\delta_{\mathrm{AC}}}{2}\sum_i \sigma_z^{(i)} + \frac{\omega_{\mathrm{MW}}}{2}\sum_i \sigma_x^{(i)} + \sum_{i<j}\frac{V_d(|\mathbf{r}_i - \mathbf{r}_j|)}{2}P_d^{(i)}P_d^{(j)},$$

being expressed in the basis of $\{|g\rangle, |d\rangle\}$ integrating out the bare Rydberg state [69]. Here, ω_{MW} indicates a microwave Rabi frequency, $\delta_{\mathrm{AC}} = \Omega^2/4\Delta$ is the light shift induced by the dressing laser, and $P_d^{(i)}$ denotes a projection onto the Rydberg state of the atom i. Regarding the coefficients, ξ_c in the order of several lattice spacing a. Also, the admixture parameter is very small $\beta \ll 1$ as a result of weak optical dressing.

Now, we are in a position to numerically investigate the performance of the proposed Rydberg VQS and discuss its ability to imitate unpredictable dynamics. As a proof of principle, we perform numerical simulations of a minimal version of the complex QCA with $N = 3$ sites on each ring. The small system size is due to the limitation of numerical simulation of the whole circuit. However, even a three-qubit QCA is capable of producing a triangular pattern as well as entangled states.

Finally, we present the corresponding numerical results in Fig. 7.4. In our simulation, the parameters are also chosen according to a relevant experiment reported in Ref. [184]. To be more precise, $\Delta/2\pi = 5.0$MHz and $\Omega/2\pi = 2.0$MHz. This corresponds to $\beta = 0.2$, $V_0/2\pi = 16.0$kHz and $\delta_{\mathrm{AC}}/2\pi = 200.0$kHz. Also, the microwave Rabi coupling is of the strength $\omega_{\mathrm{AC}}/2\pi = 10.0$kHz and we pick a proper value for C_6 such that $\xi_c = 2a$. Furthermore, the variational circuit is shallow with the circuit depth of three, $d = 3$, which is initialized with the previous optimized state. Regarding the measurement procedure, we assume that measuring Pauli operators up to 3-local operators per site, i.e. $4^3 = 64$ observables, is feasible.

In these calculations, we have employed a sequential quadratic programming algorithm [187] to optimize the variational cost function which is highly non-linear. Noteworthy, since in such problems the variational landscape sometimes becomes flat in a wide region, known as the *barren plateaus*, the *gradient-based* minimization methods might fail [188]. However, we circumvent this issue by optimizing the circuit in a layerwise fashion. We must mention that in a real experiment where the measurement results are unavoidably noisy, *derivative-free* minimization methods are more recommended as they don't get affected by the fake gradient descents induced by the measurement noise [51].

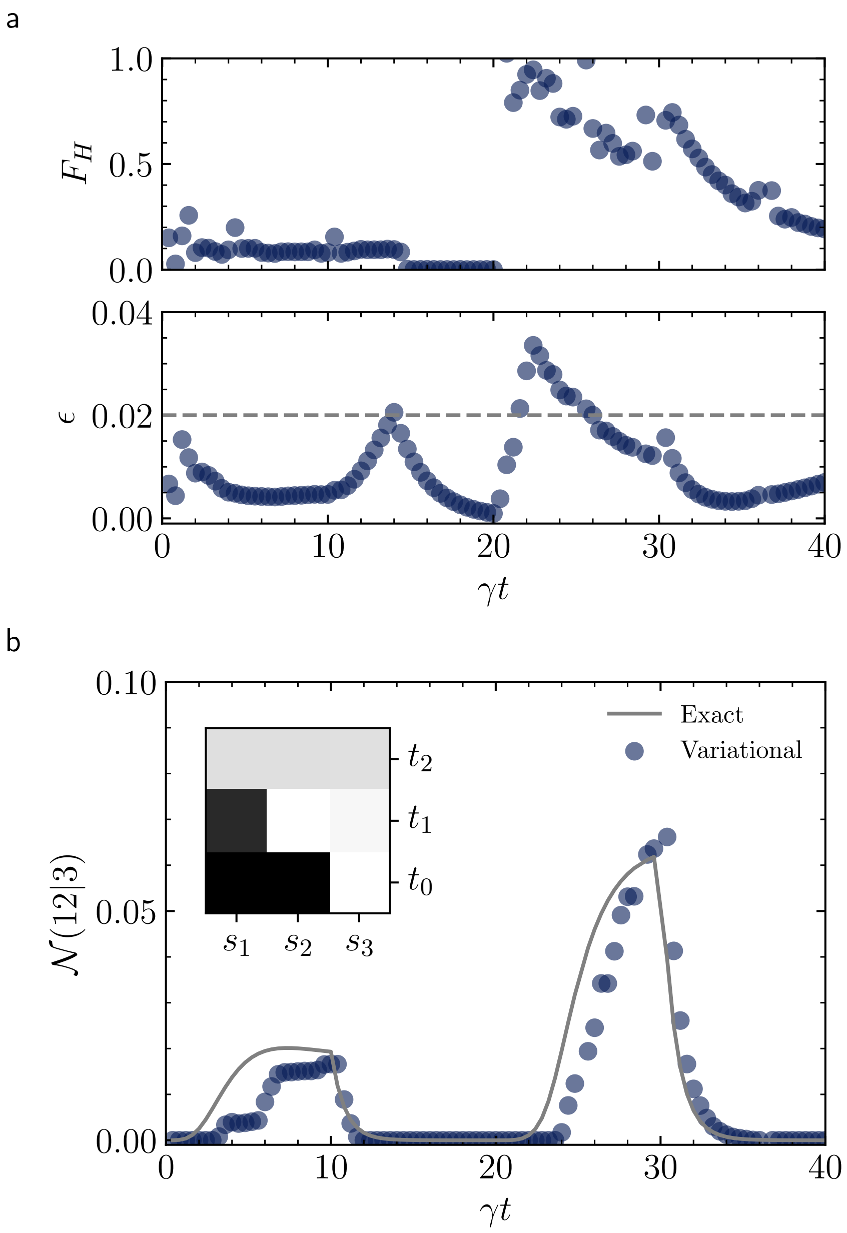

Figure 7.4: Benchmarking of the VQS approach for the quantum rule 137 for a system of $N = 3$ particles on each ring. Variational norm F_H, error probability ε (a) and quantum negativity $\mathcal{N}$ (b) as a function of time for the first two time steps with $n_\phi = 0.5$ and $\gamma t_c = 10$. The inset shows a minimal triangular tile appearing in the output ring at the middle of the steps.

Figure 7.4(a) demonstrates variational norm F_H and probability error for $n_\phi = 0.5$ and $\gamma t_c = 10$ where unpredictability and quantum entanglement coexist. The results indicate an overall error of less than 2% for almost all data points. Figure 7.4(b) shows that entanglement measured in terms of the negativity verifying good quantitative agreement between the VQS results and the exact dynamics.

To sum up, our numerical results demonstrate the expressibility of the variational quantum circuit for the experimental realization of arbitrary correlated operations using present-day qubit technologies. Notably, we showed that even unpredictable dynamical systems with 6-body correlated jump operators can be efficiently realized via the VQS scheme. Considering the severe challenges in the classical simulation of these systems [28], their quantum simulation with variational circuits opens up the possibility to observe a quantum advantage in the NISQ era.

Part IV

Conclusion

Imagination and intuition are vital to our understanding. ... Even physics, the strictest of all applied sciences, depends to an astonishing degree upon intuition, which works by way of the unconscious (although it is possible to demonstrate afterward the logical procedures that could have led one to the same result as intuition).

— Carl G. Jung

Chapter 8

Summary and outlook

8.1 Summary

In this thesis, we have reported on the numerical simulation of several types of open quantum systems under Markovian evolution. In Part I, we briefly reviewed the main features of open quantum systems and we outlined the relevant numerical simulation methods. We have particularly focused on variational methods which have shown promising results specifically for simulation of driven-dissipative systems. Building upon the recent advances in this direction, we have developed a novel variational treatment that provides a powerful framework especially for the detection of steady state phase transitions. We have also extended the variational quantum simulation scheme to a full-time simulator of open many-body systems suggesting a quantum advantage via available noisy quantum devices.

In Part II, we studied the properties of non-equilibrium steady states. Crucially, we investigated several challenging issues in this context. First, in Chapter 4, we have developed a variational method for assessing bistability in the steady state of open many-body systems. Our proposal relies on the notion of nucleation process among multiple minima appearing in a variational subspace of the fixed states of Linbladians. We note that our method applies to a wide range of dissipative many-body systems to verify any predicted multistability. In particular, we have demonstrated how the controversial bistability in the dissipative Ising model emerges only in proximity to phase transitions refuting any genuine bistability. Moreover, we have investigated a probabilistic cellular automaton featuring genuine bistability at the presence of both classical and quantum fluctuations. Second, in Chapter 5, we have tried to overcome the challenge of quantifying the stationary properties of strongly interacting dissipative spin models. We demonstrated a successful application of our variational approach by investigating driven-dissipative Rydberg gases with long-range van der Waals interactions. Importantly, the interplay between coherent driving and dissipation, namely the spontaneous emission and a dephasing process, clarified how a first-order phase transition appears.

In Part III of the thesis, we turned to dynamical properties of dissipative systems. Our work in Chapter 6 establishes an irreversible quantum cellular automata based on programmable jump operators leading to a novel dynamical class of open quantum many-body systems featuring unpredictable evolution. Strikingly, we have shown computational unpredictability can coexist with quantum entanglement for a long time, despite the intrinsic bias of entanglement toward predictable behavior. In Chapter 7, we numerically simulated dissipative variational circuits and demonstrated that they can be deployed to emulate non-trivial dissipative dynamics with high fidelity. Notably, we suggested a protocol for constructing variational circuits for multi-dimensional systems based upon the notion of Rydberg dressing which is perfectly compatible with the present-day Rydberg technology.

8.2 Outlook

At the final section of this thesis, we outline possible directions for future studies corresponding to the content of chapters 4,5,6 and 7.

- **Multistability in non-equilibrium steady states:** The master equation embedding of Toom-like behavior opens up the possibility to elaborate on non-ergodicity in the context of driven-dissipative quantum systems. Geared up with the variational Langevin formalism, one can also classify probabilistic cellular automata in terms of their steady-state stability. This can in turn give rise to novel models with multistable steady states, initiating concrete applications in various quantum technologies such as self-correcting quantum memories [189, 190, 191].

- **Criticality in strongly interacting dissipative systems:** Considering the success of the variational principle for the steady state of strongly interacting Rydberg gases, it would be interesting to further study the appearance of dissipative phase transition in the presence of long-range interactions and different dissipation sources. Particularly, investigation of criticality under the aforementioned scenario is a very exciting subject of research, as there are many open questions to be answered. A variant of the dissipative Ising model is a good candidate in this regard as its steady-state phase diagram exhibits multi-critical behavior in contrast to its equilibrium counterpart [99].

- **Unpredictability in quantum cellular automata:** While our proposed QCA is spatially (quasi-)one-dimensional, the setting has the advantage of easily be extended to higher dimensions by adding additional rings. It would be interesting, for instance, to construct a dissipative analog of the quantum game of life [140] attaining a higher level of unpredictability in quantum dynamical systems. Moreover, we expect that the additional rings can also be useful for embedding historic memory which permits to access non-Markovian dynamics in a controlled way.

- **Data analysis using variational quantum circuits:** Building upon the flexibility of VQS scheme, it would be interesting to design hardware-efficient platforms for computational purposes as well. Particularly, within the active field of quantum machine learning, it would be useful to further investigate the experimental realization of relevant setups such as quantum neural networks for quantum/classical data classification [192, 193], quantum autoencoders to handle noisy data [194], etc.

Part V

Appendices

Quantum mechanics can be appreciated, to some degree, on a purely qualitative level. But mathematics is what brings its beauty into sharp focus.

— Leonard Susskind

Appendix A

Microscopic derivation of Lindblad equation

Here we will discuss, in more detail, the required conditions for the derivation of the Lindblad master equation (2.13). In the following, we will focus on a limiting case where the system-environment interaction is weak, also known as the *weak-coupling limit.* This limit arises naturally in many practical situations where the environment is extremely large compared to the system size, and also the system of interest is, to some extent, isolated. It is worth mentioning that the weak-coupling limit is only a sufficient condition for quantum Markovianity. Other cases are discussed in, e.g. Refs.[16, 19].

A.1 Born-Markov approximation

Let us start from the von Neumann equation of a system S and its environment E as a whole, i.e. Eq. (2.10) where the total Hamiltonian is

$$H_{\mathrm{SE}} = H_{\mathrm{S}} + H_{\mathrm{E}} + H_{\mathrm{int}}. \tag{A.1}$$

In order to employ a perturbative treatment, it is helpful to go to the interaction picture such that

$$\frac{d}{dt}\tilde{\rho}_{\mathrm{SE}}(t) = -i[\tilde{H}_{\mathrm{int}}(t), \tilde{\rho}_{\mathrm{SE}}(t)], \tag{A.2}$$

with

$$\tilde{O} = e^{i(H_{\mathrm{S}}+H_{\mathrm{E}})t} O e^{-i(H_{\mathrm{S}}+H_{\mathrm{E}})t}.$$

After integrating the Eq. (A.2) and inserting it back to the same equation, one can obtain the following relation

$$\frac{d}{dt}\tilde{\rho}_{\mathrm{SE}}(t) = -i[\tilde{H}_{\mathrm{int}}(t), \tilde{\rho}_{\mathrm{SE}}(0)] - \int_0^t d\tau \big[\tilde{H}_{\mathrm{int}}(t), [\tilde{H}_{\mathrm{int}}(\tau), \tilde{\rho}_{\mathrm{SE}}(\tau)]\big].$$

Now, tracing out the environment gives

$$\frac{d}{dt}\tilde{\rho}_{\mathrm{S}}(t) = -\mathrm{Tr}_{\mathrm{E}}\left(\int_0^t d\tau \big[\tilde{H}_{\mathrm{int}}(t), [\tilde{H}_{\mathrm{int}}(\tau), \tilde{\rho}_{\mathrm{S}}(t) \otimes \tilde{\rho}_{\mathrm{E}}]\big]\right), \tag{A.3}$$

where we here assumed that not only the system and environment are initially uncorrelated, i.e. $\tilde{\rho}_{\mathrm{SE}}(0) = \tilde{\rho}_{\mathrm{S}}(0) \otimes \tilde{\rho}_{\mathrm{E}}$, but also the total state has the form of $\tilde{\rho}_{\mathrm{SE}}(\tau) = \tilde{\rho}_{\mathrm{S}}(t) \otimes \tilde{\rho}_{\mathrm{E}}(0)$. The latter assumption is twofold. First, building upon the weak-coupling limit we have applied the so-called *Born approximation* by replacing the total state by a product state that is

$$\tilde{\rho}_{\mathrm{SE}}(\tau) = \tilde{\rho}_{\mathrm{S}}(\tau) \otimes \tilde{\rho}_{\mathrm{E}}(t).$$

Secondly, we employ the following approximation, known as the *Markov approximation*,

$$\tilde{\rho}_{\mathrm{S}}(\tau) \otimes \tilde{\rho}_{\mathrm{E}}(t) \to \tilde{\rho}_{\mathrm{S}}(t) \otimes \tilde{\rho}_{\mathrm{E}},$$

which implies that the memory inherited in Eq. (A.3) (as $\tilde{\rho}_{\mathrm{S}}(t)$ depends on all the previous states) is neglectable as long as the correlation time of the environment is relatively small (short-memory environment). Next, using the substitution $\tau \to t - \tau$ and extending the integration in Eq. (A.3) to infinity, we get

$$\frac{d}{dt}\tilde{\rho}_{\mathrm{S}}(t) = -\mathrm{Tr}_{\mathrm{E}}\left(\int_0^\infty d\tau \big[\tilde{H}_{\mathrm{int}}(t), [\tilde{H}_{\mathrm{int}}(t-\tau), \tilde{\rho}_{\mathrm{S}}(t) \otimes \tilde{\rho}_{\mathrm{E}}]\big]\right). \tag{A.4}$$

The above relation demonstrates a time-local equation featuring a fully Markovian generator.

A.2 Secular approximation

Having said that, reaching the Lindblad form of the master equation requires further considerations. To this end, let us decompose the interaction

Hamiltonian $\tilde{H}_{\text{int}}$ as follows

$$\begin{aligned}\tilde{H}_{\text{int}} &= \sum_{n} \tilde{S}_n(t) \otimes \tilde{E}_n(t) \\ &= \sum_{n,\omega} e^{-i\omega t} S_n(\omega) \otimes \tilde{E}_n(t),\end{aligned}$$

where $\tilde{S}_n(t) = \sum_\omega e^{-i\omega t} S_n(\omega)$ denotes an expansion in terms of the eigenfrequencies of the system Hamiltonian. Inserting the decomposition back into Eq. (A.4) yields

$$\frac{d}{dt}\tilde{\rho}_{\text{S}}(t) = \sum_{m,n}\sum_{\omega,\omega'} e^{i(\omega'-\omega)t} g_{mn}(\omega)\left[S_n(\omega)\tilde{\rho}_{\text{S}}(t), S_m^\dagger(\omega')\right] + \text{h.c.}, \tag{A.5}$$

with

$$\begin{aligned}g_{mn}(\omega) &= \int_0^\infty d\tau \operatorname{Tr}\left(e^{i\omega\tau}\tilde{E}_n(t)\tilde{E}_n(t-\tau)\tilde{\rho}_{\text{E}}\right) \\ &= \frac{1}{2}\gamma_{mn}(\omega) + \chi_{mn}(\omega),\end{aligned} \tag{A.6}$$

being the correlation function of the environment decomposed into Hermitian and non-Hermitian terms. In the weak-coupling limit, we are allowed to neglect the fast-rotating terms in the Eq. (A.5) and only keep the resonant interactions, i.e. $\omega' = \omega$. The so-called *secular approximation* is equivalent to the rotating-wave approximation widely used in quantum optics. Eventually, utilizing these quantities and going back to the Schrödinger picture yields the Lindblad generator of the Markovian dynamics,

$$\begin{aligned}\mathcal{L}(\rho_{\text{S}}(t)) = &- i[H_{\text{S}} + H'_{\text{S}}, \rho_{\text{S}}(t)] \\ &+ \sum_{m,n}\sum_{\omega}\gamma_{mn}(\omega)\left(S_n(\omega)\rho_{\text{S}}(t)S_m^\dagger(\omega) - \frac{1}{2}\left\{S_m^\dagger(\omega)S_n(\omega), \rho_{\text{S}}(t)\right\}\right),\end{aligned} \tag{A.7}$$

where

$$H'_{\text{S}} = -\sum_{m,n}\sum_{\omega}\chi_{mn}(\omega)S_n(\omega)S_m^\dagger(\omega).$$

The additional Hamiltonian H'_{S} commutes with H_{S} and hence making only a total shift in the energy levels of the system. A comprehensive derivation of the Lindblad master equation is available in Refs. [20, 16].

Appendix B

Characterization of Toom-like bistability

Toom-like bistability enforces inhomogeneity in the time-dependent states as it is necessary to recover multiple (homogeneous) steady states via denucleation of minority islands in the initial states. Here we investigate the required inhomogeneity by incorporating spatial fluctuations into the Gutzwiller ansatz. This allows us to obtain a simple non-equilibrium variant of the time-dependent Ginzburg-Landau equations in the form of a Langevin equation which captures the mesoscopic behavior of the model near criticality.

B.1 Ginzburg-Landau variational functional

We start by formulating a Ginzburg-Landau-like functional from the variational norm within the Gutzwiller theory for open systems. We consider the functional as a discrete sum over lattice sites including the homogeneous variational norm f_v as well as an inhomogeneous term g_v to incorporates spatial fluctuations, i.e.

$$\mathbb{F}[\phi] = \sum_i f_v(\phi_i) + g_v(\nabla\phi_i), \tag{B.1}$$

where g_v is constructed by the overlapping terms of the Liouvillian (see Fig. B.1) such that $g_v(\nabla\phi_i \to 0) = 0$, hence

$$g_v(\nabla\phi_i) = \sum_j \frac{\langle\!\langle \tilde{\mathcal{L}}_i^\dagger(\phi_i, \nabla\phi_i) | \tilde{\mathcal{L}}_j(\phi_i, \nabla\phi_i) \rangle\!\rangle - \langle\!\langle \tilde{\mathcal{L}}_i^\dagger(\phi_i) | \tilde{\mathcal{L}}_j(\phi_i) \rangle\!\rangle}{\langle\!\langle \rho_0(\phi_i) | \rho_0(\phi_i) \rangle\!\rangle^{n_{ij}}}, \tag{B.2}$$

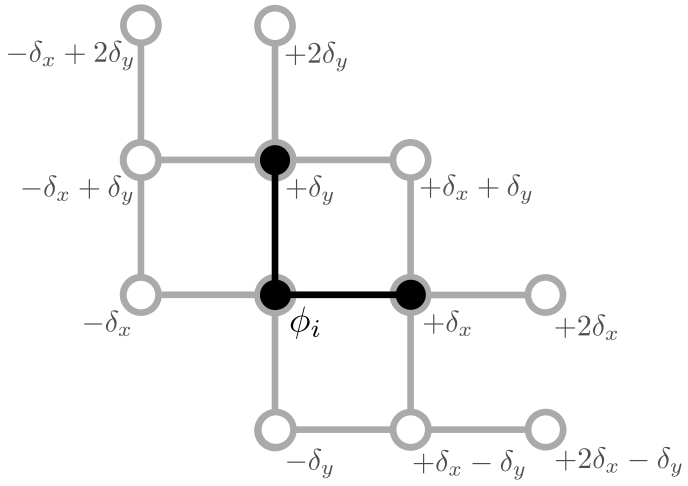

Figure B.1: Spatial gradients corresponding to Toom's model. Here, the black L shape represents $\langle\!\langle \tilde{\mathcal{L}}_i^\dagger |$ and the gray L shapes represent $|\tilde{\mathcal{L}}_j\rangle\!\rangle$ as a function of ϕ_i and its spatial gradients δ_x and δ_y.

with j running over the given site itself, say site i, and all the neighbouring sites whose associated terms in the Liouvillian overlaps with that of the site i. In fact, we express g_v in terms of the localized field ϕ_i and spatial fluctuations around it, i.e. $\nabla\phi_i = \delta_x\hat{x} + \delta_y\hat{y}$, with

$$\begin{aligned} \delta_x &= \big(\phi_{i+E} - \phi_i\big) = -\big(\phi_{i+W} - \phi_i\big) \\ \delta_y &= \big(\phi_{i+N} - \phi_i\big) = -\big(\phi_{i+S} - \phi_i\big). \end{aligned} \tag{B.3}$$

where the capital letters indicate cardinal neighbours. Now, performing a Taylor expansion of $g_v(\phi_i)$ around $\phi_i = 0$ up to the second order yields

$$g_v = \frac{a}{2}\big[\delta_x + \delta_y\big] + b\delta_x\delta_y + b'\phi_i\big[\delta_x + \delta_y\big] + c\big[\delta_x^2 + \delta_y^2\big]. \tag{B.4}$$

These coefficients will be then calculated to construct the Langevin equation.

B.2 Domain-wall kinetics in Toom's model

Bistability in Toom's model is caused by the chiral updating rules enabling a majority phase to eliminate the minority phase. This can be simply explained in terms of surface-energy dependency on the orientation of the underlying domain walls separating the two phases. Suppose we have a minority island (of either $|\uparrow\rangle$ or $|\downarrow\rangle$ states) in the form of an isosceles right triangle. As seen in Fig. B.2(a), one can estimate local surface tension σ_θ -with θ denoting the interface orientation- in terms of the corresponding 3-site variational norm. More precisely, we define σ_θ as the "energy" difference between the north-center-east state at the current time and after a spin-flip operation on the central site (similar to the form of updating rules). For the noiseless updates, i.e. $\mu = \nu = 0$, while the surface tension on the hypotenuse is positive, that is $\sigma_{45^\circ} = \mathbb{F}_{|\downarrow\uparrow\downarrow\rangle}$, the surface tension of the vertical and horizontal interfaces vanish. Since the system tends to lower the surface tension, the hypotenuse moves toward the southwestern direction while the legs stay motionless. Eventually, this wipes out the minority island of either phase giving rise to the expected bistability.

The above argument holds even in the case of having sufficiently small noise where $\sigma_{45^\circ} > \sigma_{0^\circ} + \sigma_{90^\circ}$. In other words, the domain-wall kinetics can be effectively described as

$$\frac{\partial R}{\partial t} \propto -\left(\sigma_{45^\circ} - \sigma_{0^\circ} - \sigma_{90^\circ}\right), \tag{B.5}$$

where R denotes the radius of a fictitious circular droplet inscribed in the triangular island. Crucially, if the r.h.s of the equation is negative, the droplet constantly shrinks irrespective of its size. In Fig. B.2(b), we illustrate the shrinkage process by solving the Langevin equation for a lattice of 20×20 sites using the Euler-Maruyama method [195]. As the initial state in the simulation, we consider a square-shaped minority island with a length of 10 whose state is favored by the bias and the bulk being in the unfavored state. We observe that in the case of zero white noise, the square-shaped island gradually turns into a triangle, and then the aforementioned shrinkage takes place. It is worth mentioning that according to the variational calculations, the white noise is very small in the bistable region. Therefore, the overall dynamics is roughly consistent with the mentioned geometrical argument.

Concerning the numerical estimation of the phase diagram, we thereupon considered a minority island in the form of an isosceles right triangle with the length of 10 sites sitting in the middle of a 20×20 lattice with periodic boundary condition. Next, we solved the Langevin equation by averaging over 100 samples. Finally, to assess the steady state we have calculated the averaged value of the order parameter $\langle \phi \rangle$ in the long-time limit of the dynamics.

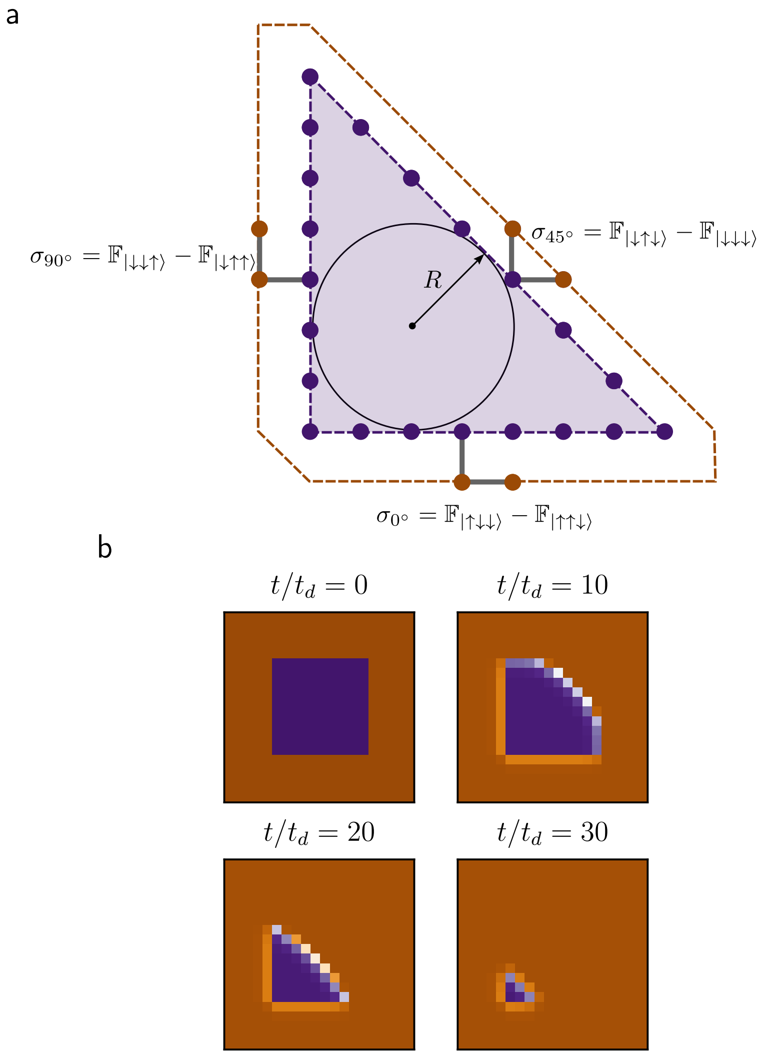
a
$\sigma_{90^\circ} = \mathbb{F}_{|\downarrow\downarrow\uparrow\rangle} - \mathbb{F}_{|\downarrow\uparrow\uparrow\rangle}$
$\sigma_{45^\circ} = \mathbb{F}_{|\downarrow\uparrow\downarrow\rangle} - \mathbb{F}_{|\downarrow\downarrow\downarrow\rangle}$
R
$\sigma_{0^\circ} = \mathbb{F}_{|\uparrow\downarrow\downarrow\rangle} - \mathbb{F}_{|\uparrow\uparrow\downarrow\rangle}$
b
$t/t_d = 0$
$t/t_d = 10$
$t/t_d = 20$
$t/t_d = 30$

Figure B.2: (a) Orientational surface tension on a triangular minority island circumscribing a droplet of radius R. (b) Time evolution of a 10×10 minority island of the stable state encircled by the less-stable state on 20×20 square lattice with $T = 0.75$, $H = 0.001$, and zero white noise.

Appendix C

Correlated jump operators in Rydberg atoms

C.1 Adiabatic elimination

In the context of open quantum systems, while studying the full system-environment is usually impossible, an effective description of the system itself is feasible in specific cases such as the weak-coupling limit of the system-environment interaction. Similarly, given a quantum system with several interacting subsystems, one might be only interested in obtaining the dynamics of a particular subsystem of interest. This is possible if the subsystem of interest is weakly coupled to the other subsystems and has relatively lower dissipation rates. The so-called *adiabatic elimination* is highly useful to engineer many-body interactions. Building upon this technique, we are interested in tailoring 3-body correlated jump operators. In the following, we exemplify that using 3-level Rydberg atoms under proper conditions.

C.2 Tailoring correlated jump operators

We assume that we have three Rydberg atoms with three levels for each, $\{|g_i\rangle, |p_i\rangle, |r_i\rangle\}$. Here is the corresponding Hamiltonian

$$H_{\text{Ryd}} = \omega_{\text{aux}} \sum_{i=1}^{3} |p_i\rangle\langle r_i| + \text{H.c.} + \omega_p \sum_{i=1}^{3} |p_i\rangle\langle p_i| + V_{rr} \sum_{\langle ij\rangle} |r_i r_j\rangle\langle r_i r_j|, \tag{C.1}$$

since we are interested in the open boundary condition there is no interaction between site 1 and site 3, i.e. $\langle ij\rangle \in \{12, 23\}$. We also consider a spontaneously decay from the intermediate state $|p_i\rangle$ to the ground state $|g_i\rangle$, i.e.

$$c_i = \sqrt{\gamma}|g_i\rangle\langle p_i|, \tag{C.2}$$

where γ denotes the decay rate. Now, in order to proceed with the adiabatic elimination of $\{|p_i\rangle\}$, we divide the Hilbert space of our model into a ground-state subspace $\mathcal{H}_{gr}$, and an excited-state subspace $\mathcal{H}_e$. Accordingly, one can decompose the Hamiltonian as follows

$$\begin{aligned} H_{\mathrm{Ryd}} &= (P_{gr} + P_e)H_{\mathrm{Ryd}}(P_{gr} + P_e) \\ &= P_{gr}H_{\mathrm{Ryd}}P_{gr} + P_eH_{\mathrm{Ryd}}P_e + P_eH_{\mathrm{Ryd}}P_{gr} + P_{gr}H_{\mathrm{Ryd}}P_e, \\ &\equiv H_{gr} + H_e + V_+ + V_-, \end{aligned} \tag{C.3}$$

where $V = V_+ + V_-$ couples the subspaces and the projection operator $P_{gr} = \mathbb{1} - P_e$ is defined as $P_{gr} = \mathbb{1}^{(1)}_{gr} \otimes \mathbb{1}^{(2)}_{gr} \otimes \mathbb{1}^{(3)}_{gr}$ with $\mathbb{1}^{(i)}_{gr} \equiv |g_i\rangle\langle g_i| + |r_i\rangle\langle r_i|$. The next step is to to diagonalize the ground-state Hamiltonian H_{gr} in the form of $H_{gr} = \sum_l E_l P_l$ yielding

$$\begin{aligned} P_0 &= |ggg\rangle\langle ggg|, & E_0 &= 0, \\ P_1 &= |rgg\rangle\langle rgg|, & E_1 &= 0, \\ P_2 &= |grg\rangle\langle grg|, & E_2 &= 0, \\ P_3 &= |ggr\rangle\langle ggr|, & E_3 &= 0, \\ P_4 &= |rgr\rangle\langle rgr|, & E_4 &= 0, \\ P_5 &= |rrg\rangle\langle rrg|, & E_5 &= V_{rr}, \\ P_6 &= |grr\rangle\langle grr|, & E_6 &= V_{rr}, \\ P_7 &= |rrr\rangle\langle rrr|, & E_7 &= 2V_{rr}. \end{aligned}$$

Let us to express V_+ in terms of the basis P_l such that $V_+ \equiv \sum_l V_+^l \equiv \sum_l V_+ P_l$ where

$$\begin{aligned} V_+^0 &= 0, \\ V_+^1 &= \omega_{\mathrm{aux}}|pgg\rangle\langle rgg|, \\ V_+^2 &= \omega_{\mathrm{aux}}|gpg\rangle\langle grg|, \\ V_+^3 &= \omega_{\mathrm{aux}}|ggp\rangle\langle ggr|, \\ V_+^4 &= \omega_{\mathrm{aux}}\big(|pgr\rangle + |rgp\rangle\big)\langle rgr|, \\ V_+^5 &= \omega_{\mathrm{aux}}\big(|prg\rangle + |rpg\rangle\big)\langle rrg|, \\ V_+^6 &= \omega_{\mathrm{aux}}\big(|gpr\rangle + |grp\rangle\big)\langle grr|, \\ V_+^7 &= \omega_{\mathrm{aux}}\big(|prr\rangle + |rpr\rangle + |rrp\rangle\big)\langle rrr|. \end{aligned}$$

Following the procedure in Ref. [196], one can obtain an effective Hamiltonian and effective jump operators as follows

$$H_{\text{eff}} = -\frac{1}{2}V_{-}\sum_{l}\Big[(O^{l}_{\text{NH}})^{-1} + \big((O^{l}_{\text{NH}})^{-1}\big)^{\dagger}\Big]V^{l}_{+} + H_{gr}, \tag{C.4}$$

$$c^{(m)}_{\text{eff}} = c_{m}\sum_{l}(O^{(l)}_{\text{NH}})^{-1}V^{l}_{+}, \tag{C.5}$$

where $O^{(l)}_{\text{NH}}$ is a non-Hermitian operator which is defined as

$$\begin{aligned} O^{(l)}_{\text{NH}} =& H_{e} - i/2\sum_{k} c_{k}c^{\dagger}_{k} - E_{l} \\ O^{(l)}_{\text{NH}} =& \sum_{m=1}^{3}\big(\omega_{p} - E_{l} - i\frac{\gamma}{2}\big)|p_{m}\rangle\langle p_{m}| \otimes \mathbb{1}_{gr} \otimes \mathbb{1}_{gr} \\ &+ V_{rr}|prr\rangle\langle prr| + V_{rr}|rrp\rangle\langle rrp|. \end{aligned}$$

The effective process consists of an initial excitation V^{l}_{+} from ground state l, an intermediate propagation O_{NH} in the excited subspace, and eventually either a de-excitation V_{-} to the ground state subspace corresponding to the effective Hamiltonian, or a decay c_{k} to $|g_{m}\rangle$ representing the effective jump operators.

In or case, the effective Hamiltonian takes the following form

$$\begin{aligned} H_{\text{eff}} =& V_{rr}\sum_{<ij>}|r_{i}r_{j}\rangle\langle r_{i}r_{j}| \otimes \mathbb{1}_{gr} \\ & - \omega^{2}_{\text{aux}}|r_{m}\rangle\langle p_{m}|\sum_{m}\frac{\Big[\omega_{p} + \big(\tilde{\delta}_{|f\rangle} - \tilde{\delta}'_{\langle i|}\big)V_{rr}\Big]}{\Big[\omega_{p} + \big(\tilde{\delta}_{|f\rangle} - \tilde{\delta}'_{\langle i|}\big)V_{rr}\Big]^{2} + \gamma^{2}/4}\big(|p_{m}\rangle\langle r_{m}| \otimes \mathbb{1}_{gr} \otimes \mathbb{1}_{gr}\big), \end{aligned}$$

where

$$\tilde{\delta}_{|f\rangle} = \begin{cases} 1 & \text{if} \quad |f\rangle \in \{|prr\rangle, |rrp\rangle\}, \\ 0 & \text{otherwise,} \end{cases}$$

and

$$\tilde{\delta}'_{\langle i|} = \begin{cases} 2 & \text{if} \quad \langle i| = \langle rrr|, \\ 1 & \text{if} \quad \langle i| \in \{\langle grr|, \langle rrg|\}, \\ 0 & \text{otherwise.} \end{cases}$$

Also, the effective jump operators can be written as

$$c^{(m)}_{\text{eff}} = |g_{m}\rangle\langle p_{m}|\frac{\omega_{\text{aux}}\sqrt{\gamma}}{\omega_{p} + \big(\tilde{\delta}_{|f\rangle} - \tilde{\delta}'_{\langle i|}\big)V_{rr} - i\gamma/2}\big(|p_{m}\rangle\langle r_{m}| \otimes \mathbb{1}_{gr} \otimes \mathbb{1}_{gr}\big), \tag{C.6}$$

which represents the following effective jump operators

$$\begin{aligned}
c^1_{\text{eff}} &= \omega_{\text{aux}}\sqrt{\gamma}\big[\lambda_1|ggg\rangle\langle rgg| + \lambda_1|ggr\rangle\langle rgr| + \lambda_2|grg\rangle\langle rrg| + \lambda_2|grr\rangle\langle rrr|\big],\\
c^2_{\text{eff}} &= \omega_{\text{aux}}\sqrt{\gamma}\big[\lambda_1|ggg\rangle\langle grg| + \lambda_2|rgg\rangle\langle rrg| + \lambda_2|ggr\rangle\langle grr| + \lambda_3|rgr\rangle\langle rrr|\big],\\
c^3_{\text{eff}} &= \omega_{\text{aux}}\sqrt{\gamma}\big[\lambda_1|ggg\rangle\langle ggr| + \lambda_1|rgg\rangle\langle rgr| + \lambda_2|grg\rangle\langle grr| + \lambda_2|rrg\rangle\langle rrr|\big],
\end{aligned}$$

where

$$\begin{aligned}
\lambda_1 &= (\omega_p - i\gamma/2)^{-1},\\
\lambda_2 &= (\omega_p - V_{rr} - i\gamma/2)^{-1},\\
\lambda_3 &= (\omega_p - 2V_{rr} - i\gamma/2)^{-1}.
\end{aligned}$$

To further simplify the effective operators, we assume a strong Rydberg-Rydberg interaction, i.e. $V_{rr} \gg 1$, and a resonance condition of $\omega_p = 2V_{rr}$. Consequently, the three jump operators are reduced to a single operator, i.e.

$$\begin{aligned}
c^1_{\text{eff}} &= 0,\\
c^2_{\text{eff}} &= i2\omega_{\text{aux}}/\sqrt{\gamma}|rgr\rangle\langle rrr|,\\
c^3_{\text{eff}} &= 0.
\end{aligned}$$

Finally, we can describe the original 3-level Rydberg atoms in terms of 2-level atoms with the following effective Hamiltonian and effective jump operator

$$H_{\text{eff}} = H_{gr} = V_{rr}\sum_{<ij>} P_r^{(i)}P_r^{(j)}, \tag{C.7}$$

$$c_{\text{eff}} = i\frac{2\omega_{\text{aux}}}{\sqrt{\gamma}}P_r^{(1)}\sigma_-^{(2)}P_r^{(3)}. \tag{C.8}$$

The complex coefficient corresponds to an effective decay rate that is given by

$$\gamma_{\text{eff}} = |\langle rgr|c_{\text{eff}}|rrr\rangle|^2 = \frac{4\omega_{\text{aux}}^2}{\gamma}. \tag{C.9}$$

Therefore, we demonstrated a successful engineering of a typical correlated jump operators using the technique of adiabatic elimination. More advanced protocols can be found in Refs. [174, 117].

Appendix D

Frozen Rydberg gases and the Ising model

In this section, we analyze the structure of the Rydberg Hamiltonian including long-range vdW interactions by converting it into Ising-type interaction. Moreover, we will show that the resulting characteristic values of the laser detuning don't change the expected liquid-gas phase transition.

D.1 Rydberg vs. Ising Hamiltonian

Rydberg Hamiltonian resembles the transverse-field Ising Hamiltonian with long-range interactions, i.e.

$$H_{\text{Ising}} = \frac{\Omega}{2} \sum_i \sigma_x^{(i)} + V \sum_{i<j} \frac{\sigma_z^{(i)} \sigma_z^{(j)}}{|\mathbf{r}_i - \mathbf{r}_j|^6}, \tag{D.1}$$

being a more well-known model. However, there are two differences between these two Hamiltonians. First, the Ising interaction $\sigma_z^{(i)} \sigma_z^{(j)}$ does not exclude ground state interactions as the Rydberg-Rydberg interaction does. Second, the Rydberg Hamiltonian contains additional terms proportional to $\sigma_z^{(i)}$ which corresponds to a longitudinal magnetic field in the spin language.

However, by expanding Rydberg interactions in terms of σ_z, one can obtain Ising interactions and cancel out the longitudinal field by an effective detuning. Having said that, reducing Rydberg interactions to Ising ones may kill the particular properties of Rydberg gases such as the blockade effect. Therefore, the trick is to keep the Rydberg form of the Hamiltonian within a length greater than blockade radius, $r_c > r_{\text{b}}$, and apply the reduction to

Ising model for larger values of the so-called *cutoff radius* r_c as follows

$$\begin{aligned} H_{\mathrm{Ryd}} = &-\frac{\Delta}{2}\sum_i \sigma_z^{(i)} + \frac{\Omega}{2}\sum_i \sigma_x^{(i)} + \frac{C_6}{a^6}\sum_{r_{ij}\le r_c} \frac{P_r^{(i)}P_r^{(j)}}{r_{ij}^6} \\ &+ \frac{C_6}{4a^6}\sum_{r_{ij}>r_c} \frac{\sigma_z^{(i)}+\sigma_z^{(j)}}{r_{ij}^6} + \frac{C_6}{4a^6}\sum_{r_{ij}>r_c} \frac{\sigma_z^{(i)}\sigma_z^{(j)}}{r_{ij}^6} + \frac{C_6}{4a^6}\sum_{r_{ij}>r_c} \frac{\mathbb{1}^{(i)}\mathbb{1}^{(j)}}{r_{ij}^6}, \end{aligned} \tag{D.2}$$

where $r_{ij} = |\mathbf{r}_i - \mathbf{r}_j|$. Since the last term only shifts the total energy of the system, we can ignore it. Hence, we have

$$\begin{aligned} H_{\mathrm{Trans}} = &\Big(-\frac{\Delta}{2} + \tilde{V}_{\mathrm{Ising}}\Big)\sum_i \sigma_z^{(i)} + \frac{\Omega}{2}\sum_i \sigma_x^{(i)} \\ &+ \frac{C_6}{a^6}\sum_{r_{ij}\le r_c} \frac{P_r^{(i)}P_r^{(j)}}{r_{ij}^6} + \frac{C_6}{4a^6}\sum_{r_{ij}>r_c} \frac{\sigma_z^{(i)}\sigma_z^{(j)}}{r_{ij}^6}, \end{aligned} \tag{D.3}$$

where

$$\tilde{V}_{\mathrm{Ising}} = \frac{C_6}{4a^6}\sum_{r_{ij}>r_c} \frac{1}{r_{ij}^6}. \tag{D.4}$$

As mentioned before, we can cancel out the longitudinal field by an appropriate choice of the detuning, i.e., $\Delta(r_c) = 2\tilde{V}_{\mathrm{Ising}}(r_c)$. Crucially, at the extreme case of $r_c = 0$, the resulting value of detuning $\Delta(r_c = 0)$ is very large such that it compensates for the energy shift by the strong vdW interaction, leading to the anti-blockade regime. However, we are interested in the regime of finite r_c where the blockade effect is under control. From now on, we call to these values of detuning as *transverse points*. To obtain these points, let us first calculate the value of $\tilde{V}_{\mathrm{Ising}}$, ie.e

$$\tilde{V}_{\mathrm{Ising}} = \frac{C_6}{4a^6}\left[\sum_{r_{ij}=-\infty}^{+\infty}{}' \frac{1}{r_{ij}^6} - \sum_{r_{ij}\le r_c} \frac{1}{r_{ij}^6}\right], \tag{D.5}$$

where the primed sum indicates that the zero point is excluded. Using the notion of Dirichlet series, the first term of the above equation describing distances on a square lattice, is equivalent to

$$\begin{aligned} \sum_{-\infty}^{+\infty}{}' \frac{1}{r_{ij}^6} &= \sum_{-\infty}^{+\infty}{}' \frac{1}{(i^2+j^2)^3} \\ &= 4\zeta(3)\beta(3), \end{aligned} \tag{D.6}$$

where $\beta(x)$ is the Dirichlet β-function and $\zeta(x)$ is the Riemann ζ-function

r_c	$\tilde{V}_{\text{Ising}} a^6/C_6$	Δ
0	$\zeta(3)\beta(3)$	2055.0144
1	$\zeta(3)\beta(3) - (1)$	290.6422
$\sqrt{2}$	$\zeta(3)\beta(3) - \left(1 + \frac{1}{8}\right)$	70.0957
2	$\zeta(3)\beta(3) - \left(1 + \frac{1}{8} + \frac{1}{64}\right)$	42.5274
$\sqrt{5}$	$\zeta(3)\beta(3) - \left(1 + \frac{1}{8} + \frac{1}{64} + \frac{2}{125}\right)$	14.2974
$\sqrt{8}$	$\zeta(3)\beta(3) - \left(1 + \frac{1}{8} + \frac{1}{64} + \frac{2}{125} + \frac{1}{512}\right)$	10.8514
3	$\zeta(3)\beta(3) - \left(1 + \frac{1}{8} + \frac{1}{64} + \frac{2}{125} + \frac{1}{512} + \frac{1}{729}\right)$	8.4311

Table D.1: Transverse points of the laser detuning in the Rydberg Hamiltonian for $C_6 = 20\text{MHz}\mu\text{m}^6$ and $a = 0.532\mu\text{m}$.

[197]. We recall that $\beta(3) = \pi^3/32$ and $\zeta(3) \approx 1.202057$ is the sum of the reciprocals of the positive cubes which is known as the Apery's constant. Therefore, we can express Eq. (D.5) as follows

$$\tilde{V}_{\text{Ising}} = \frac{C_6}{a^6}\left[\zeta(3)\beta(3) - \sum_{r_{ij} \le r_c} \frac{f(i,j)}{r_{ij}^6}\right], \tag{D.7}$$

where

$$f(i,j) = \begin{cases} 2 & \text{if } i \neq 0 \text{ and } i \neq j, \\ 1 & \text{otherwise.} \end{cases}$$

In Table D.1, we present the transverse points of the laser detuning for $0 < r_t < 3$ and the vdW coefficient of $C_6/a^6 = 882\text{MHz}$.

To further proceed, it is possible to have an effective low-energy description of the aforementioned model with H_{Trans} and the associated cutoff radius r_c. A short-range Ising model can be served as the effective model with the following Hamiltonian,

$$H_{\text{eff}} = h_z(r_c)\sum_i \sigma_z^{(i)} + \frac{\Omega}{2}\sum_i \sigma_x^{(i)} + J_{\text{eff}}(r_c)\sum_{\langle ij\rangle} \sigma_z^{(i)}\sigma_z^{(j)}, \tag{D.8}$$

with $h_z(r_c) = -\Delta/2 + \tilde{V}_{\text{Ising}}$ and $J_{\text{eff}}(r_c) = \tilde{V}_{\text{Ising}}$. Now, considering two consec-

r_{c_1}	r_{c_2}	Δ^*
0	1	509.2595
1	$\sqrt{2}$	112.9505
$\sqrt{2}$	2	52.9374
2	$\sqrt{5}$	21.4002
$\sqrt{5}$	$\sqrt{8}$	12.3383
$\sqrt{8}$	3	9.4893

Table D.2: Midpoints of the laser detuning in the Rydberg Hamiltonian for the same value of C_6 as in Table D.1.

utive cutoff radii, say r_{c_1} and r_{c_2}, we want to find a specific value of detuning $\Delta_{r_{c_1}} < \Delta^* < \Delta_{r_{c_2}}$ such that the corresponding effective descriptions become equivalent, i.e.

$$\frac{|h_z(r_{c_1})|}{J_{\text{eff}}(r_{c_1})} = \frac{|h_z(r_{c_2})|}{J_{\text{eff}}(r_{c_2})} \rightarrow \Delta^* = \frac{2\Delta(r_{c_1})\Delta(r_{c_2})}{\Delta(r_{c_1}) + \Delta(r_{c_2})}. \tag{D.9}$$

We refer to these values as *midpoint* of the laser detuning, see Table D.2.

D.2 Numerical simulation

We are now in a position to investigate if the transverse points and/or the midpoint of the laser detuning can change the nature of the expected liquid-phase transition. Figure D.1(a) demonstrates the expected first-order phase transition for different values of the laser detuning including transverse points and midpoints. As seen in the inset, the first-order line remains intact even at the characteristic values of detuning. Crucially, similar to the previous results in Section 5.4.1, this is associated with a persistent blockade effect, as shown in Fig.D.1(b). Indeed, here also the blockade radius decreases by increasing Δ.

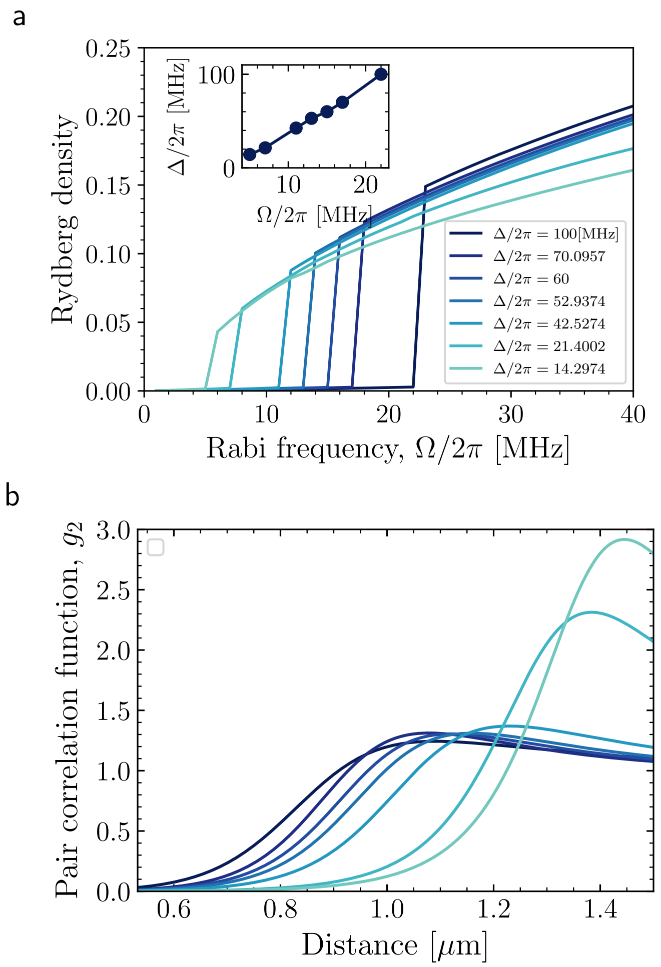

Figure D.1: Variational results for the steady state of 2D driven-dissipative Rydberg gases with $\gamma_a/2\pi = 1$MHz. (a) A first-order transition is shown in terms of Rydberg density for different values of detuning Δ including transverse points and midpoints. The inset shows the first-order line in the plane of $\Delta - \Omega$. (b) Pair correlation function g_2 demonstrates a decrease in Rydberg blockade radius by increasing Δ at $\Omega/2\pi = 40$MHz (In these calculations cluster size is 9×9).

List of Figures

3.1 Spatial configurations of a 2-local Liouvillian 29
3.2 A diagram of the variational quantum simulator 37

4.1 Thermally-activated nucleation process in non-equilibrium steady states 50
4.2 Variational norm for the dissipative Ising model 52
4.3 Relaxation rate in the dissipative Ising model 53
4.4 Phase diagram of Toom's model 58
4.5 Bistability in the variational steady state of Toom's model in the presence of quantum fluctuation 60
4.6 Phase diagram of Toom's model in the presence of quantum fluctuations 61

5.1 Blockade effect in a two-dimensional array of Rydberg atoms 66
5.2 Variational results for the steady state of 2D driven Rydberg gases in the presence of decay 74
5.3 Steady-state phase diagram for driven-dissipative Rydberg gases 75
5.4 Variational results for the steady state of an effective dissipative Ising model 76
5.5 Stationary Rydberg density in the presence of dephasing . . . 78

6.1 Updating ruleset of ECA rule 110 83
6.2 Wolfram's classification of elementary cellular automata . . . 83
6.3 Patterns in elementry cellular automata rule 110. 84
6.4 Gray code enumeration scheme 87
6.5 Master equation embedding of ECA rules 89
6.6 Cycle time phase transition in rule 110 91
6.7 Cyclic setting in RK dynamics and ECA rule 137 94
6.8 Competition between classical rule 137 and a dissipative quantum process 95

7.1 Density-matrix representation of Rokhsar-Kivelson state . . . 99

7.2 Benchmarking of the VQS approach for dynamical preparation of Rokhsar-Kivelson state 101
7.3 Sketch of a variational Quantum circuit for simulation of an unpredictable QCA 103
7.4 Benchmarking of the VQS approach for the quantum rule 137 106

B.1 Spatial gradients corresponding to Toom's model 122
B.2 Domain-wall kinetics in Toom's model 124

D.1 Variational results for the steady state of 2D driven Rydberg gases with characteristic detuning 133

List of Tables

2.1 Dissipative processes in open quantum systems 15
2.2 Comparison of thermal and quantum phase transitions 19

3.1 Classical simulation methods for driven-dissipative systems . 25
3.2 Experimental platforms for variational quantum simulation . 38
3.3 Scaling laws in Rydberg atoms 42

4.1 Ruleset for Toom's model 55

5.1 Varitional ansätze for correlation functions 70

6.1 Jump operators for ECA rule 110 88
6.2 Ruleset to prepare entangled Rokhsar-Kivelson state 93

D.1 Transverse points of the laser detuning in the Rydberg Hamiltonian 131
D.2 Midpoints of the laser detuning in the Rydberg Hamiltonian . 132

Bibliography

[1] M. A. Nielsen and I. L. Chuang, *Quantum computation and quantum information* (Cambridge University Press, Cambridge, 2000).

[2] C. Gross and I. Bloch, Quantum simulations with ultracold atoms in optical lattices, Science **357**, 995 (2017).

[3] V. Giovannetti, S. Lloyd, and L. Maccone, Quantum Metrology, Phys. Rev. Lett. **96**, 010401 (2006).

[4] V. Giovannetti, S. Lloyd, and L. Maccone, Advances in quantum metrology, Nature Photon **5**, 222 (2011).

[5] S. Diehl, A. Micheli, A. Kantian, B. Kraus, H. P. Büchler, and P. Zoller, Quantum states and phases in driven open quantum systems with cold atoms, Nature Phys. **4**, 878 (2008).

[6] F. Verstraete, M. M. Wolf, and J. Ignacio Cirac, Quantum computation and quantum-state engineering driven by dissipation, Nature Phys. **5**, 633 (2009).

[7] H. Weimer, M. Müller, I. Lesanovsky, P. Zoller, and H. P. Büchler, A Rydberg quantum simulator, Nature Phys. **6**, 382 (2010).

[8] H. Weimer, Tailored jump operators for purely dissipative quantum magnetism, J. Phys. B **50**, 024001 (2017).

[9] M. Raghunandan, F. Wolf, C. Ospelkaus, P. O. Schmidt, and H. Weimer, Initialization of Quantum Simulators by Sympathetic Cooling, arXiv:1901.02019 (2019).

[10] R. A. Bertlmann and P. Krammer, Bloch vectors for qudits, Journal of Physics A: Mathematical and Theoretical **41**, 235303 (2008).

[11] O. Giraud, D. Braun, D. Baguette, T. Bastin, and J. Martin, Tensor Representation of Spin States, Phys. Rev. Lett. **114**, 080401 (2015).

[12] R. F. Werner, *Quantum Information Theory — an Invitation*, pages 14–57, Springer Berlin Heidelberg, Berlin, Heidelberg, 2001.

[13] G. Vidal and R. F. Werner, Computable measure of entanglement, Phys. Rev. A **65**, 032314 (2002).

[14] S. Gharibian, Strong NP-hardness of the quantum separability problem, Quantum Information & Computation **10**, 343 (2010).

[15] K. Jacobs, *Quantum Measurement Theory and its Applications* (Cambridge University Press, 2014).

[16] A. Rivas and S. F. Huelga, *Open Quantum Systems* SpringerBriefs in Physics (Springer, Berlin Heidelberg, 2012).

[17] A. J. Daley, Quantum trajectories and open many-body quantum systems, Adv. Phys. **63**, 77 (2014).

[18] A. Shabani and D. A. Lidar, Completely positive post-Markovian master equation via a measurement approach, Phys. Rev. A **71**, 020101 (2005).

[19] S. Alipour, A. T. Rezakhani, A. P. Babu, K. Mølmer, M. Möttönen, and T. Ala-Nissila, Correlation-Picture Approach to Open-Quantum-System Dynamics, Phys. Rev. X **10**, 041024 (2020).

[20] H.-P. Breuer and F. Petruccione, *The Theory of Open Quantum Systems* (Oxford University Press, Oxford, 2002).

[21] P. M. Chaikin and T. C. Lubensky, *Principles of condensed matter physics* (Cambridge University Press, Cambridge, 1995).

[22] E. M. Kessler, G. Giedke, A. Imamoglu, S. F. Yelin, M. D. Lukin, and J. I. Cirac, Dissipative phase transition in a central spin system, Phys. Rev. A **86**, 012116 (2012).

[23] S. Lieu, R. Belyansky, J. T. Young, R. Lundgren, V. V. Albert, and A. V. Gorshkov, Symmetry Breaking and Error Correction in Open Quantum Systems, Phys. Rev. Lett. **125**, 240405 (2020).

[24] H. Weimer, M. Michel, J. Gemmer, and G. Mahler, Transport in anisotropic model systems analyzed by a correlated projection superoperator technique, Phys. Rev. E **77**, 011118 (2008).

[25] P. Navez and R. Schützhold, Emergence of coherence in the Mott-insulator–superfluid quench of the Bose-Hubbard model, Phys. Rev. A **82**, 063603 (2010).

[26] A. Le Boité, G. Orso, and C. Ciuti, Steady-State Phases and Tunneling-Induced Instabilities in the Driven Dissipative Bose-Hubbard Model, Phys. Rev. Lett. **110**, 233601 (2013).

[27] M. Hoening, W. Abdussalam, M. Fleischhauer, and T. Pohl, Antiferromagnetic long-range order in dissipative Rydberg lattices, Phys. Rev. A **90**, 021603 (2014).

[28] H. Weimer, A. Kshetrimayum, and R. Orús, Simulation methods for open quantum many-body systems, Rev. Mod. Phys. **93**, 015008 (2021).

[29] L. M. Sieberer, M. Buchhold, and S. Diehl, Keldysh field theory for driven open quantum systems, Rep. Prog. Phys. **79**, 096001 (2016).

[30] M. F. Maghrebi and A. V. Gorshkov, Nonequilibrium many-body steady states via Keldysh formalism, Phys. Rev. B **93**, 014307 (2016).

[31] M. Raghunandan, J. Wrachtrup, and H. Weimer, High-Density Quantum Sensing with Dissipative First Order Transitions, Phys. Rev. Lett. **120**, 150501 (2018).

[32] J. Johansson, P. Nation, and F. Nori, QuTiP 2: A Python framework for the dynamics of open quantum systems, Comp. Phys. Comm. **184**, 1234 (2013).

[33] J. I. Cirac and F. Verstraete, Renormalization and tensor product states in spin chains and lattices, Journal of Physics A: Mathematical and Theoretical **42**, 504004 (2009).

[34] N. Schuch, M. M. Wolf, F. Verstraete, and J. I. Cirac, Computational Complexity of Projected Entangled Pair States, Phys. Rev. Lett. **98**, 140506 (2007).

[35] F. Verstraete, V. Murg, and J. Cirac, Matrix product states, projected entangled pair states, and variational renormalization group methods for quantum spin systems, Advances in Physics **57**, 143 (2008).

[36] J. Haferkamp, D. Hangleiter, J. Eisert, and M. Gluza, Contracting projected entangled pair states is average-case hard, Phys. Rev. Research **2**, 013010 (2020).

[37] A. Kshetrimayum, H. Weimer, and R. Orús, A simple tensor network algorithm for two-dimensional steady states, Nature Commun. **8**, 1291 (2017).

[38] M. Reh, M. Schmitt, and M. Gärttner, Time-dependent variational principle for open quantum systems with artificial neural networks, arXiv:2104.00013 (2021).

[39] H. Weimer, Variational Principle for Steady States of Dissipative Quantum Many-Body Systems, Phys. Rev. Lett. **114**, 040402 (2015).

[40] X. Yuan, S. Endo, Q. Zhao, Y. Li, and S. C. Benjamin, Theory of variational quantum simulation, Quantum **3**, 191 (2019).

[41] F. Vicentini, A. Biella, N. Regnault, and C. Ciuti, Variational neural network ansatz for steady states in open quantum systems, arXiv:1902.10104 (2019).

[42] W. Krauth, M. Caffarel, and J.-P. Bouchaud, Gutzwiller wave function for a model of strongly interacting bosons, Physical Review B **45**, 3137 (1992).

[43] V. R. Overbeck, *Time evolution and steady states of dissipative quantum many-body systems*, PhD thesis, Gottfried Wilhelm Leibniz Universität, 2018.

[44] V. R. Overbeck and H. Weimer, Time evolution of open quantum many-body systems, Phys. Rev. A **93**, 012106 (2016).

[45] T. Pistorius, J. Kazemi, and H. Weimer, Quantum Many-Body Dynamics of Driven-Dissipative Rydberg Polaritons, Phys. Rev. Lett. **125**, 263604 (2020).

[46] J. Jin, A. Biella, O. Viyuela, L. Mazza, J. Keeling, R. Fazio, and D. Rossini, Cluster Mean-Field Approach to the Steady-State Phase Diagram of Dissipative Spin Systems, Phys. Rev. X **6**, 031011 (2016).

[47] S. Lloyd, Universal Quantum Simulators, Science **273**, 1073 (1996).

[48] J. Preskill, Quantum Computing in the NISQ era and beyond, Quantum **2**, 79 (2018).

[49] A. Peruzzo, J. McClean, P. Shadbolt, M.-H. Yung, X.-Q. Zhou, P. J. Love, A. Aspuru-Guzik, and J. L. O'Brien, Quantum circuits with many photons on a programmable nanophotonic chip, Nat Commun **5**, 4213 (2014).

[50] N. Moll, P. Barkoutsos, L. S. Bishop, J. M. Chow, A. Cross, D. J. Egger, S. Filipp, A. Fuhrer, J. M. Gambetta, M. Ganzhorn, A. Kandala, A. Mezzacapo, P. Müller, W. Riess, G. Salis, J. Smolin, I. Tavernelli, and K. Temme, Quantum optimization using variational algorithms on near-term quantum devices, Quantum Sci. Technol. **3**, 030503 (2018).

[51] C. Kokail, C. Maier, R. van Bijnen, T. Brydges, M. K. Joshi, P. Jurcevic, C. A. Muschik, P. Silvi, R. Blatt, C. F. Roos, and P. Zoller, Self-verifying variational quantum simulation of lattice models, Nature **569**, 355 (2019).

[52] T. Pistorius and H. Weimer, Variational analysis of driven-dissipative bosonic fields, arXiv:2011.13746 (2020).

[53] J. M. Arrazola et al., Quantum circuits with many photons on a programmable nanophotonic chip, Nature **591**, 54 (2021).

[54] I. M. Georgescu, S. Ashhab, and F. Nori, Quantum simulation, Rev. Mod. Phys. **86**, 153 (2014).

[55] M.-C. Chen, M. Gong, X. Xu, X. Yuan, J.-W. Wang, C. Wang, C. Ying, J. Lin, Y. Xu, Y. Wu, S. Wang, H. Deng, F. Liang, C.-Z. Peng, S. C. Benjamin, X. Zhu, C.-Y. Lu, and J.-W. Pan, Demonstration of Adiabatic Variational Quantum Computing with a Superconducting Quantum Coprocessor, Phys. Rev. Lett. **125**, 180501 (2020).

[56] Y. Atas, J. Zhang, R. Lewis, A. Jahanpour, J. F. Haase, and C. A. Muschik, SU(2) hadrons on a quantum computer, arXiv:2102.08920 (2021).

[57] A. Kandala, A. Mezzacapo, Temme, B. Kristan, Takita an Maika, J. M. Markus, Chow, and J. M. Gambetta, Hardware-efficient variational quantum eigensolver for small molecules and quantum magnets, Nature **549**, 242 (2017).

[58] A. Kandala, K. Temme, A. D. Córcoles, A. Mezzacapo, J. M. Chow, and J. M. Gambetta, Error mitigation extends the computational reach of a noisy quantum processor, Nature **567**, 491 (2017).

[59] F. Arute et al., Quantum supremacy using a programmable superconducting processor, Nature **574**, 505 (2019).

[60] Y. Wu et al., Strong quantum computational advantage using a superconducting quantum processor, arXiv:2106.14734 (2021).

[61] J. I. Cirac and P. Zoller, Quantum Computations with Cold Trapped Ions, Phys. Rev. Lett. **74**, 4091 (1995).

[62] F. Schmidt-Kaler, H. Hšffner, M. Riebe, S. Gulde, G. P. T. Lancaster, T. Deuschle, C. Becher, C. F. Roos, J. Eschner, and R. Blatt, Realization of the Cirac-Zoller controlled-NOT quantum gate, Nature **422**, 408 (2003).

[63] J. Zhang, G. Pagano, P. W. Hess, A. Kyprianidis, P. Becker, H. Kaplan, A. V. Gorshkov, Z. X. Gong, and C. Monroe, Observation of a many-body dynamical phase transition with a 53-qubit quantum simulator, Nature **551**, 601 (2017).

[64] C. Monroe, W. C. Campbell, L. M. Duan, Z. X. Gong, A. V. Gorshkov, P. Hess, R. Islam, K. Kim, N. Linke, G. Pagano, P. Richerme, C. Senko, and N. Y. Yao, Programmable Quantum Simulations of Spin Systems with Trapped Ions, arXiv:1912.07845 (2020).

[65] M. Mielenz, H. Kalis, M. Wittemer, F. Hakelberg, U. Warring, R. Schmied, M. Blain, P. Maunz, D. L. Moehring, D. Leibfried, and T. Schaetz, Arrays of individually controlled ions suitable for two-dimensional quantum simulations, Nat. Commun. **7**, ncomms11839 (2016).

[66] P. C. Holz, S. Auchter, G. Stocker, M. Valentini, K. Lakhmanskiy, C. Rössler, P. Stampfer, S. Sgouridis, E. Aschauer, Y. Colombe, and R. Blatt, 2D Linear Trap Array for Quantum Information Processing, Advanced Quantum Technologies **3**, 2000031 (2020).

[67] T. S. Humble, H. Thapliyal, E. Munoz-Coreas, F. A. Mohiyaddin, and R. S. Bennink, Quantum Computing Circuits and Devices, IEEE Design & Test **36**, 69 (2019).

[68] R. Löw, H. Weimer, J. Nipper, J. B. Balewski, B. Butscher, H. P. Büchler, and T. Pfau, An Experimental and Theoretical Guide to Srongly Interacting Rydberg Gases, J. Phys. B: At. Mol. Opt. Phys. (2012).

[69] J. Zeiher, *Realization of Rydberg-dressed quantum magnets*, PhD thesis, Ludwig Maximilian University of Munich, 2017.

[70] A. Cooper, J. P. Covey, I. S. Madjarov, S. G. Porsev, M. S. Safronova, and M. Endres, Alkaline-Earth Atoms in Optical Tweezers, Phys. Rev. X **8**, 041055 (2018).

[71] W. R. Anderson, J. R. Veale, and T. F. Gallagher, Resonant Dipole-Dipole Energy Transfer in a Nearly Frozen Rydberg Gas, Phys. Rev. Lett. **80**, 249 (1998).

[72] I. Mourachko, D. Comparat, F. de Tomasi, A. Fioretti, P. Nosbaum, V. M. Akulin, and P. Pillet, Many-Body Effects in a Frozen Rydberg Gas, Phys. Rev. Lett. **80**, 253 (1998).

[73] A. Browaeys and T. Lahaye, Many-body physics with individually controlled Rydberg atoms, Nature Physics **16**, 132 (2019).

[74] S. de Léséleuc, V. Lienhard, P. Scholl, D. Barredo, S. Weber, N. Lang, H. P. Büchler, T. Lahaye, and A. Browaeys, Observation of a symmetry-protected topological phase of interacting bosons with Rydberg atoms, Science **365**, 775 (2019).

[75] S. Choi, C. J. Turner, H. Pichler, W. W. Ho, A. A. Michailidis, Z. Papić, M. Serbyn, M. D. Lukin, and D. A. Abanin, Emergent SU(2) Dynamics and Perfect Quantum Many-Body Scars, Phys. Rev. Lett. **122**, 220603 (2019).

[76] A. Celi, B. Vermersch, O. Viyuela, H. Pichler, M. D. Lukin, and P. Zoller, Emerging Two-Dimensional Gauge Theories in Rydberg Configurable Arrays, Phys. Rev. X **10**, 021057 (2020).

[77] M. Morgado and S. Whitlock, Quantum simulation and computing with Rydberg-interacting qubits, arXiv:2011.03031 (2020).

[78] C. Dlaska, K. Ender, G. B. Mbeng, A. Kruckenhauser, W. Lechner, and R. van Bijnen, Quantum optimization via four-body Rydberg gates, arXiv:2106.02663 (2021).

[79] S. Ebadi, T. T. Wang, H. Levine, A. Keesling, G. Semeghini, A. Omran, D. Bluvstein, R. Samajdar, H. Pichler, W. W. Ho, S. Choi, S. Sachdev, M. Greiner, V. Vuletic, and M. D. Lukin, Quantum phases of matter on a 256-atom programmable quantum simulator, Nature **595**, 227 (2021).

[80] P. Scholl, M. Schuler, H. J. Williams, A. A. Eberharter, D. Barredo, K.-N. Schymik, V. Lienhard, L.-P. Henry, T. C. Lang, T. Lahaye, A. M. Läuchli, and A. Browaeys, Quantum simulation of 2D antiferromagnets with hundreds of Rydberg atoms, Nature **595**, 233 (2021).

[81] I. Bouchoule and K. Mølmer, Spin squeezing of atoms by the dipole interaction in virtually excited Rydberg states, Phys. Rev. A **65**, 041803 (2002).

[82] J. B. Balewski, A. T. Krupp, A. Gaj, S. Hofferberth, R. Low, and T. Pfau, Rydberg dressing: understanding of collective many-body effects and implications for experiments, New J. Phys. **16**, 063012 (2014).

[83] K. Macieszczak, M. Guţă, I. Lesanovsky, and J. P. Garrahan, Towards a Theory of Metastability in Open Quantum Dynamics, Phys. Rev. Lett. **116**, 240404 (2016).

[84] J. J. Mendoza-Arenas, S. R. Clark, S. Felicetti, G. Romero, E. Solano, D. G. Angelakis, and D. Jaksch, Beyond mean-field bistability in driven-dissipative lattices: Bunching-antibunching transition and quantum simulation, Phys. Rev. A **93**, 023821 (2016).

[85] M. Foss-Feig, P. Niroula, J. T. Young, M. Hafezi, A. V. Gorshkov, R. M. Wilson, and M. F. Maghrebi, Emergent equilibrium in many-body optical bistability, Phys. Rev. A **95**, 043826 (2017).

[86] S. R. K. Rodriguez, W. Casteels, F. Storme, N. Carlon Zambon, I. Sagnes, L. Le Gratiet, E. Galopin, A. Lemaître, A. Amo, C. Ciuti, and J. Bloch, Probing a Dissipative Phase Transition via Dynamical Optical Hysteresis, Phys. Rev. Lett. **118**, 247402 (2017).

[87] F. Letscher, O. Thomas, T. Niederprüm, M. Fleischhauer, and H. Ott, Bistability Versus Metastability in Driven Dissipative Rydberg Gases, Phys. Rev. X **7**, 021020 (2017).

[88] D. Nigro, On the uniqueness of the steady-state solution of the Lindblad–Gorini–Kossakowski–Sudarshan equation, Journal of Statistical Mechanics: Theory and Experiment **2019**, 043202 (2019).

[89] K. Macieszczak, D. C. Rose, I. Lesanovsky, and J. P. Garrahan, Theory of classical metastability in open quantum systems, arXiv:2006.01227 (2020).

[90] T. E. Lee, H. Häffner, and M. C. Cross, Antiferromagnetic phase transition in a nonequilibrium lattice of Rydberg atoms, Phys. Rev. A **84**, 031402 (2011).

[91] T. E. Lee and M. C. Cross, Spatiotemporal dynamics of quantum jumps with Rydberg atoms, Phys. Rev. A **85**, 063822 (2012).

[92] M. Marcuzzi, E. Levi, S. Diehl, J. P. Garrahan, and I. Lesanovsky, Universal Nonequilibrium Properties of Dissipative Rydberg Gases, Phys. Rev. Lett. **113**, 210401 (2014).

[93] A. Le Boité, G. Orso, and C. Ciuti, Steady-State Phases and Tunneling-Induced Instabilities in the Driven Dissipative Bose-Hubbard Model, Phys. Rev. Lett. **110**, 233601 (2013).

[94] J. Jin, D. Rossini, R. Fazio, M. Leib, and M. J. Hartmann, Photon Solid Phases in Driven Arrays of Nonlinearly Coupled Cavities, Phys. Rev. Lett. **110**, 163605 (2013).

[95] A. Le Boité, G. Orso, and C. Ciuti, Bose-Hubbard model: Relation between driven-dissipative steady states and equilibrium quantum phases, Phys. Rev. A **90**, 063821 (2014).

[96] T. Mertz, I. Vasić, M. J. Hartmann, and W. Hofstetter, Photonic currents in driven and dissipative resonator lattices, Phys. Rev. A **94**, 013809 (2016).

[97] C. D. Parmee and N. R. Cooper, Phases of driven two-level systems with nonlocal dissipation, Phys. Rev. A **97**, 053616 (2018).

[98] H. Weimer, Variational analysis of driven-dissipative Rydberg gases, Phys. Rev. A **91**, 063401 (2015).

[99] V. R. Overbeck, M. F. Maghrebi, A. V. Gorshkov, and H. Weimer, Multicritical behavior in dissipative Ising models, Phys. Rev. A **95**, 042133 (2017).

[100] J. T. Young, A. V. Gorshkov, M. Foss-Feig, and M. F. Maghrebi, Nonequilibrium Fixed Points of Coupled Ising Models, Phys. Rev. X **10**, 011039 (2020).

[101] J. Langer, Statistical theory of the decay of metastable states, Ann. Phys. **54**, 258 (1969).

[102] E. Clouet, Modeling of Nucleation Processes, in *ASM Handbook, volume 22A Fundamentals of Modeling for Metals Processing*, edited by D. Furrer and S. Semiatin, ASM Handbook, pages 203–219, ASM International, 2009.

[103] C. Carr, R. Ritter, C. G. Wade, C. S. Adams, and K. J. Weatherill, Nonequilibrium Phase Transition in a Dilute Rydberg Ensemble, Phys. Rev. Lett. **111**, 113901 (2013).

[104] M. Höning, D. Muth, D. Petrosyan, and M. Fleischhauer, Steady-state crystallization of Rydberg excitations in an optically driven lattice gas, Phys. Rev. A **87**, 023401 (2013).

[105] D. C. Rose, K. Macieszczak, I. Lesanovsky, and J. P. Garrahan, Metastability in an open quantum Ising model, Phys. Rev. E **94**, 052132 (2016).

[106] A. L. Toom, Stable and attractive trajectories in multicomponent systems, in *Multicomponent Random Systems*, edited by R. L. Dobrushin, Advances in probability and related topics, pages 549–575, Marcel Dekker, 1980.

[107] C. H. Bennett and G. Grinstein, Role of Irreversibility in Stabilizing Complex and Nonergodic Behavior in Locally Interacting Discrete Systems, Phys. Rev. Lett. **55**, 657 (1985).

[108] P. Gacs and J. Reif, A simple three-dimensional real-time reliable cellular array, Journal of Computer and System Sciences **36**, 125 (1988).

[109] G. Grinstein, Can complex structures be generically stable in a noisy world?, IBM J. Res. Dev. **48**, 5 (2004).

[110] J. L. Lebowitz, C. Maes, and E. R. Speer, Statistical mechanics of probabilistic cellular automata, J. Stat. Phys. **59**, 117 (1990).

[111] L. F. Gray, *Toom's Stability Theorem in Continuous Time*, pages 331–353, Birkhäuser Boston, Boston, MA, 1999.

[112] Y. He, C. Jayaprakash, and G. Grinstein, Generic nonergodic behavior in locally interacting continuous systems, Phys. Rev. A **42**, 3348 (1990).

[113] M. A. Muñoz, F. de los Santos, and M. M. Telo da Gama, Generic two-phase coexistence in nonequilibrium systems, Eur. Phys. J. B **43**, 73 (2005).

[114] P. C. Hohenberg and B. I. Halperin, Theory of dynamic critical phenomena, Rev. Mod. Phys. **49**, 435 (1977).

[115] H. Landa, M. Schiró, and G. Misguich, Multistability of Driven-Dissipative Quantum Spins, Phys. Rev. Lett. **124**, 043601 (2020).

[116] P. Gacs, Reliable Cellular Automata with Self-Organization, Journal of Statistical Physics **103**, 45 (2001).

[117] T. M. Wintermantel, Y. Wang, G. Lochead, S. Shevate, G. K. Brennen, and S. Whitlock, Unitary and Nonunitary Quantum Cellular Automata with Rydberg Arrays, Phys. Rev. Lett. **124**, 070503 (2020).

[118] S. Weber, C. Tresp, H. Menke, A. Urvoy, O. Firstenberg, H. P. Büchler, and S. Hofferberth, Calculation of Rydberg interaction potentials, Journal of Physics B: Atomic, Molecular and Optical Physics **50**, 133001 (2017).

[119] D. Comparat and P. Pillet, Dipole blockade in a cold Rydberg atomic sample, J. Opt. Soc. Am. B **27**, A208 (2010).

[120] E. Urban, T. A. Johnson, T. Henage, L. Isenhower, D. D. Yavuz, T. G. Walker, and M. Saffman, Observation of Rydberg blockade between two atoms, Nature Phys. **5**, 110 (2009).

[121] A. Gaëtan, Y. Miroshnychenko, T. Wilk, A. Chotia, M. Viteau, D. Comparat, P. Pillet, A. Browaeys, and P. Grangier, Observation of collective excitation of two individual atoms in the Rydberg blockade regime, Nature Phys. **5**, 115 (2009).

[122] D. Petrosyan, Dynamics and equilibration of Rydberg excitations in dissipative atomic ensembles, Journal of Physics B: Atomic, Molecular and Optical Physics **46**, 141001 (2013).

[123] M. Gärttner, S. Whitlock, D. W. Schönleber, and J. Evers, Semianalytical model for nonlinear absorption in strongly interacting Rydberg gases, Phys. Rev. A **89**, 063407 (2014).

[124] K. Huang, *Statistical Mechanics* (John Wiley and Sons, New York, 1987).

[125] P. Virtanen and et all, SciPy 1.0: Fundamental Algorithms for Scientific Computing in Python, Nature Methods **17**, 261 (2020).

[126] S. G. Johnson, The NLopt nonlinear-optimization package, https://github.com/stevengj/nlopt, accessed: 01.07.2021 .

[127] H. Weimer, R. Löw, T. Pfau, and H. P. Büchler, Quantum critical behavior in strongly interacting Rydberg gases, Phys. Rev. Lett. **101**, 250601 (2008).

[128] H. Weimer and H. P. Büchler, Two-stage melting in systems of strongly interacting Rydberg atoms, Phys. Rev. Lett. **105**, 230403 (2010).

[129] C. Ates, T. Pohl, T. Pattard, and J. M. Rost, Many-body theory of excitation dynamics in an ultracold Rydberg gas, Phys. Rev. A **76**, 013413 (2007).

[130] M. M. Valado, C. Simonelli, M. D. Hoogerland, I. Lesanovsky, J. P. Garrahan, E. Arimondo, D. Ciampini, and O. Morsch, Experimental observation of controllable kinetic constraints in a cold atomic gas, Phys. Rev. A **93**, 040701 (2016).

[131] J. Honer, R. Löw, H. Weimer, T. Pfau, and H. P. Büchler, Artificial Atoms Can Do More Than Atoms: Deterministic Single Photon Subtraction from Arbitrary Light Fields, Phys. Rev. Lett. **107**, 093601 (2011).

[132] D. W. Schönleber, M. Gärttner, and J. Evers, Coherent versus incoherent excitation dynamics in dissipative many-body Rydberg systems, Phys. Rev. A **89**, 033421 (2014).

[133] N. Margolus, Physics-like models of computation, Physica D **10**, 81 (1984).

[134] E. Berlekamp, J. Conway, and R. Guy, *Winning Ways for Your Mathematical Plays, Vol. 4* (A K Peters, Wellesley, MA, 2004).

[135] M. Cook, Universality in Elementary Cellular Automata, Complex Systems **15**, 1 (2004).

[136] T. Neary and D. Woods, P-completeness of Cellular Automaton Rule 110, Berlin: Springer. Lecture Notes in Computer Science **4051**, 132 (2006).

[137] G. K. Brennen and J. E. Williams, Entanglement dynamics in one-dimensional quantum cellular automata, Phys. Rev. A **68**, 042311 (2003).

[138] R. Raussendorf, Quantum cellular automaton for universal quantum computation, Phys. Rev. A **72**, 022301 (2005).

[139] P. Arrighi, V. Nesme, and R. Werner, One-Dimensional Quantum Cellular Automata over Finite, Unbounded Configurations, in *Language and Automata Theory and Applications*, edited by C. Martín-Vide, F. Otto, and H. Fernau, pages 64–75, Berlin, 2008, Springer.

[140] D. Bleh, T. Calarco, and S. Montangero, Quantum Game of Life, EPL (Europhysics Letters) **97**, 20012 (2012).

[141] L. E. Hillberry, M. T. Jones, D. L. Vargas, P. Rall, N. Y. Halpern, N. Bao, S. Notarnicola, S. Montangero, and L. D. Carr, Entangled quantum cellular automata, physical complexity, and Goldilocks rules, arXiv:2005.01763 (2021).

[142] I. Lesanovsky, K. Macieszczak, and J. P. Garrahan, Non-equilibrium absorbing state phase transitions in discrete-time quantum cellular automaton dynamics on spin lattices, Quantum Sci. Technol. **4**, 02LT02 (2019).

[143] S. Wolfram, Universality and complexity in cellular automata, Physica D **10**, 1 (1984).

[144] G. J. Martinez, J. C. Seck-Tuoh-Mora, and H. Zenil, Computation and Universality: Class IV versus Class III Cellular Automata, J. Cell. Autom. **7**, 393 (2013).

[145] S. Wolfram, *A New Kind of Science* (Wolfram Media, 2002).

[146] J. P. Eckmann and D. Ruelle, Ergodic theory of chaos and strange attractors, Rev. Mod. Phys. **57**, 617 (1985).

[147] W. Li and M. G. Nordahl, Transient behavior of cellular automaton rule 110, Physics Letters A **166**, 335 (1992).

[148] P. Rendell, *Turing Universality of the Game of Life*, pages 513–539, Springer London, London, 2002.

[149] A. M. Turing, On Computable Numbers, with an Application to the Entscheidungsproblem, Proceedings of the London Mathematical Society **s2-42**, 230 (1937).

[150] C. G. Langton, Computation at the edge of chaos: Phase transitions and emergent computation, Physica D **42**, 12 (1990).

[151] S. Aaronson, S. M. Carroll, and L. Ouellette, Quantifying the Rise and Fall of Complexity in Closed Systems: The Coffee Automaton, arXiv:1405.6903 (2014).

[152] M. Li and P. Vitányi, *An Introduction to Kolmogorov Complexity and Its Applications* Texts in Computer Science (Springer, New York, 2008).

[153] R. Cilibrasi and P. M. B. Vitányi, Clustering by Compression, IEEE Transactions on Information Theory **51**, 1523 (2005).

[154] H. Zenil, Compression-based investigation of the dynamical properties of cellular automata and other systems, Complex Systems **19**, 1 (2010).

[155] F. Gray, Pulse code communication, US Patent No. 2,632,058 (1953).

[156] L. P. Deutsch, DEFLATE Compressed Data Format Specification version 1.3, RFC 1951, RFC Editor, 1996.

[157] B. Schumacher, Quantum coding, Phys. Rev. A **51**, 2738 (1995).

[158] R. Jozsa, M. Horodecki, P. Horodecki, and R. Horodecki, Universal Quantum Information Compression, Phys. Rev. Lett. **81**, 1714 (1998).

[159] L. A. Rozema, D. H. Mahler, A. Hayat, P. S. Turner, and A. M. Steinberg, Quantum Data Compression of a Qubit Ensemble, Phys. Rev. Lett. **113**, 160504 (2014).

[160] J. Romero, J. P. Olson, and A. Aspuru-Guzik, Quantum autoencoders for efficient compression of quantum data, Quantum Sci. and Technol. **2**, 045001 (2017).

[161] A. R. Brown and L. Susskind, Second law of quantum complexity, Phys. Rev. D **97**, 086015 (2018).

[162] J. Cotler, N. Hunter-Jones, J. Liu, and B. Yoshida, Chaos, complexity, and random matrices, J. High Energy Phys. **2017**, 48 (2017).

[163] B. LuValle, The Effects of Boundary Conditions on Cellular Automata, Complex Systems **28**, 97 (2019).

[164] K. Bhattacharjee, N. Naskar, S. Roy, and S. Das, A survey of cellular automata: types, dynamics, non-uniformity and applications, Nat. Comp. **17**, 1 (2018).

[165] M. A. Valdez, D. Jaschke, D. L. Vargas, and L. D. Carr, Quantifying Complexity in Quantum Phase Transitions via Mutual Information Complex Networks, Phys. Rev. Lett. **119**, 225301 (2017).

[166] N. Maskara, A. Deshpande, M. C. Tran, A. Ehrenberg, B. Fefferman, and A. V. Gorshkov, Complexity phase diagram for interacting and long-range bosonic Hamiltonians, arXiv:1906.04178 (2019).

[167] A. T. Cesário, D. L. B. Ferreira, T. Debarba, F. Iemini, T. O. Maciel, and R. O. Vianna, Quantum Statistical Complexity Measure as a Signalling of Correlation Transitions, arXiv:2002.01590 (2020).

[168] A. Jamadagni and H. Weimer, An Operational Definition of Topological Order, arXiv:2005.06501 (2021).

[169] A. Arora, D. C. Morse, F. S. Bates, and K. D. Dorfman, Commensurability and finite size effects in lattice simulations of diblock copolymers, Soft Matter **11**, 4862 (2015).

[170] T. S. Cubitt, D. Perez-Garcia, and M. M. Wolf, Undecidability of the spectral gap, Nat. **528**, 207 (2015).

[171] A. Adams, H. Zenil, P. C. W. Davies, and S. I. Walker, Formal Definitions of Unbounded Evolution and Innovation Reveal Universal Mechanisms for Open-Ended Evolution in Dynamical Systems, Sci. Rep. **7**, 997 (2017).

[172] P. Arrighi, An overview of quantum cellular automata, Nat. Comput. **18**, 885 (2019).

[173] T. Farrelly, A review of Quantum Cellular Automata, Quantum **4**, 368 (2020).

[174] M. Roghani and H. Weimer, Dissipative preparation of entangled many-body states with Rydberg atoms, Quantum Sci. Technol. **3**, 035002 (2018).

[175] H. Weimer, M. Müller, H. P. Büchler, and I. Lesanovsky, Digital quantum simulation with Rydberg atoms, Quant. Inf. Proc. **10**, 885 (2011).

[176] I. Lesanovsky, Many-Body Spin Interactions and the Ground State of a Dense Rydberg Lattice Gas, Phys. Rev. Lett. **106**, 025301 (2011).

[177] F. Verstraete and J. I. Cirac, Mapping local Hamiltonians of fermions to local Hamiltonians of spins, J. Stat. Mech. **2005**, P09012 (2005).

[178] P. Jurcevic, B. P. Lanyon, P. Hauke, C. Hempel, P. Zoller, R. Blatt, and C. F. Roos, Quasiparticle engineering and entanglement propagation in a quantum many-body system, Nature **511**, 202 (2014).

[179] H. Bernien et al., Probing many-body dynamics on a 51-atom quantum simulator, Nature **551**, 579 (2017).

[180] J. Honer, H. Weimer, T. Pfau, and H. P. Büchler, Collective Many-Body Interaction in Rydberg Dressed Atoms, Phys. Rev. Lett. **105**, 160404 (2010).

[181] A. W. Glaetzle, M. Dalmonte, R. Nath, C. Gross, I. Bloch, and P. Zoller, Designing Frustrated Quantum Magnets with Laser-Dressed Rydberg Atoms, Phys. Rev. Lett. **114**, 173002 (2015).

[182] R. M. W. van Bijnen and T. Pohl, Quantum Magnetism and Topological Ordering via Rydberg Dressing near Förster Resonances, Phys. Rev. Lett. **114**, 243002 (2015).

[183] R. M. W. Glaetzle, A. W.and van Bijnen, P. Zoller, and W. Lechner, A coherent quantum annealer with Rydberg atoms, Nat. Commun. **8**, 15813 (2017).

[184] J. Zeiher, R. van Bijnen, P. Schauß, S. Hild, J.-y. Choi, T. Pohl, I. Bloch, and C. Gross, Many-body interferometry of a Rydberg-dressed spin lattice, arXiv:1602.06313 (2016).

[185] N. Henkel, R. Nath, and T. Pohl, Three-Dimensional Roton Excitations and Supersolid Formation in Rydberg-Excited Bose-Einstein Condensates, Phys. Rev. Lett. **104**, 195302 (2010).

[186] J. E. Johnson and S. L. Rolston, Interactions between Rydberg-dressed atoms, Phys. Rev. A **82**, 033412 (2010).

[187] P. Virtanen et al., SciPy 1.0: Fundamental Algorithms for Scientific Computing in Python, Nature Methods **17**, 261 (2020).

[188] J. R. McClean, S. Boixo, V. N. Smelyanskiy, R. Babbush, and H. Neven, Barren plateaus in quantum neural network training landscapes, Nature Communications **9** (2018).

[189] F. Pastawski, L. Clemente, and J. I. Cirac, Quantum memories based on engineered dissipation, Phys. Rev. A **83**, 012304 (2011).

[190] M. Herold, E. T. Campbell, J. Eisert, and M. J. Kastoryano, Cellular-automaton decoders for topological quantum memories, npj Quantum Inf. **1**, 15010 (2015).

[191] A. Kubica and J. Preskill, Cellular-Automaton Decoders with Provable Thresholds for Topological Codes, Phys. Rev. Lett. **123**, 020501 (2019).

[192] J. Marshall, L. Campos Venuti, and P. Zanardi, Classifying quantum data by dissipation, Phys. Rev. A **99**, 032330 (2019).

[193] V. Havlícek, A. D. Córcoles, K. Temme, A. W. Harrow, A. Kandala, J. M. Chow, and J. M. Gambetta, Error mitigation extends the computational reach of a noisy quantum processor, Nature **567**, 209 (2019).

[194] D. Bondarenko and P. Feldmann, Quantum Autoencoders to Denoise Quantum Data, Phys. Rev. Lett. **124**, 130502 (2020).

[195] G. N. Milstein, *Numerical Integration of Stochastic Differential Equations* (Springer Netherlands, Dordrecht, 1995).

[196] F. Reiter and A. S. Sørensen, Effective operator formalism for open quantum systems, Phys. Rev. A **85**, 032111 (2012).

[197] A. Actor, Evaluation of multidimensional linear zeta functions, J. Number Theor. **35**, 62 (1990).

Acknowledgments

The past few years have been a challenging part of my life yet full of instructive experiences and cheerful moments. It would not have been possible for me to get through this long journey without the support of the people mentioned below.

I would like to begin my acknowledgments by genuinely thanking my supervisor Dr. Hendrik Weimer for his intellectual guidance and steady support throughout my Ph.D. studies. I sincerely appreciate you for accepting me into the group with all the bureaucratic difficulties. It has been a privilege working under your supervision.

I take the opportunity to express my sincere gratitude towards Prof. Luis Santos who has kindly accepted to be a part of my thesis advisory committee. Besides, I would like to thank the external referee of my dissertation, Prof. Mohammad Maghrebi, who generously took a part despite a busy schedule. I also thank Prof. Tanja Mehlstäubler for chairing my disputation.

I acknowledge financial support from the German research foundation through the priority program "Giant interactions in Rydberg Systems" (GiRyd). I am also thankful to the administrators of the ITP computing cluster. Particular thanks go to Daniel Edler for all his administrative help and advice.

I have been very lucky to work in a pleasant atmosphere created by my colleagues in our research group alongside the members of Prof. Santos' group. Thank you guys for sharing with me all the laughter and enjoyment. Meanwhile, I should especially mention my office mate Amit Jamadagni with whom I have had everyday discussions of physics among other things, easing the bumpy way of the Ph.D. life. It was very nice working with you, I really appreciate all your help in programming and technical issues.

And to all my friends here in Germany, Iran, and elsewhere, thank you for all the emotional support and encouragement. I honestly appreciate every single moment you shared with me.

Most importantly, I am forever indebted to my parents, my siblings, and the rest of my family for always being there for me no matter what. I can't imagine surviving all the hardships of my life without your endless support and encouragement even from miles away.

Publications

Contents of Chapter 6 and Chapter 7 has appeared as a pre-print in the following manuscript which is currently under peer review:

- Javad Kazemi and Hendrik Weimer
  "Unpredictability and Entanglement in Open Quantum Systems"
  Submitted (arXiv:2106.07673)

Contents of Chapter 4 and Chapter 5 will be published under the following tentative titles which are currently in preparation:

- Javad Kazemi and Hendrik Weimer
  "Genuine Bistability in Open Quantum Many-Body Systems"

- Javad Kazemi and Hendrik Weimer
  "Liquid-Gas Transition in Driven-Dissipative Rydberg Gases with Long-Range Interaction"

The author has also contributed in the following article as an application of the variational method introduced in Section 3.2.1:

- Tim Pistorius, Javad Kazemi and Hendrik Weimer
  "Quantum Many-Body Dynamics of Driven-Dissipative Rydberg Polaritons"
  Phys. Rev. Lett 125, 263604 (2020)

Curriculum Vitae

Email: javad.kazemi@itp.uni-hannover.de

Personal details

Birth	:	Feb. 1990, Mashhad, Iran
Gender	:	Male
Nationality	:	Iranian

Education

2017-2021	:	Ph.D., Leibniz Universität Hannover, Germany
2012-2015	:	M.Sc. in condensed-matter physics, Shahid Beheshti University, Iran
2008-2012	:	B.Sc. in solid-state physics, K. N. Toosi University of Technology, Iran

Selbstständigkeitserklärung

Hiermit versichere ich, die vorliegende Doktorarbeit selbständig und unter ausschließlicher Verwendung der angegebenen Hilfsmittel angefertigt zu haben.

Seyedjavad Kazemi
Hannover, Sep 2021